AN ABSTRACT OF THE THESIS OF

Chaur-Fong Chen for the degree of Doctor of Philosophy in Civil Engineering presented on July, 27, 1992.

Title : Analytical Framework for Modeling Scale-Related Variabilities in Remote Sensing.

Abstract approved : Redacted for Privacy
Professor, Richard Cuenca

A general analytical framework was established to investigate the scale-related variabilities in remote sensing. The variabilities were studied first by investigating canopy structure, canopy interaction with light, relation between spectral reflectance and plant phenological parameters. The variabilities simulated by the plant model were compared with the actual spectral data acquired by ground spectroradiometer and satellite sensors. The theoretical relation between orthogonal-based transform and Kahunen-Loéve transform was investigated in the vector space. The role of spectral indices in identifying the status of phenological parameters was briefly studied.

The radiometric corrections of the remotely sensed data were carefully controlled to avoid the unwanted noise introduced by typical resampling/correction procedures from commercial operation. The non-linearity and sensor response corrections were applied to the spectral data as necessary. Variability analysis was conducted to illustrate the complexities of spectral variability embedded in the remotely sensed data.

The information extraction in spatial frequency domain was investigated with emphasis in Fourier domain feature extraction. The Radon transform was introduced as the potential tool to enhance the spatial information of the Fourier transformed image. The adequacy of entropy and fractal dimension as image information measures was proved. A functional link between entropy and fractal dimension was established. The image information content was extracted using various first and second order statistics, entropy, and fractal dimension. Results were presented for different remote sensors based on the full image information content and specific agricultural ground features. The quality of spatial resampling algorithms was tested by investigating the capability to maintain image information in the resampled image. Finally, two applications utilizing this analytical framework were presented to show its potential in land-use classification and multiscale data fusion.

ANALYTICAL FRAMEWORK FOR MODELING SCALE-RELATED VARIABILITIES IN REMOTE SENSING

by

Chaur-Fong Chen

A Thesis

submitted to

Oregon State University

In partial fulfillment of

the requirements for the degree of

Doctor of Philosophy

Completed July 27, 1992

Commencement June 1993

APPROVED :

Redacted for Privacy

Professor of Bioresource Engineering and Civil Engineering in charge of major

Redacted for Privacy

Head of Department of Civil Engineering

Redacted for Privacy

Dean of Graduate School

Date Thesis is presented July 28, 1992

ACKNOWLEDGEMENT

Many support and resources had been contributed to the completion of this thesis. The NASA EOCAP-1 project provided financial support for the major part of my study. My gratitude to Dr. Marshall English and Dr. Richard Cuenca, for their patient guidance and consistent encouragement throughout the completion of this thesis. They were always available not just as advisors but also as friends.

I would like to share the completion of this thesis with Mr. Robinson Barker of SPOT image corporation and Mr. Samuel Lanahan of Environmental Aeroscientific for their support in providing SPOT and CASI data for this research. I would also like to express my deep appreciation to the faculty, staff, and fellow graduate students in the Bioresource Engineering Department and Civil Engineering Department. I will always remember their help and friendship. Special thanks to Dr. Andrew Hashimoto, Head of Bioresource Engineering Department, for providing a dedicated research lab space for this project and other remote sensing related research. Thanks to Mr. Bob Schnekenburger for many lengthy lunch hour problem discussion, machine shop service, and computer network support.

My deepest gratitude to Mr. Frank Lamb of Eastern Oregon Farming Co. and CROPIX Inc. who brought me into the world of remote sensing and digital image processing. During the course of this project he provided a great deal of support and encouragement not only as a great teacher but also as a best friend. His contributions have been a key to the completion of this thesis.

My very special thanks to Ms. Pamela Rew for the hours of conversation, insight, and inspiration in helping me visualize problem from both engineering and human perspectives in the critical stage of this thesis completion.

Finally, I would like to dedicate this thesis to my dear wife Jang Luh and my children Lotos and Elton. Their love and companionship formed the invaluable emotional support during those long and hard years of my graduate study and had made the completion of this thesis possible.

TABLE OF CONTENTS

LIST OF FIGURES

LIST OF TABLES

ANALYTICAL FRAMEWORK FOR MODELING SCALE-RELATED VARIABILITIES IN REMOTE SENSING

INTRODUCTION

Solar radiation passing through the atmosphere, reflected by the ground features on the Earth's surface and received by a remote sensor becomes the spectral signature of that ground feature. The ground feature signature seen by a remote sensor is in fact influenced by surface roughness (such as plant geometry and canopy structure in case of vegetative surface), surface optical properties (e.g. soil moisture and chemical compounds), surface topography, and atmospheric conditions (Figure 1). The aggregation of the feature signature becomes a measure of texture for a specific image. Texture is therefore an important parameter for feature extraction and pattern recognition in remote sensing applications.

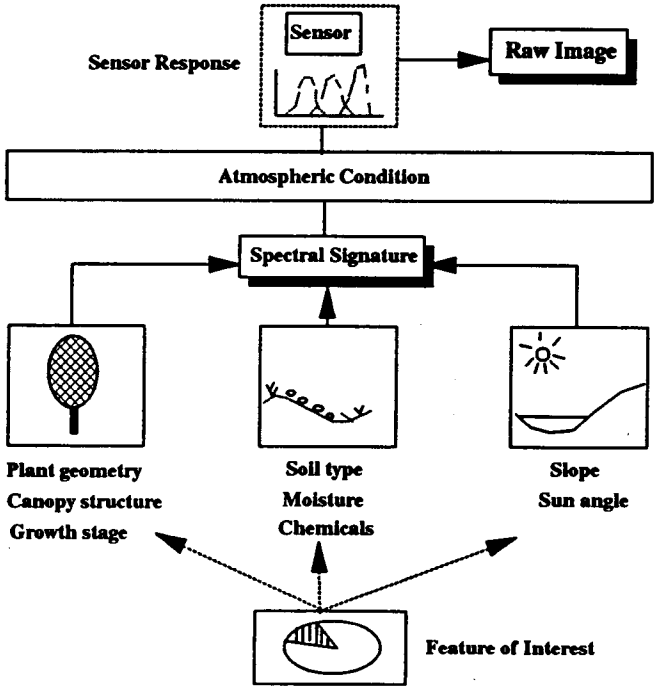

Figure 1. Factors affecting the ground feature spectral signature

Sensors that cover different bandwidth and spatial resolutions often provide significantly different views of the Earth's surface. The real questions are *' Is there any basic feature or process which is invariant with respect to change of spectral and spatial scale ? '* or *' Is there a limiting scale up to which a set of spectral bandwidths will deliver the same information ? '*. A more generalized form of the question would be *' How does a ground feature changes with respect to the scale ? '*.

Typically, a remote sensing image requires certain degrees of preprocessing (Figure 2) before non-

visual information can be extracted. The preprocessing procedures could produce image enhancement as well as information degradation. How the effects from these procedures (such as ***Karhunen-Loêve*** transform or ***Fourier transform***) relate to spectral variability is therefore another important factor to be investigated.

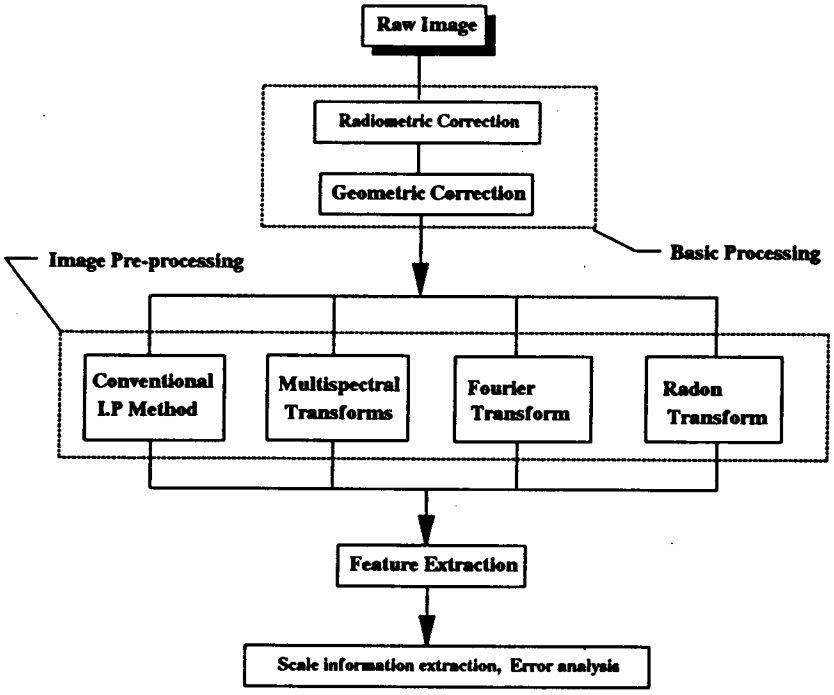

Figure 2. Preprocessing procedures used for image processing

Much research to relate vegetative growth to remotely sensed information has been conducted since Monteith (1972) first expressed the mechanism by which the solar radiation intercepted by any given vegetation is transformed into dry matter. That mechanism can be expressed as:

$$D_m = \int_t \xi_s \xi_i \xi_c S \, dt \qquad (1)$$

Where D_m is the dry matter production; t is the time period, ξ_s is the fraction of photosynthetically active radiation (*PAR*) of the solar radiation, ξ_i is the fraction of the incident light intercepted by the canopy , ξ_c is the dry matter conversion efficiency and S is the global solar radiation. The equation can be used for direct solution when all the parameters on the right hand side are assumed to be known for the inverse problem of estimating vegetation parameters.

In early remote sensing research, efforts were focused on agricultural applications using the Monteith approach to investigate the relationship between vegetative growth parameters and biomass

production. Many useful results have been documented from the *Large Area Crop Inventory Experiment (LACIE)* and *Agriculture and Resources Inventory Surveys Through Aerospace Remote Sensing (AgRISTARS)*. These two projects laid the foundation for using different sensor platforms to obtain specific growth parameters from remotely sensed information. The researchers used statistical regression to establish the relationship between instantaneous spectral reflectance and vegetative parameters of interest. The approach has suffered from the fact that (1) the physical and physiological processes and (2) the nature of spectral signature variation and its propagation were not explicitly taken into account. Most remote sensing models have proven to be site specific or scene dependent when different sensors are applied to obtain reflectance data from variable vegetative cover under heterogeneous conditions. As a result, remote sensing is still as much an art, learned by practice and trial and error, as a science, based on tried and tested methods and rules.

Since practical remote sensing applications have been limited over the past decade, remote sensing technology has often been treated as an interesting matter or expensive toy rather than a practical tool. With the recent worldwide emphasis on global change studies, remote sensing has once again attracted both public and research community attention. With slightly different objectives to be achieved, the underlying physical processes for more recent global change studies do not differ significantly from research conducted in the early 70's. Unfortunately, the lessons from the past unsuccessful history of remote sensing have been forgotten. Instead of extending early efforts in solving basic problems inherited in remote sensing data (and techniques as well), major efforts have been devoted to the launches of more sophisticated sensors with higher spectral and spatial resolution and frequent coverage. While scientists are anxiously waiting for enormous amounts of information covering the whole Earth that is soon to be gathered by new remote sensing platforms, less than 5 percent of the data gathered by LANDSAT satellites has been analyzed to date. The remote sensing community should realize that data alone do not provide understanding. It is only when we put data in context that we create information to provide understanding. Obviously, understanding the meaning of information is a lot more difficult than collecting and displaying it. A systematic approach is needed which combines remotely sensed data with a better understanding of underlying causes of variations in the spectral signature of vegetative canopies. Such an approach could utilize vegetative-phenologic models to aid in interpreting spectral reflectance data acquired from remote platforms.

In satellite remote sensing digital image processing, sometimes it is difficult to analyze the information content of an image directly from the intensity of the image pixels. In fact, the intensity is a function of radiation conditions, atmospheric conditions and sensor response. More important are the local variations of the reflectance. The size of the neighborhood where contrast is computed must be adapted to the size of the objects that we want to analyze. This *size* defines a resolution of reference

for measuring the local variations of the image. Obviously, the structures we want to recognize have different sizes. It is therefore not possible to define *a-prior* an optimal resolution for analyzing an image. People often assume that the higher the resolution the more detailed the information that can be obtained. The details involve the expense of data storage, faster computation requirements and most of all, higher data collection cost.

Efforts to find the optimal resolution for specific image features have been very empirical and limited in the past due to the limitations of sensor platform availability and methods to analyze the information. Hall et al. (1988) developed a hierarchical search for image matching which addressed the resolution problem. It is clear that the study of feature presentation in different scales can provide a simple hierarchical framework for interpreting the information. At different resolutions (scales), the details of an image generally characterize different physical structures of the scene. At a coarse resolution, these details correspond to the larger structures which provide the image *context*. It is a natural process to analyze first the image details at a coarse resolution, then gradually increase the resolution. Such a coarse-to-fine strategy is useful for pattern recognition in image processing and will help in finding the optimal resolution for analyzing a specific ground feature.

During the last twenty years, Benoit Mandelbrot has gradually developed a class of mathematical functions known as ***fractals***. Mandelbrot showed that fractal surfaces can be found in a number of natural processes, ranging from vegetation growth to fingering in porous media flow. A principal characteristic of a fractal process is the lack of any characteristic length scale. Just as a statistically stationary process has a probability distribution that is invariant with respect to translation in time, the fractal process describes the invariance of a probability distribution with respect to scale changes. Clearly, the statistical properties of Earth's features obtained from remote sensing imagery are the result of many physical processes that operate at different spatial locations and scales. Each single physical process may be dominated by a fractal parameter over some localized region and scales. Pentland (1984) showed that the fractal dimension of an image is a measure of surface roughness as well as the invariant scale characteristics of the original data. It is therefore possible to use fractal processes as part of a framework to represent the statistical properties of Earth's features in remote sensing imagery.

The theme of this thesis is to establish an analytical framework which addresses the spectral signature variation issue in the multiresolution context. The derivations start with plant geometry, canopy structure, and their mathematical representation. The relationship between mathematically transformed spectral indices and plant phenological parameters is then derived followed by the preprocessing of a digital image. The concept of image processing in a spatial frequency domain is

introduced. Three mathematical transforms are discussed in detail; they are *(1) Multispectral transformation, (2) Discrete Fourier transform, and (3) Radon transformation.* The extraction of scale information from a digital image is then discussed together with currently used sensors and their response dynamic. Finally, procedures for determination of signature variability and error analysis are investigated. The goal for this research is to establish a generalized framework to study the scale related variabilities from plant canopy level and move up to the satellite level. The specific tasks to be accomplished include

(1) Invetigate the relation between canopy structure, spectral reflectance, spectral indices, and phenological parameters (ground cover and leaf area index specifically) by integrating canopy and photon transfer models.

(2) Study the orthogonal based transform (multispectral transform vegetation indices) and Karhunen-Loéve transform in feature vecotr space.

(3) Investigate potential methods to extract scale related spatial variabilities within a remotely sensed image with emphasis in spatial frequency domain and information content.

(4) Implement and verify the established general framework in the real world applications.

In summary, this thesis proposes systematic procedures to investigate the spectral variabilities due to different image scales (spatial resolutions). The *"spectral"* term used here represents raw spectral reflectance from remote sensors as well as pixel values resulting from image preprocessing.

LITERATURE REVIEW

Remote Sensing Concept

Satellite remote sensing has been used for ground observation since the early 1970s. Although the definition for remote sensing may still be debatable in different disciplines, the following definition was considered to be applicable in general for all disciplines. Remote sensing can be defined as "acquisition of information about the condition and/or the state of a target by a sensor that is not in direct physical contact with it". The use of remote sensing has provided a great way to obtain large amounts of information about Earth's surface features. Even though the applications of remote sensing have been broadened dramatically since the Large Area Crop Inventory Experiment (LACIE, Bauer et al.,1978; MacDonald and Hall, 1980) and Agriculture and Resources Inventory Surveys Through Aerospace Remote Sensing (AgRISTARS, Bauer et al., 1986) projects, the improvement of data analysis techniques has been slow in the past ten years. The launches of LACIE and AgRISTARS were designed to develop operational satellite use capabilities for government and eventually for private industry. The large-scale field measurement programs accompanying the satellite program in the 1970s and early 1980s have contributed to satellite data processing and thematic information capability development such as signature-extendable technology (Hall and Badhwar, 1987). Unfortunately, the overall results have been much less than expected in establishing fundamental understanding of the physical relationship between electromagnetic radiation and Earth surface processes. As a result, the remote sensing community and general public have suffered from the misconception of pictorial products which produce weak correlation to ground attributes to be mapped or monitored.

Vegetative / Phenological Model

In case of natural resources applications, the main problem comes from the inappropriate selection of data based upon the inadequate understanding of the relation between features of interest and the spectral reflectance obtained by the sensor. The basic assumptions of optical remote sensing are (1) solar radiation, which has interacted with the ground object to be sensed and has been received by a remotely located sensor, carries the signature of the object, and (2) this signature can be deciphered to obtain the important characteristics of the object (Goel, 1989). In case of vegetation, these important characteristics include (1) plant identity (or plant type), (2) phenological stage, (3) plant physical conditions, (4) amount of biomass or area indices of plant elements, (5) the architecture of the canopy such as the orientation of the plant, (6) the spatial distribution of ground cover. Numerous research projects have been conducted to study the relation between plant phenological parameters such as the leaf area index (LAI) and light penetration within the plant canopy. The light penetration

characteristics is in fact a good indicator of leaf reflectance as seen by the remote sensor. Most research has focused around the Bouger-Lambert Law (or Beer's Law) which states the relative transmitted light intensity decreases exponentially for each row spacing as the LAI increases. This phenomenon can be expressed in the form of

$$I = I_0 e^{-K(LAI)} \quad (2)$$

Where I is the light intensity at the bottom of the canopy, I_0 is the light intensity immediately above the plant canopy, and K is an extinction coefficient which determines the amount of light attenuated by the plant canopy. This approach provides a useful approximation when the plant canopy is presented as a homogeneous layer (i.e, canopy is in full cover stage), but does not cover the cases when the ground is only partially covered by the canopy. Besides the simplified canopy models, many complex photon transport models were created to simulate the canopy reflectance or inversion of biophysical parameters. A very comprehensive review covering more than fifty photon transport models and six hundred reference papers was assembled by Myneni et al. (1989). Most of these photon transport models assume a fixed leaf distribution and are usually mathematically complicated which require sophisticated numerical solutions. Direct application of these models to a different spatial scale are generally difficult or sometimes impossible. Recent advances in language theory and computer graphics have enable the researcher to define a complex object by successively replacing parts of a simple initial object using a set of rewriting rules or production (Lindenmayer, 1986). Originally, the L-system was designed to generate a realistic decorative plant under a given lighting condition. With simple modification, the deterministic OL system can be used to simulate the canopy reflectance under a given light penetration.

Sources of Spectral Variations

Remote sensing studies of ground features generally suffer from the atmosphere medium interference. Many research projects were conducted specifically to remove or reduce the atmospheric effects. So far, very little attention has been addressed to the influences of soil background over the measured canopy spectral reflectance. The soil background contribution to plant canopy spectral response is very significant in a partially covered ground. Majority portions of the vegetative surface on Earth are partially covered. Huete (1989) investigate the factors which affect the spectral response of partial vegetation covers. The four factors are (1) the structure and biophysical makeup of the vegetation, (2) the soil surface background, (3) solar illumination and sensor viewing conditions, and (4) the atmospheric medium. Research has shown for that for given wave bands soil signatures may vary in (1) brightness differences which are associated with the magnitude of reflected radiance, and (2) spectral curve-shape variations attributed to mineralogic, organic, and water absorption features.

Kauth and Thomas (1976) analyzed soil spectral variations in four-dimensional Landsat images and found the major variations of soils to be attributed to the brightness. The result from this analysis was the widely accepted soil line concept. The soil line concept was used by many researchers such as Jackson et al. (1980), Wiegand and Richardson (1982). The concept of the existence of global soil line was questioned later as Jackson et al. (1980) and Huete et al. (1984) found that the global soil line actually consisted of many nonparallel soil lines that represented specific soil types at different values of soil moisture. The soil line therefore becomes soil-specific and scene-dependent. Stoner and Baumgardner (1981) investigated 485 soils under different moisture conditions. They found five soil forms in the spectral region from 0.52 - 2.32 μm which were associated mainly with the organic matter and iron contents of the soils. Soil spectral curve-shape difference is the cause of deviation away from the soil line. The variations found in the soil line have certain degrees of influence in the vegetation canopy spectral reflectance. Huete et al. (1985) investigated the relationship between spectral reflectance and soil under different moisture contents. Under a bright (light-colored) background, the red reflectance decreased significantly with increasing amount of green cover. Near infrared, on the other hand, increased with increasing vegetation for both wet and dry soils. Researches conducted by Sellers (1985) and Choudhury (1987) indicated that the slopes of spectral isolines increased with increasing vegetation density. Huete and Jackson (1988) further investigated the effects from solar angle and atmospheric turbidity. They found out the diurnal changes in red canopy reflectance was the result of soil effects. The presence of soil background affects the canopy spectral reflectance in different spectral regions. A canopy with a dark soil background is more sensitive to atmosphere conditions in the red spectral regions but less sensitive to sun angle and vegetation density. In summary, the level of soil influence is dependent on the spectral variance of the soil background within an image. The effects of atmospheric conditions on the remotely sensed spectral reflectance are fairly complicated. In general, the atmospheric effects are wavelength dependent. Slater and Jackson (1982) showed that atmosphere effects can cause a three to seven day delay in the detection of water-stressed wheat due to brightness modulation. Corrections of atmospheric effects can be performed using slant-direction measurement based algorithms (such as Diner and Martonchik, 1985), sharp contrast based algorithms (such as Kaufman and Joseph, 1982) or even a dark object subtraction combined with maximum reflectance normalization brute force method (Chen and Waddington, 1992).

Digital Image Processing

The utility of remote sensing has not been fully explored partially due to the lack of image analysis tools, the high cost of satellite images, and data availability. The cost of the remotely sensed data and data availability are issues currently not in the control of the end users (Chen and Lamb, 1991). The

improvement of the image analysis tools therefore will play a pivotal role in bringing remote sensing techniques to practical applications. Image analysis tools which can be generalized into two broad groups include image enhancement (quality) and feature extraction.

Image enhancement

The image enhancement uses various contrast stretching, spatial filtering, data reduction techniques to provide wider dynamic range, higher display contrast and more clear boundary definitions for better image interpretation. Most image enhancement techniques are discrete linear operators. These operators form the output pixel intensity at (x,y) from a weighted sum of input pixel intensities in the neighborhood. The implementations of these algorithms are achieved using a convolution window kernel in the local region (Pratt, 1991). The operator can be applied in both spatial and temporal modes. The spatial operators have the following generalized form

$$g(x,y) = \sum_{i=-n/2}^{n/2} \sum_{j=-n/2}^{n/2} h_{sm}(i,j)\, f(x+i,y+j) \tag{3}$$

Where $f(x,y)$ is the input image, n is the number of row (or column), and $h_{sm}(i,j)$ is the operating function with nonzero values in region S. The approach for spatial operation can easily be extended to temporal case by assuming a specific noise effect model in the form of

$$f_i'(\underline{x}) = f_i + m_i(\underline{x}) \tag{4}$$

Where $f'_i(\underline{x})$ represents a noise corrupted image and $m_i(\underline{x})$ is the noise process at spatial location $\underline{x}$. The desired output image from M ensemble images therefore has the form

$$g(\underline{x}) = \frac{1}{M} \sum_{ensemble} f_i'(\underline{x}) \tag{5}$$

The major drawback of these linear operators is the side effect generally associated with the operator (e.g., the smoothing operator reduces image noise but also blurs edges). The nonlinear operators which can accomplish the objectives of linear operators but do not possess negative attributes have begun to demonstrate their potential (Hodgson, 1985). One of the most promising nonlinear operators is the median filter which is a subset of rank filters. To apply the median filter to an image, the output intensity of each pixel at spatial location $\underline{x} = (x,y)^T$ is chosen on the basis of the relative rank (or intensity) of pixels in the neighborhood. The rank of a set of N pixels in a region S can be denoted as

$$R(\underline{x}) = \{f_1, f_2, \ldots, f_N\} \qquad \forall\ f_i \le f_{i+1} \tag{6}$$

Where f_i is the intensity of pixel i. The output image intensity is

$$g(\underline{x}) = Rank_j\ R(\underline{x}) \tag{7}$$

Where $Rank_j$ is the position of j in $R(\underline{x})$. A median filter can be implemented by choosing the output intensity to be f_m where m is the median intensity and can be obtained at ranking location (N+1)/2 (N should be an odd number). The nonlinear median operator therefore becomes

$$med\ (R(\underline{x})) = Rank_{\frac{N+1}{2}}\ (R(\underline{x})) \tag{8}$$

Nonlinear operators can usually preserve the edge location and reduce the pixel intensity variance while increasing the cost due to intensive computation requirements. If the characteristics of the image sensor and the underlying physical process of the target feature are known and the accurate characterization of image degradation process is available, the model-based enhancement can be utilized.

Feature extraction

Statistical feature extraction

Most of the feature extraction techniques are implemented as forms of pattern recognition. Generally, the pattern recognition can be defined as the determination of an obscure property from a set of measurements (Varmuza, 1980). A number of algorithms are currently being used (e.g. Jensen 1986, Lillesand and Kiefer, 1987). In most cases, a particular decision rule is applied on feature space which is subdivided into non-overlapped regions. The decision rules can be further divided into exploratory methods and confirmatory methods. The exploratory methods use bootstrap solutions to determine the number and nature of the groups present from the distribution of points in the feature space. The confirmatory methods start with an initial hypothesis that k groups of patterns are presented with an initial estimate of the statistical properties of those groups. The pattern recognition procedures can be categorized as supervised classification, clustering, and unsupervised classification. The supervised classification uses proper algorithms to label the pixel in an image as representing particular target features or classes. The algorithms range from probability distribution based models to multispectral space partition for optimally located class-specific regions. All the algorithms used in the remote sensing come from the field of mathematical pattern recognition. The theoretical derivations of these algorithms and their basic applications can be found in Watanabe (1965), Ball and Hall (1965), Cover (1965), Chien and Fu (1967), Cover and Hart (1967), Butt (1968), Tou (1968), Kanal (1968), Batchelor and Wilkins (1968), Hawkins (1970), Duda and Hart (1973), Babu (1973), Anderberg

(1973), Tou and Gonzalez (1974), Young and Calvert (1974). Decision tree (Nilsson, 1965) which uses a series of decisions can also be used for the classification. The advantages of this approach is that different sets of features or algorithms can be used at each decision stage. The application of this algorithm is described by Swain and Hauska (1977). The applications of supervised and unsupervised classifications can be found in Jensen (1986), IEEE Transactions on Geoscience and Remote Sensing, Photogrammetric Engineering and Remote Sensing (American Society of Photogrammetry and Remote Sensing), or other remote sensing related journals. In most cases, a specific algorithm was applied to a remotely sensed digital image with some kind of standard statistical accuracy assessment. Very little progress has been made in advancing the analysis tools during the past ten years. Recently, with the increasing attention focused on the global change issues and the launches of upcoming Earth Observing System (EOS, Butler et al., 1984) satellites, remote sensing has once again drawing the attention from both public and private sectors. The basic understanding of the Earth physical processes and their relations with the optical sensor and spectral reflectance were the main issues emphasized in the EOS preliminary studies (Butler *et al.*, 1988). The need for better techniques to interpret data acquired by the remote sensing platforms was also stressed in the EOS data panel report (Butler *et al.*, 1988). One important issue surfacing from the EOS project is capability to perform multiscale multiresolution data merging.

Multiscale feature extraction

The basic concept to merge or utilize the data from different scales is similar to the concept of multiresolution decomposition used in digital signal processing. Koenderink (1984) studied the structure of an image and proposed the potential of using simple hierarchical framework for interpreting the image information content. The details of an image generally characterize different physical structures of the scene at different resolutions. At a coarse resolution, the details usually correspond to larger structures (or features) which also provide an overall image context. The pattern recognition procedures therefore should include a coarse-to-fine approach. This approach was first used by Grimson (1985) to perform a low level image analysis on a set of images in different resolutions. Another algorithm which holds great potential for multiscale image analysis is the Hierarchical/Pyramidal image analysis (Biederman, 1985). A hierarchical processing procedure basically emulates the way human visual system (HVS) process the object vision from a coarser descriptive level to a set of consecutive refinement levels. Since features in different scales may be related, a basic requirement for the multiscale operator is the ability to maintain a consistent representation of the multiscale image. Baubaud et al. (1986) developed a scale-space filter by convoluting the input image with a Gaussian kernel which contains a scale parameter. The scale-modified 1-D function is given by

$$\phi(x,y) = f(x) * g(x,y) \tag{9}$$

Where * represents a specific convolution process or

$$\phi(x,y) = \int_{-\infty}^{\infty} f(u)\, g(x-u,y)\, du \tag{10}$$

In this particular case, the above equation produces an ensemble of images as a function of the scale parameter y. If a consistent scale-space kernel $g(x,y)$ is used, then the new zero crossing may appear, but the existing ones never disappear (Baubaud et al., 1986). The most interesting characteristics of such an operator is that for a given linear differential operator, L

$$\begin{aligned} L[\phi(x,\hat{y}) &= L[f(x)] * g(x,\hat{y}) \\ &= f(x) * L[g(x,\hat{y})] \end{aligned} \tag{11}$$

The above equation indicates that image enhancement can either be performed before scale reduction or after the scale reduction. This feature provides a lot of flexibility for image manipulation. So far, the multiscale analysis has started gaining popularity among computer vision applications. The application is still more or less limited to edge contouring (Williams and Shah, 1988) or segmentation (Bischof and Caelli, 1988). Another tool which also holds great potential for multiscale image analysis is fractals. Since the introduction of *fractals* by Mandelbrot (1977), the studies related to fractal applications have grown exponentially. The studies range from time series simulation, spatial chaos, random vibration, percolation, phase transition and renormalization, to cellular automata. The discussions of these studies are far beyond the scope of this literature review. Besides all these potential applications of fractals, the application in image analysis has been limited to the realistic image generation of mountains, planets, or trees (Peitgen and Richter, 1986). Pentland (1984) published a paper titled "Fractal-based description of natural scenes" (Pentland, 1984). The paper has provided a general foundation for fractal applications in image analysis. A few papers have been published since Pentland's work. Most of the research has been focused on structure-oriented images such as an image produced by Synthetic Aperture Radar (SAR, Dellepiane et al., 1991) or the measuring of the geometric characteristics of natural surfaces (Clarke and Schweizer, 1991). Research conducted by Lam (1990) focused on the fractal dimension of a satellite image surface which did not address the multiscale issue. Even though fractal applications in remote sensing has been slow, the use of fractal description for image analysis still looks very promising.

In spite of all the development in multiscale analysis, the use of multiscale information extraction in remotely sensed images (particularly in satellite remote sensing) has been very limited due to the constraint imposed by availability of the remote sensing platforms (i.e. very few spatial resolutions are available to the researcher). Curran (1988) utilized the semivariogram to investigate the underlying spatial correlation within a remotely sensed image. Woodcock et al. (1988) used the same technique to simulate and model the remotely sensed scene. This research generated interesting questions about the scale issue in the remotely sensed images but did not provide real utility for multiscale image analysis. The general direction of these approaches is positive since the spatial relationship between adjacent pixels is taken into account. Traditionally, feature extraction in remotely sensed images has been focused on tonal or spectral information, i.e. pixel values have been considered individually without regarding the properties of neighboring pixels. Ideally, the features from neighboring pixels should provide additional spatial information for image analysis. A logical representation of the neighborhood features is to use some kind of texture measure.

Texture features

The texture presentation was used extensively in the field of psychology. Researchers have studied texture discrimination by the human visual system. Julesz (1975) conducted statistical analysis on two textures and concluded that two textures are not discriminable instantly if their second order statistics are identical. Further study done by Julesz and Caelli (1979) revealed the exceptions in case of measurement based on local geometrical features. The uses of texture information in image analysis have been focused on image segmentation in machine vision level. In the field of computer vision, textures are analyzed either by structural or statistical methods. The nature of texture analysis at the structural level does not render itself as a tool for remotely sensed data. Texture analysis in the statistical level does present great potential for multiresolution remote sensing analysis. Theoretically, the pattern variations in the neighborhood pixel can be obtained from either the image domain or frequency domain. Weska *et al.* (1976) adopted an algorithm proposed by Haralick *et al.* (1973) to show the advantages of using image domain methods over frequency domain methods. The potential of using texture information for pattern recognition did not receive wide acceptance due to its computation costs. Kittler and Foglein (1984) demonstrated the use of textural information as an additional feature during the feature labeling phase.

It is clear that texture information obtained from the multispectral image has not received any noticeable acceptance. The reliability resulting from the incorporation of texture information remains to be proved mathematically or statistically.

THEORY

Plant Geometry, Plant Development and Phenological Parameters

The plant canopy structure, properties of the leaf, and pattern of light attenuation within the canopy are the major factors that affect the reflectance acquired from a remote sensing device. In the case of agricultural crops, how the canopy is structured is mainly a function of cultural practices. Typical row crops start as independent plants isolated from neighboring plants. As the plant grows the leaf canopy tends to overlap and interfere with adjacent plants, eventually forming a closed leaf canopy. Edwards (1986) suggested that there are three levels at which we can investigate the clumping of leaves in a plant canopy. The three levels are: (1) clumping together as an entire canopy of either a discrete plant or community of plants; (2) clumping together on the separate branches subtended by the plant; and (3) clumping together by individual position on the branch. All three levels of clumping affect the canopy structure in different scales. For most plants the canopy structure is somewhat heterogeneous in the natural environment. A basic mathematical model of the plant canopy structure is essential to help in modeling the reflectance observed by the sensor as a result of light being transmitted, reflected, or absorbed by the leaves and their background. Consider a plant with a basic structure as shown in Figure 3 (adopted from Prusinkiewics, 1986).

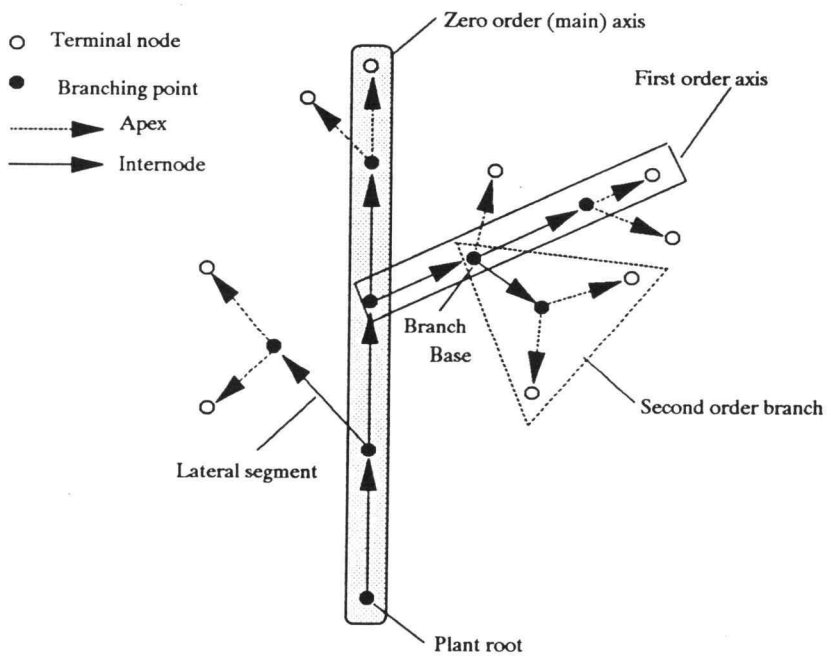

Figure 3. Basic plant branch structure

The plant is represented as a theoretical graph-notion of Preparatas (1973) "*rooted tree*" with the botany inspired notion of branches and axes. The base node of the rooted tree is called the ***root***. The edge segments form paths from root nodes. In a biological context, the edges are referred as branch segments. A segment followed by at least one more segment in any path is called an ***internode***. A segment with no succeeding edges is called an ***apex***. A sequence of segments is defined as an ***axis*** if the following conditions are met : (1) the first segment in the sequence originates at the root of the tree or as a lateral segment at some node, (2) each subsequent segment is a straight segment, and (3)the last segment is not followed by any straight segment in the tree. The axis and its descendants constitutes a ***branch***. The axes and branches can be ordered as shown in Figure 3 with a pre-fixed angle between axes. Prusinkiewicz et. al (1989) have used a similar notation to model and produce photo-realistic graphics of botanical garden plants. The geometric notation of such a plant should be viewed as an intuitive link between the graph theory and real plant structure. Similar branching pattern exists between the theoretical ***rooted tree*** in Figure 3 and a typical potato plant diagram as shown in Figure 4. It is therefore a reasonable assumption to model a specific plant structure with the mathematical tree shown in Figure 3 coupled with specific leaf angle distribution for the plant.

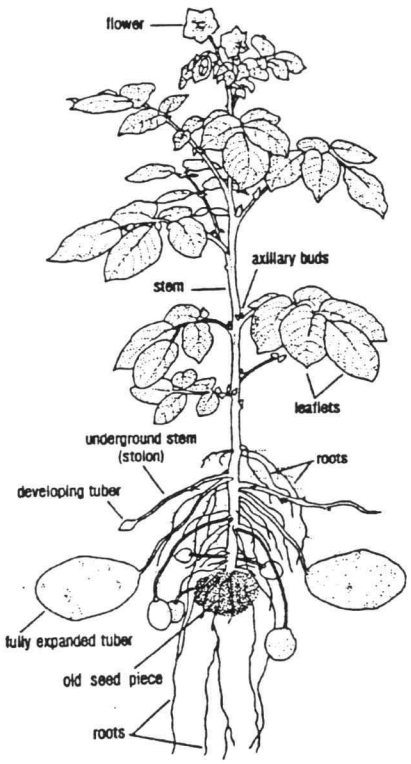

Figure 4. Diagram of a typical potato plant

Plant stand modeling using L-systems

The L-systems first originated by Lindenmayer (1968) are widely used by computer scientists as the formalism of language theory. Recently, L-systems and fractals have been combined to generate photo realistic images of flowers and plants. The utility of L-systems as a tool to model plant geometry for spectral reflectance estimation has not been investigated. The basic concept of L-systems can be described using a definition from Prusinkiewicz (1980) : " ***define complex objects by successively replacing parts of a simple initial object using a set of rewriting rules or productions***". Vigorous mathematical proofs can be found in Herman and Rozenberg (1975). Only basic concepts and definitions will be reviewed in this section. A deterministic OL system ***(DOL)*** is the basic form for plant stand modeling.

Define *a* DOL system as a triple, $G = (\Sigma, h, \omega)$

where

Σ : an alphabet

h : endomorphism defined on Σ^*

Σ^* : the set of all nonempty words over Σ

ω : an element of Σ^* refered to as an axiom (12)

Define the language of G as L(G)

$$L(G) = \bigcup_{i \geq 0} h^i(\omega) \quad or \tag{13}$$

$$h^0(\omega) = \omega, h(\omega), h^2(\omega), h^3(\omega), \ldots$$

The above definitions indicate that the L-systems have properties such as parallelism in rewriting processes and the notion of rewriting process conceived as a dynamic process. These properties imply the suitability for biological development modeling. Obviously, plant development is a far more complex process than a few simplified mathematical definitions. The lengths of stands are likely to increase strictly in most plant stand development. A DOL system does not guarantee strictly increasing word length. More constraints should be added to DOL systems to account for the biological processes.

Definition : A propagating DOL (PDOL) system is

$$G = (\Sigma, h, \omega) \subset \{ \text{ no } a \in \Sigma \rightarrow \Lambda \in h(a) \} \tag{14}$$

in other words, h is nonerasing

Remark : $L^i(G,x) = \{ y \in \Sigma^* \mid y \in h^i(x) \}$, $\forall x \in \Sigma^*$, $i \geq 1$

Set $L^0(G,x) = \{x\}$ $\rightarrow$ $L(G) = \bigcup_{i \geq 0} L^i(G,\omega)$

Define the following terms

$$\begin{aligned}
&x \underset{G}{\rightarrow} y, && \text{x directly derives y (in G) if } y \in L^1(G,x) \\
&x \overset{n}{\underset{G}{\rightarrow}} y, && \text{x derives y in n steps (in G) if } y \in L^n(G,x) \\
&x \overset{+}{\underset{G}{\rightarrow}} y, && \text{x derives y (in G) if } y \in L^n(G,x), \text{ for some } n \geq 1 \text{ ; } \textit{and} \\
&x \overset{*}{\underset{G}{\rightarrow}} y, && \text{x derives y (in G) if } y \in L^n(G,x) \text{ for some } n \geq 0
\end{aligned} \tag{15}$$

This set of tools, L-system characters and rewriting rules will be used to describe a tree. Consider a string consisting of $\{x,y\}$ and for each letter a production rule is assigned as

$$\begin{aligned}
x &\rightarrow y && \rightarrow \text{character x will be replaced by y} \\
y &\rightarrow xy && \rightarrow \text{character y will be replaced by xy}
\end{aligned} \tag{16}$$

This set of rewriting rules produces a tree-like structure as shown in Figure 5. The branching topology of the tree was defined using the L-systems. However, the geometric aspects such as the length of each segment and branching angle are not included in the tree.

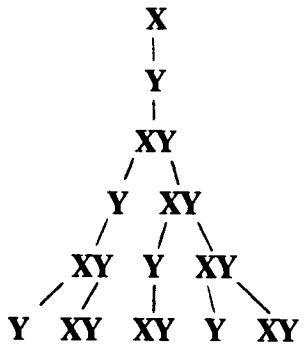

Figure 5. Tree structure generated from string $\{x,y\}$ and L-systems

Prusinkiewicz (1986) introduced a extension of turtle interpretation with bracket strings and L-system to formally describe branching structures found in many plants. Details about these systems are not discussed since it is out of the scopes of this study. Consider a branching point in Figure 3. The state of a branching point can be expressed as $B\ (x,y,z,r,\theta,\phi)$, where the Cartesian coordinates (x,y,z) represent the branching point in 3-D space, and the spherical coordinates (r,θ,ϕ) represent the subsequent segment length and relative location to the branching point (Figure A.1 in appendices). A plant stem can be generated using the above DOL systems. For simple analysis, leaf curvature was not considered.

General law for radiation beam penetration into the canopy

The following approach to study canopy characteristics in radiation regime was adopted from Mann's early research since it lead to the concept of pseudo area index which was well accepted in agriculture research community.

1. Line transect model with fixed projection width W

Assume each leaf has a projection width W which is projected onto a transect of length L located arbitrarily within/below a crop canopy. The leaf projection and related coordinate system are illustrated in Figure A.2 (Appendices). Each leaf projection is identified by the midpoint. The locations of midpoints are assumed to be a set of random variables with distribution function F and density function P_r. If x is a point in the transect L, the probability of x not being covered by a projection from any of the N leaves in the canopy is given by

$$P(x|N) = [F(x-\frac{W}{2}) + 1-F(x+\frac{W}{2})]^N \tag{17}$$

where

$$F(x-\frac{W}{2}) = 0, \forall x<\frac{W}{2} \tag{18}$$

$$F(x+\frac{W}{2}) = 1, \forall x>L-\frac{W}{2} \tag{19}$$

$$F(x-\frac{W}{2}) = \text{probability of } x \in l_1 \tag{20}$$

$$1-F(x+\frac{W}{2}) = \text{probability of } x \in l_2 \tag{21}$$

The expected portion of the transect being contacted by a light beam is the integral of the probability of individual points along L being seen by the beam which can be represented by

$$\mathscr{E}(contact|N\ Leaves,\ projection\ width=W) = \frac{1}{L}\int_0^{\frac{W}{2}}[F(x-\frac{W}{2}) + 1 - F(x+\frac{W}{2})]^N\,dx \tag{22}$$

$$+\frac{1}{L}\int_{\frac{W}{2}}^{L-\frac{W}{2}}[F(x-\frac{W}{2})+1-F(X+\frac{W}{2})]^N\,dx+\frac{1}{L}\int_{L-\frac{W}{2}}^{L}[F(x-\frac{W}{2})+1-F(x+\frac{W}{2})]^N\,dx \quad (23)$$

Assume that for each positive integer N, there is a set of random variables $(x_1, x_2, \ldots x_n, Y)$, where Y is uniformly distributed along L, x_i are distributed according to a distribution function F with density function P_r, X_i represent the center of leaf projection. $(Y = y \mid W, N)$ is an event such that point y has contact with the incoming radiation beam given N leaves with projection on L, each with a width W. The probability that point y has contact with the radiation beam is equal to the probability of y not being covered by the leaf projection i centered at X_i and can be expressed as

$$P_r\{Y-y|W,N\} = P_r\{(X_i-\frac{W}{2})>y \;\; or \;\; (X_i+\frac{W}{2})<y\} = P_r\{|X_i-y|>\frac{W}{2}\} \quad (24)$$

The probability that point y is not covered by any of the N leaf projections becomes

$$P_r\{y|W,N\} = P_r\{\bigcap_{i=1}^{N}[|X_i-y|>\frac{W}{2}]\} = \prod_{i=1}^{N}P_r\{|X_i-y|>\frac{W}{2}\} \quad (25)$$

Since

$$P_r\{|X_i-y|>\frac{W}{2}\} = P_r\{(X_i-\frac{W}{2})>y\} + P_r\{(X_i+\frac{W}{2})<y\} = F(y-\frac{W}{2}) + [1-F(y+\frac{W}{2})] \quad i=1,2,\ldots N \quad (26)$$

Equation (25) becomes

$$P_r\{y|W,N\} = [F(y-\frac{W}{2}) + 1 - F(y+\frac{W}{2})]^N \quad (27)$$

The expected portion of L in contact with the radiation beam is equal

$$\frac{1}{L}\int_0^L[F(y-\frac{W}{2}) + 1 - F(y+\frac{W}{2})]^N dy \quad (28)$$

The equation is subject to the following boundary conditions,

$$F(y-\frac{W}{2}) = 0 \ , \ \forall\, y<\frac{W}{2} \tag{29}$$

$$F(y-\frac{W}{2}) = 1 \ , \ \forall\, y>L-\frac{W}{2} \tag{30}$$

Applying the above boundary conditions to Equation (28) yields

$$\frac{1}{L}\int_0^L [F(y-\frac{W}{2}) + 1 - F(y+\frac{W}{2})]^N dy - \frac{1}{L}\int_0^{\frac{W}{2}} [F(y-\frac{W}{2}) + -F(y+\frac{W}{2})]^N dy \tag{31}$$

$$+\frac{1}{L}\int_{\frac{W}{2}}^{L-\frac{W}{2}} [F(y-\frac{W}{2}) + 1 - F(y+\frac{W}{2})]^N dy + \frac{1}{L}\int_{L-\frac{W}{2}}^{L} [F(y-\frac{W}{2}) + -F(y+\frac{W}{2})]^N dy \tag{32}$$

$$-\frac{1}{L}\int_0^{\frac{W}{2}} [1-F(y+\frac{W}{2})]^N dy + \frac{1}{L}\int_{\frac{W}{2}}^{L-\frac{W}{2}} [F(y-\frac{W}{2}) + 1 - F(y+\frac{W}{2})]^N dy + \frac{1}{L}\int_{L-\frac{W}{2}}^{L} [F(y-\frac{W}{2})]^N dy \tag{33}$$

If the leaf projection location has a distribution function F, the expected value of the portion of L in contact with the radiation beam for N leaves with fixed projection width W is

$$\frac{1}{L}\int_0^L [F(y-\frac{W}{2}) + 1 - F(y+\frac{W}{2})]^N dy \tag{34}$$

If leaves are clustered together and N becomes large, the total projection area will tend to stay constant ($NW = k$) and Equation (34) becomes

$$\lim_{N\to\infty}{}^{NW=k} \mathcal{E}\{\text{ has beam contact } |N,W,\} = \lim_{N\to\infty} \frac{1}{L}\int_0^L \exp\{N\log[F(y-\frac{W}{2}) + 1 - F(y+\frac{W}{2})]\}\, dy \tag{35}$$

Based on the convergence theory and exponential continuity, Equation (35) can be rearranged as

$$\frac{1}{L}\int_0^L \exp \lim_{N\to\infty} \frac{\log[F(y-\frac{k}{2N}) + 1 - F(y+\frac{k}{2N})]}{N^{-1}}\, dy \qquad (\because W = \frac{k}{N}) \tag{36}$$

As N approaches the limit, both numerator and denominator will become zero. Simplifying Equation (36) according to the L'Hôpital rule

$$\frac{1}{L}\int_0^L \exp \left(\lim_{N\to\infty} \frac{f(y-\frac{k}{2N})\frac{k}{2N^2} + f(y+\frac{k}{2N})\frac{k}{2N^2}}{[F(y-\frac{k}{2N}) + 1 - F(y+\frac{y}{2N})](-N^{-2})}\right) dy \tag{37}$$

$$-\frac{1}{L}\int_0^L \exp\{-\frac{k}{2}[f^-(y) + f^+(y)]\}\, dy \tag{38}$$

If f is a continuous function,

$$\mathscr{E}\{\text{has light beam contact}\} = \frac{1}{L}\int_0^L e^{-k f(y)}\, dy \tag{39}$$

Assume the leaf projection over L is uniformly distributed, $P_r(x) = 1/L$, $F(x) = x/L$, *for all* $x \in [0,L]$. Carrying out the integration in Equations (31-33) yields

$$\int_0^{\frac{W}{2}} (1-\frac{y}{L}-\frac{W}{2})^N dy + \int_{\frac{W}{2}}^{L-\frac{W}{2}} (1-W)^N dy + \int_{L-\frac{W}{2}}^{L} (\frac{y}{L}-\frac{W}{2})^N dy \tag{40}$$

Equation (40) can be expanded to

$$\mathscr{E}(\text{average portion of contact} \mid \text{N leaves, projection width} = \text{W, projection uniformly distributed}) = \tag{41}$$

$$\frac{N-1}{N+1}(1-\frac{W}{L})^{N+1} + \frac{2}{N+1}(1-\frac{W}{2L})^{N+1} \tag{42}$$

2. Line Transect Model with Stochastic Projection Width $R(W) \subset [a,b]$

The result based on the assumption that all the projections have a constant width W cannot be applied directly to the field condition. It is more reasonable to assume W follows a probability distribution, that is, the length of leaf projections will vary with location along a transect. Let $F_{(x|d)}$ be the conditional distribution function of X given $W = d$. The average (expected) portion of contact becomes

$$\mathscr{E}(\textit{contact with radiation beam} \mid N \textit{ leaves, projection width} - W \textit{ with } F_{(x|d)}) \tag{43}$$

$$= \frac{1}{L}\int_0^L \{E_W[F_{(x|W)}(y-\frac{W}{2}) + 1 - F_{(x|W)}(y+\frac{W}{2})]\}^N dy \tag{44}$$

Let Y_i represent the location of the center of the i^{th} leaf projection along L and the width of projection W_i be a random variable with some distribution function. If $(T_i \mid Y = y)$ represents the event that point y is not covered by leaf projection i, the following equality exists

$$P_r(T_i \mid Y-y) = \mathscr{E}_{(x,W)}\, P_r[(T_i \mid Y-y) \mid (x,W)] \tag{45}$$

where $E_{(x,W)}$ is the expectation with respect to the joint distribution of X and projection width W. Equation (45) can be rewritten as

$$P_r(T_i \mid Y-y) = \int_{R(W)} [F_{(x|Z)}(y-\frac{Z}{2}) + 1 - F_{(x|Z)}(y+\frac{Z}{2})]\, g(z)\, dz \tag{46}$$

$R(W)$ is the domain of W and $g(z)$ is the density function of W. Rewriting Equation (46) for events T_i where y is not covered by any of the N leaf projections as

$$P_r(T_i, N \mid Y-y) = [P_r(T_i \mid Y-y)]^N \tag{47}$$

The average value for the portion of L that has contact with the radiation beam is therefore equal to

$$P_r(T,N \mid Y-y) = \frac{1}{L}\int_0^L \{\int_{R(W)} [F_{(x|Z)}(y-\frac{Z}{2}) + 1 - F_{(x|Z)}(y+\frac{Z}{2})]\, g(z)\, dz\}^N dy \tag{48}$$

$$B.C: \quad R(W) \subset [0,L] \quad \textit{range of the projection width} \tag{49}$$

$$W \subset [a,b] \quad \textit{width projection is bounded by } [a,b] \tag{50}$$

Consider the critical points for the projection midpoint location along L where the probability distribution changes. Divide L into section I to V as shown in Figure A.3 (Appendices), such that the probability distribution can be applied to each section separately. The expected value of the portion that has contact with the radiation beam is

$$\mathcal{E}(\textit{contact with beam} \mid N, W, \subset [a,b]) = \tag{51}$$

$$\textit{Section I} : \int_0^{\frac{a}{2}} \{ \int_a^b [1 - F_{(x|Z)}(x+\frac{Z}{2})]\, g(z)dz \}^N dx \tag{52}$$

$$\textit{Section II} : \int_{\frac{a}{2}}^{\frac{b}{2}} \{ \int_a^{2x} [F_{(x|Z)}(x-\frac{Z}{2}) + 1 - F_{(x|Z)}(x+\frac{Z}{2})]\, g(z)dz + \int_{2x}^b [1 - F_{(x|Z)}(x+\frac{Z}{2})]\, g(z)dz \} \tag{53}$$

$$\textit{Section III} : \int_{\frac{b}{2}}^{L-\frac{b}{2}} \{ \int_a^b [F_{(x|Z)}(x-\frac{Z}{2}) + 1 - F_{(x|Z)}(x+\frac{Z}{2})]\, g(z)dz \}^N dx + \tag{54}$$

$$\textit{Section IV} : \int_{L-\frac{a}{2}}^{L-\frac{b}{2}} \{ \int_a^{2L-2x} [F_{(x|Z)}(x-\frac{Z}{2}) + 1 - F_{(x|Z)}(x+\frac{Z}{2})]\, g(z)dz + \int_{2L-2x}^b F_{(x|Z)}(x-\frac{Z}{2})]\, g(z)d \tag{55}$$

$$\textit{Section V} : \int_{L-\frac{a}{2}}^{L} [\int_a^b F_{(x|Z)}(x-\frac{Z}{2})\, g(z)dz \}^N dx \tag{56}$$

3. 2-Dimensional Model with Stochastic Projection Region

Assume that the canopy is projected from a 3-D point *(x,y,z)* into a 2-dimensional domain R as shown in Figure A.4. The distribution of 3-D points *(x,y,z)* will be mapped onto a 2-dimensional distribution.

Assume the 2-D point distribution is called $F(s,t)$. The total projection area is the sum of N small areas. The size of each small area (W) equals k/N, where k is some constant. Any point $(s,t) \in R$ will have contact with the light beam if none of the leaves fall within the bounded region

$$\Omega \; : \; \{[s-\frac{W}{2}, s+\frac{W}{2}] : [t-\frac{W}{2}, t+\frac{W}{2}]\} \tag{57}$$

The probability of point (s,t) not being covered by a leaf can be expressed as

$$h(s,t,w) = 1 - \int_R \int f(x,y)dydx \tag{58}$$

where $f(x,y)$ is the joint probability density function of point $(s,t) \in R$ that will be bounded by Ω. If all leaves are independently distributed the probability that none of the N leaf fragments will cover the point (s,t) is $[h(s,t,w)]^N$ with expected value

$$\mathcal{E}(\{S\},N) = \int_R \int [h(s,,t,w)]^N dsdt \tag{59}$$

where $\{S\}$ is the event that point (s,t) will be covered by any of the N leaves (fragments). By applying mean-value theorem for each point $(s,t) \in R$ there exists a point $(a(s),b(t)) \in \Omega$ such that

$$\mathcal{E}(\{S\},N) = \int_R \int [1 - \frac{k}{N} f(a(s),b(t))]^N dsdt \tag{60}$$

Let

$$M = sup_R f, \quad and \; \varepsilon = f(a(s),b(t)) - f(s,t) \tag{61}$$

$$\because \varepsilon \leq m\frac{k}{N} \qquad \therefore \varepsilon = O(\frac{1}{N}) \tag{62}$$

Equation (60) can be rewritten as

$$\mathcal{E}(\{S\},N) = \int_R \int [1 - \frac{k}{N} f(s,t) + \varepsilon]^N dsdt - \int_R \int [1 - \frac{k}{N} f(s,t) - \frac{k}{N}\varepsilon]^N dsdt \tag{63}$$

Note that

$$[1-\frac{k}{N}f(s,t) - \frac{k}{N}\varepsilon]^N = \sum_{i=0}^{N}\binom{N}{i}(1-\frac{k}{N}f(s,t))^{N-1}(-\frac{k\varepsilon}{N})^i \tag{64}$$

$$since \quad 0 \le [1-(\frac{k}{N})f(s,t)]^N \le 1 \tag{65}$$

Combining Equation (64) and Equation (65) we obtain

$$|[1-\frac{k}{N}f(s,t) - \frac{k}{N}\varepsilon]^N| \le \sum_{i=0}^{N}\binom{N}{i}(\frac{k\varepsilon}{N})^i \tag{66}$$

$$Recall\ that\ \because \varepsilon = O(\frac{1}{N}),\ \therefore (\frac{\varepsilon k}{N})^i \le (\frac{K}{N^2})^i \quad with\ K-constant \ge 0 \tag{67}$$

$$\sum_{i=0}^{N}\binom{N}{i}(\frac{k\varepsilon}{N})^i \le \sum_{i=1}^{N}\frac{N(N-1)\ldots(N-i+1)}{i!}\cdot\frac{K^i}{N^{2i}} = \sum_{i=1}^{N}\frac{(1)(1-\frac{1}{N})\ldots(1-\frac{(i-1)}{N})}{i!}\cdot(\frac{K}{N})^i \tag{68}$$

$$\le \sum_{i=1}^{N}(\frac{K}{N})^i = \frac{(\frac{K}{N})[(\frac{K}{N})^{N+1}-1]}{(\frac{K}{N})-1} = \frac{(\frac{K}{N})^{N+1}-1}{1-(\frac{N}{K})} \tag{69}$$

$$\because \lim_{N\to\infty}\frac{(\frac{K}{N})^{N+1}-1}{1-(\frac{N}{k})} = 0 \quad \therefore \lim_{N\to\infty}[1-\frac{k}{N}f(s,t)]^N = e^{-kf(s,t)} \tag{70}$$

Substituting Equation (70) into Equation (63) yields

$$\mathscr{E}(\{S\},N) = \iint_R e^{-k\,f(s,t)}\,ds\,dt \tag{71}$$

In the case where $\{k = NW =$ total projection area$\}$, we can define a pseudo area index ($PAI=k/A$). Equation (71) becomes

$$\frac{1}{A}\iint_R e^{-A\cdot PAI\cdot f(s,t)}\,ds\,dt \tag{72}$$

Multispectral Transformation

Mathematical basis of spectral signature and spectral indices

The main purpose of the multispectral transformation is to either reduce the dimensionality of the original data or generate greater separability for class labeling. The characteristics of multi-dimensional feature space is shown in Figure 6 and Figure 7. In the case of 2-dimensional (Figure 6) feature space each region is subdivided into non-overlapping regions and labelled in terms of a real world object such as potato, corn,..etc. To express the process in a more mathematical way, let $X = (x_1,x_2, \ldots ,x_n)$ be a set of n pixels, and $W = \{w_1,w_2, \ldots ,w_m\}$ be a set of feature names. An identification operator A can map X_i into W such that

$$A_j : (x_1,x_2,\ldots.x_n) \rightarrow W_j \qquad (73)$$

During the pixel mapping, different features can be labelled with some uncertainty. The procedure reduces the [*n pixels of q bits data*] to a correspondent bit. Taking a closer look at the dryland wheat cluster in Figure 6, no specific conclusion about spectral variation can be drawn. Representation complexity is greatly reduced but none of the qualitative and quantitative information is provided.

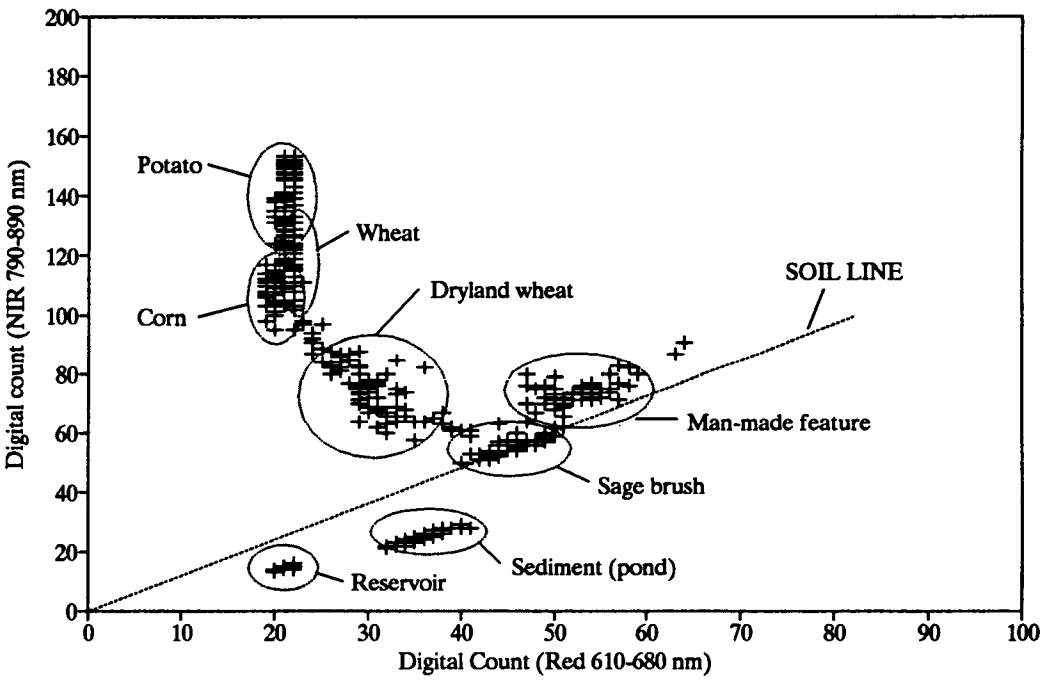

Figure 6. Diagram of multispectral feature space (*SPOT HRV* 6/10/88)

If another feature vector (in this case, ***SPOT HRV Green band***) is added to the 2-dimensional feature space in Figure 7, additional information can be extracted. High NIR and low red reflectance are accompanied by increasing green reflectance which suggests an increase in green biomass as shown in Figure 7.

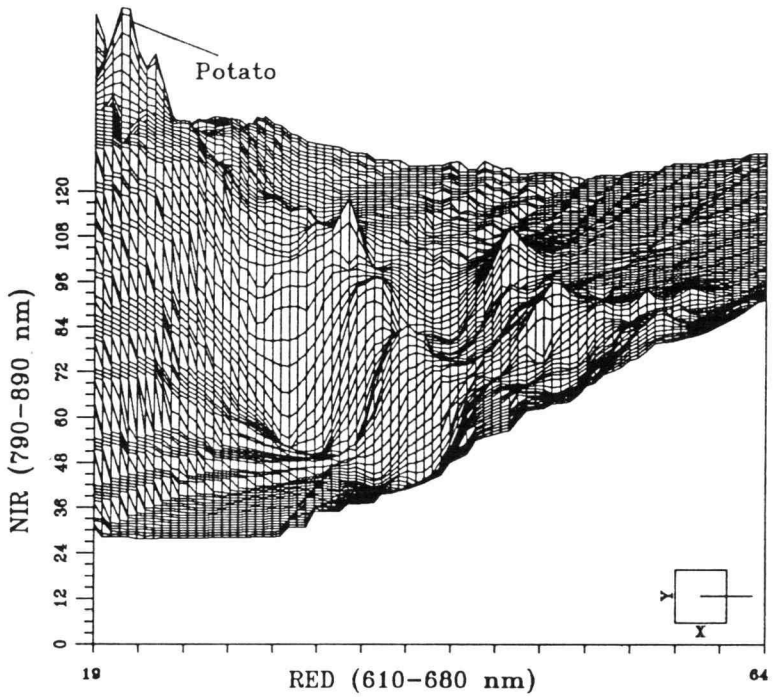

Figure 7. Diagram of 3-dimensional multispectral feature space (***SPOT HRV*** 6/10/88)

The unique feature vectors from multispectral sensing devices enable the use of spectral transformation to create new sets of image components or channels. The derived components represent alternative descriptions of the original image. With appropriate mathematical constraints, the new components can be related to the original spectral reflectance through linear combinations. The multispectral nature of the remote sensing image is accommodated by constructing a vector space with as many axes (or dimensions) as there are spectral components associated with each pixel. Many methods are available to reduce or translate the pixel value in the feature space. In general, the methods can be categorized as pure statistical and semi-empirical indices. Methods such as principal component transformation or zero correlation rotational transformation are general purpose statistical procedures and cannot provide a systematic approach to extract specific information from feature space. Semi-empirical indices are usually developed for certain applications and require local calibrations.

Orthogonal process

Given a function with the following form

$$f(x) = C_1\varphi_1(x) + C_2\varphi_2(x) + C_3\varphi_3(x) + \ldots + C_n\varphi_n(x) \tag{74}$$

Multiply the above equation by φ_m to obtain

$$f(x)\varphi_m(x) = C_1\varphi_1(x)\varphi_m(x) + C_2\varphi_2(x)\varphi_m(x) + C_3\varphi_3(x)\varphi_m(x) + \ldots + C_n\varphi_n(x)\varphi_m(x) \tag{75}$$

By integration

$$\int_a^b f(x)\varphi_m(x)dx = \int_a^b C_1\varphi_1(x)\varphi_m(x)dx + \int_a^b C_2\varphi_2(x)\varphi_m(x)dx + \ldots + \int_a^b C_m\varphi_m(x)\varphi_m(x)dx + \ldots \tag{76}$$

The properties of an orthogonal system implies that if $\varphi_n(x)$ is an orthogonal series then

$$\int_a^b \varphi_m(x)\varphi_n(x)dx = 0 \qquad \forall\, m \neq n \tag{77}$$

Equation (76) can then be simplified as

$$\int_a^b \varphi_m(x)f(x)dx = C_m \int_a^b [\varphi_m(x)]^2 dx \tag{78}$$

$$\text{Let} \quad \int_a^b [\varphi_m(x)]^2 dx = k_n \tag{79}$$

$$\int_a^b \varphi_n(x)f(x)dx = C_n k_n \tag{80}$$

We can then calculate C_n by

$$C_n = \frac{1}{k_n}\int_a^b \varphi_n(x)f(x)dx \qquad \text{where} \quad k_n = \int_a^b [\varphi_m(x)]^2 dx \tag{81}$$

In general, an orthogonal system is conveniently defined with $k_n = 1$, which implies a normalization will be required for each vector.

Gram-Schmidt orthogonalization process

The Gram-Schmidt process can be used to construct a set of linearly combined vectors which will bring out the most observable feature from spectral vector space. Using the vector inner product concept we can define

$$(f,g) = \int_a^b f(x)g(x)dx \tag{82}$$

The following rules exist

$$(f \cdot g) = (g,f) \tag{83}$$

$$(f,g+h) = (f,g) + (f,h) \tag{84}$$

$$(cf,g) = (f,cg) = c(f,g) \tag{85}$$

Assume f and g is an arbitrary pair of vectors that is neither orthogonal nor parallel to each other. We can write a equation in the vector space such that

$$g = \alpha f + \beta u \tag{86}$$

Where α, β are coefficients to be determined, and u is a normalized vector required to be orthogonal to f. Two coefficients α and β can be readily found

$$\begin{aligned} f*g &= \alpha \\ u*g &= \beta \end{aligned} \tag{87}$$

and yield

$$\beta u = g - \alpha f = g - (f*g)f \tag{88}$$

The above procedures create a pair of linear combinations of the two vectors which are mutually orthogonal. We can continue to apply this procedure to an arbitrary set of vectors. Defining a set of independent variables

$$C_0 f_0 + C_1 f_1 + C_2 f_2 + \ldots = 0 \tag{89}$$

Assume the set of vectors are not orthogonal to each other, a new set of coefficients can be defined to force the orthogonalization. The coefficients are formulated as

$$
\begin{aligned}
g_0 &= f_0 \\
g_1 &= k_{1,0} f_0 \\
g_2 &= k_{2,0} f_0 + k_{2,1} f_1 + f_2 \\
&\vdots \\
g_n &= k_{n,0} f_0 + \cdots + k_{n,n-1} f_{n-1} + f_n
\end{aligned}
\tag{90}
$$

Solving the above linear system of equations for k_{ij} as

$$
\begin{aligned}
g_0 &= f_0 \\
g_1 &= f_1 - \frac{(f_1, g_0)}{(g_0, g_0)} g_0 \\
g_2 &= f_2 - \frac{(f_2, g_0)}{(g_0, g_0)} g_0 - \frac{(f_2, g_1)}{(g_1, g_1)} g_1 \\
&\vdots \\
g_n &= f_n - \frac{(f_n, g_0)}{(g_0, g_0)} g_0 - \cdots - \frac{(f_n, g_{n-1})}{(g_{n-1}, g_{n-1})} g_{n-1}
\end{aligned}
\tag{91}
$$

The general mathematical procedures can be presented in the following readily applicable form

(1) calculate $\hat{g}_1 = \dfrac{f_1}{|f_1|}$

(2) calculate $g_2 = f_2 - (\hat{g}_1 \cdot f_2)\,\hat{g}_1$

(3) calculate $\hat{g}_2 = \dfrac{g_2}{|g_2|}$

(4) calculate $g_3 = f_3 - (\hat{g}_1 \cdot f_3)\hat{g}_1 - (\hat{g}_2 \cdot f_3)\,\hat{g}_2$

(5) calculate $\hat{g}_3 = \dfrac{g_3}{|g_3|}$

(6) continue the same procedure for $g_m = f_m - (\hat{g}_1 \cdot f_m)\hat{g}_1 - (\hat{g}_2 \cdot f_m)\hat{g}_2 \cdots -(\hat{g}_{m-1} \cdot f_m)\hat{g}_{m-1}$

(92)

The orthogonal processes have been used for satellite image processing to calculate vegetation indices such as the perpendicular vegetation index (*PVI*) and Tasselled Cap transformation. Certain mathematical and statistical aspects of orthogonal processes have always been neglected. The consequences have been the main reason leading to the misuse of vegetation indices. The orthogonal processes derived vegetation indices are usually compared to results from statistical analysis such as the principal component transform (*PCT*). Fundamental differences must be addressed in order to quantify the spectral variability obtained from these procedures. The orthogonal processes and *PCT* are similar in the way the final transformation is presented

$$T_j = W_i P_i + C_i \tag{93}$$

where

T_j : value (or position) of j^{th} pixel in i^{th} transformation axis

W_i : weights matrix of transformation i (94)

P_i : i^{th} pixel from the input matrix

C_i : constant associated with each transformation axis

The C_i term is used to offset or scale the transformation values when a negative number is encountered (a common result from zero correlation - rotational transform). To prove the offset does not affect the statistical properties of transformation, define $T = T' + T_0$ where T_0 is the location of new origin. The covariance of the new coordinate system is

$$\begin{aligned} & S_{T'} = \mathcal{E}\{(T' - M_{T'})(T' - M_{T'})^t\} \\ & \because M_{T'} = M_T - T_0 \quad \rightarrow T' - M_{T'} = T - T_0 - M_t + T_0 = T - M_T \\ & \therefore S_{T'} = S_T \end{aligned} \tag{95}$$

The covariance of the data in the principal component axes is not affected by the offset term C_i. The use of the C_i term assures the proper display on digital image processing systems. The mathematical basis for orthogonal processes was described in the previous section. Basic review of the *PCT* will be discussed in the following section.

Karhunen-Loéve transform (Principal component transform)

Algebraically, principal components are linear combinations of the p random variables X_1 , X_2 ,...X_p. Geometrically, these linear combinations represent the selection of a new coordinate axes. The new axes represent the direction with maximum variability and provide a simpler description of the covariance structure. A schematic diagram of a 2-dimensional principal component transformation is shown in Figure 8

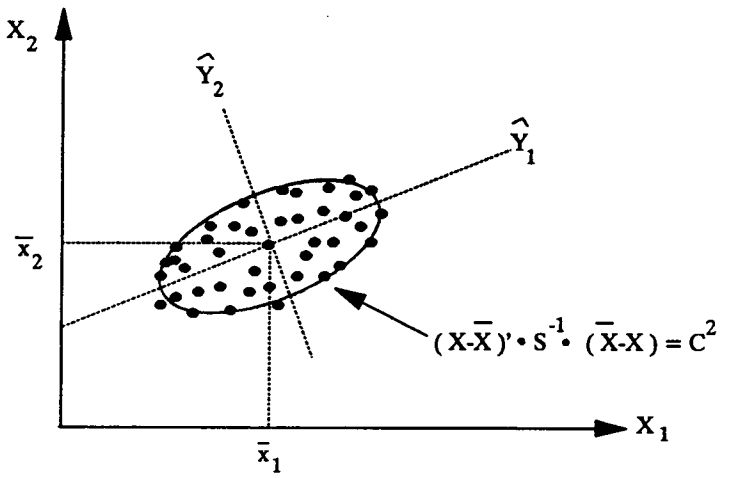

Figure 8. Schematic diagram of principal component transform

The direction of $\hat{Y}_1$ is defined by the correlation between variables X_1 and X_2 and the shape of the ellipse (or ellipsoid in case of p dimensions) enclosing the data points of the variance-covariance matrix computed from 2 (or p) variables. To use the *PCT* for multispectral images, the following procedures are performed:

(1) Compute the variance-covariance matrix S (p x p) from all p spectral bands (correlation matrix should be used in the case when digital numbers are used),

(2) Calculate the eigenvalues for matrix S, the eigenvalues give the length of principal axes of the ellipsoid,

(3) Calculate the eigenvectors from each associated eigenvalue, the eigenvector defines the direction of its associated principal axis,

(4) Use eigenvectors to construct the weight matrix W_i for equation $T_j = W_i P_i + C_i$.

The principal axes that contain small variabilities are usually discarded in statistical applications. This is another common mistake made by remote sensing researchers. In the course of preparing this thesis, some important feature variabilities have been found embedded in components with small eigenvalues. This is due to the multispectral data collected by satellite or imaging spectro-radiometer sensors usually do not comprise a single statistical population which has a unique distribution that can be enclosed by an ellipsoid (Figure 9).

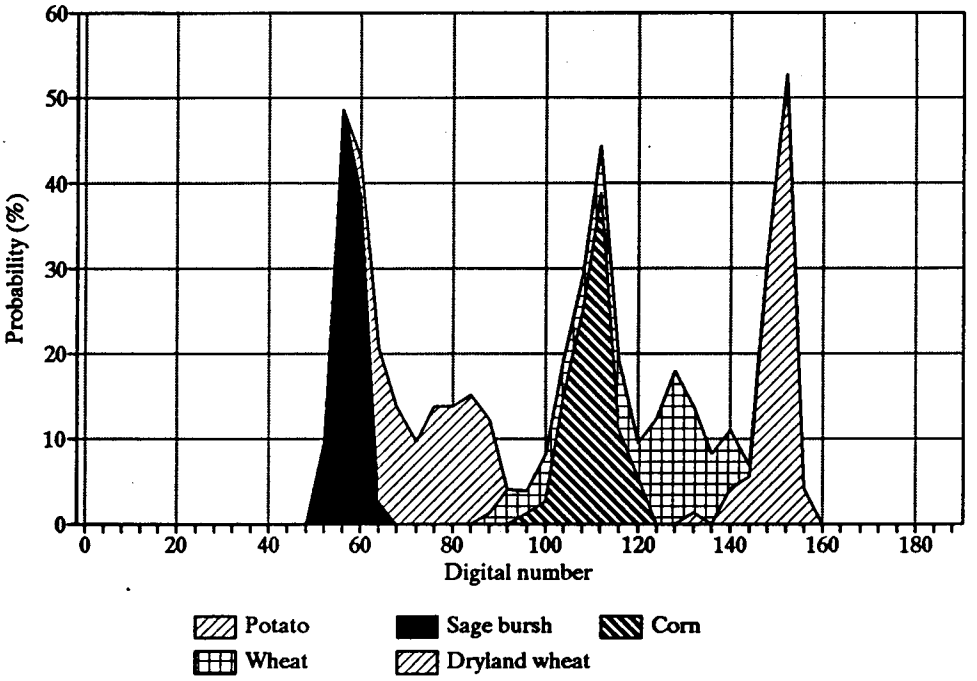

Figure 9. Probability distribution of selected features from *SPOT* (6/10/88) scene

Certain procedures are required to reduce the probability that a low eigenvalue component which contains important information is discarded. The decompositions of wheat and dryland wheat classes in Figure 6 indicate that the selected features follow a multidimensional normal distribution. A modification of class conditional probability is therefore required. In the case of a single dimensional spectral feature space, the normal probability distribution is described by

$$p(x|\omega_i) = (2\pi)^{-\frac{1}{2}} \sigma_i^{-1} \exp\left\{-\frac{1}{2}\frac{(x-\mu_i)^2}{\sigma_i^2}\right\} \qquad (96)$$

where

x : single spectral value

μ_i : mean of x

σ_i^2 : variance of x ,with an unbiased estimate (97)

$$\sigma_i^2 = \frac{1}{n_i - 1} \sum_{j=1}^{n_i} (x_j - \mu_i)^2 , \quad n_i : \text{number of pixels in class } \omega_i$$

The univariate case can be converted to account for the multidimensional case using the following procedures

(1) Replace the univariate spectral variable x by X which is a multidimensional variable

(2) Replace the univariate mean μ_i by multivariate mean M_i

(3) Replace the variance ${\sigma_i}^2$ by covariance matrix S_i such that multi-dimensionality and the effect of between band correlation are both included. S_i is defined as

$$S_i = \mathcal{E}\{(X - M_i)\,(X - M_i)^t\}, \quad \mathcal{E} \text{ is the expected value operator} \tag{98}$$

(4) Compute the unbiased estimate of S_i as

$$S_i = \frac{1}{n_i - 1} \sum_{j=1}^{n_i} [(X_j - M i)\,(X_j - M_i)^t] \tag{99}$$

(5) Compute the multidimensional version of $(x - \mu_i)^2$ by $(X - M_i)^t (X - M_i)$

(6) Perform the following replacement

$$(2\pi)^{-\frac{1}{2}} \sigma_i^{-1} \rightarrow (2\pi)^{-\frac{N}{2}} |S_i|^{\frac{1}{2}} \tag{100}$$

Finally, the multidimensional probability distribution is expressed as

$$p(X|\omega_i) = (2\pi)^{-\frac{N}{2}} |S_i|^{\frac{1}{2}} \exp\left\{-\frac{1}{2}(X - M_i)^t S_i^{-1} (X - M_i)\right\} \tag{101}$$

Relation between orthogonal process-based transforms and Karhunen-Loéve transform (PCT)

The optical characteristics of ground features such as different vegetation types have led to the highly correlated between-band spectral reflectance. The purpose of multispectral transformations are to reduce the dimensionality of ground feature images acquired by an imaging sensor. Among the transformations derived for remotely sensed data, the **Karhunen-Loéve** transform and orthogonal process-based transforms are both statistically robust but also cause a lot of confusion. In the previous section, the theoretical basis of these transforms was discussed. It should be clear that these two types of transforms are fundamentally different in the following aspects

(1) The **Karhunen-Loéve** transform is defined by the interband correlation. The structure of the variance-covariance matrix determines the shape of an ellipsoid that encloses the scattered data and eventually determines the characteristics of the new coordinate system. The processes of principal component generation is driven by the internal data structure. Principal components from such a transform are therefore unique to the specific data set.

(2) The orthogonal process-based transforms are based on pre-selected external data. Recall from the orthogonal process section that the construction of the orthogonal set is not unique. The transformation weights change with the base vector which is subjectively pre-selected.

The basic conceptual relation between these transforms is shown in Figure 10. The **Karhunen-Loéve** transform identifies the number of dimensions but does not describe the feature space data structure. The orthogonal process-based transforms describe the feature data structure by defining a set of ***a priori*** functions. Dimensionality information is not available from the transformation results.

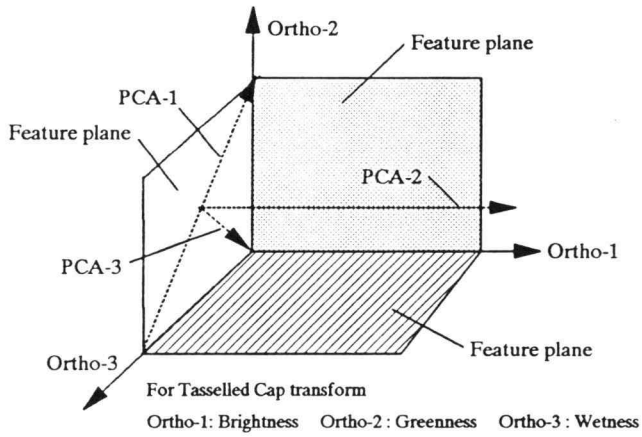

Figure 10. Relation between orthogonal transform and **Karhunen-Loéve** transform

Functional relation between commonly used vegetation indices

The vegetation indices have been developed using band combination, ratioing and other transforms to minimize the variability within data due to external factors. Research results have indicated that the vegetative parameters such as leaf area index (*LAI*), green biomass, percent ground cover (*GC*), absorbed photosynthetically active radiation (*APAR*) productivity, and photosynthetically active tissue can be reasonably estimated using different vegetation indices. Only a few spectral bands are available from satellite platforms today. Since so many different vegetation indices have been derived from a limited number of spectral bands, functional relationships are expected both in mathematical form and as function of spectral characteristics. The following indices are frequently used by researchers from various disciplines. The first category includes the direct band combination

$$\text{RVI} = \frac{r_{red}}{r_{nir}} \quad \text{ratio vegetation index, (Pearson et. al. 1972)}$$

$$\text{NDVI} = \frac{r_{nir} - r_{red}}{r_{nir} + r_{red}} = \frac{\text{RVI} - 1}{\text{RVI} + 1} \quad \text{normalized difference vegetation index, (Rouse et. al. 1972)}$$

$$\text{PVI} = \sqrt{(r_{nir,c} - r_{nir,bg})^2 + (r_{red,c} - r_{red,bg})^2} \quad \text{perpendicular vegetation index, (Richardson 1977}$$

$$\text{SAVI} = \frac{(r_{nir,c} - r_{red,c})}{(r_{nir,c} + r_{red,c} + L)} + (1 + L) \quad \text{soil adjusted vegetation index, (Huete 1988)}$$

$$\text{TSAVI} = \frac{\omega_1 (r_{nir,c} - \omega_1 r_{red,c} - \omega_2)}{(\omega_1 r_{nir,c} + r_{red,c} - \omega_1 \omega_2 + X(1 + a^2))} \quad \text{transformed SAVI, (Baret et. al. 1989)} \tag{102}$$

where

r_{red} : reflectance from red band

r_{nir} : reflectance from near infrared band

c : parameters related to canopy

bg : parameters related to soil background

X : calibration coefficient

ω_i : soil line parameters (103)

The second category includes the indices from mathematical transforms as described in the previous section

$$\text{Brightness} = \sum_{j=1}^{n} a_{1,j}\, r_j$$

$$\text{Greenness} = \sum_{j=1}^{n} a_{2,j}\, r_j$$

$$\text{Wetness} = \sum_{j=1}^{n} a_{3,j}\, r_j \qquad \text{(Kauth et. al. 1976)} \qquad (104)$$

$$\text{Intensity(I)} = R + G + B$$

$$\text{Hue(H)} = \frac{G - B}{I - 3B}$$

$$\text{Saturation(S)} = \frac{I - 3B}{I}$$

where

$a_{i,j}$: weighing coefficients for index i & band j from Gram-Schmidt transformation matri

n : number of bands

r_i : reflectanc from band i

R : band reflectance displayed in red channel

G : band reflectance displayed in green channel

B : band reflectance displayed in blue channel

(105)

The relation between selected vegetation indices calculated from SPOT satellite image is presented in Figure A.5 (Appendices)

Relation between spectral indices and phenological parameters

One of the important applications in remote sensing of vegetation is to study plant dynamic behavior throughout a growing cycle and to monitor phenological conditions. The variation in canopy spectral signature as a function of ground cover and leaf structure is therefore of particular interest. With the advent of new technology and the increasing requirement of frequent coverage and large scale ground information, remote sensing has drawn attention from hydrologists, foresters, agronomists, geographers, botanists and others. Even though each of these fields emphasizes certain aspects of the problem, ranging from development of regional water resource management to the modeling of plant physiological processes, the interaction between radiant energy and the vegetation canopy is usually the basis for different applications.

A spectral (or radiometric) signature is basically the average reflectivity of the surface over a specific bandwidth in the spectrum. The spectral signature is likely to vary with respect to different surface cover compositions since the surface unit does not always contain homogeneous cover types. Consider the simple situation of a field partially covered by vegetation. Assume G is the fraction of ground covered by the vegetation. If the reflectance index (single spectral band, band ratio or other combination) of the soil background is r_s and the reflectance of the vegetation canopy r_c, the composite reflectance measured by the remote sensor is equal to

$$r = r_c G + r_s(1-G) \tag{106}$$

The generic equation above can be applied to any wave bands of interest. The effective penetration depth for different wavelengths within a canopy was categorized as shown in Figure 11.

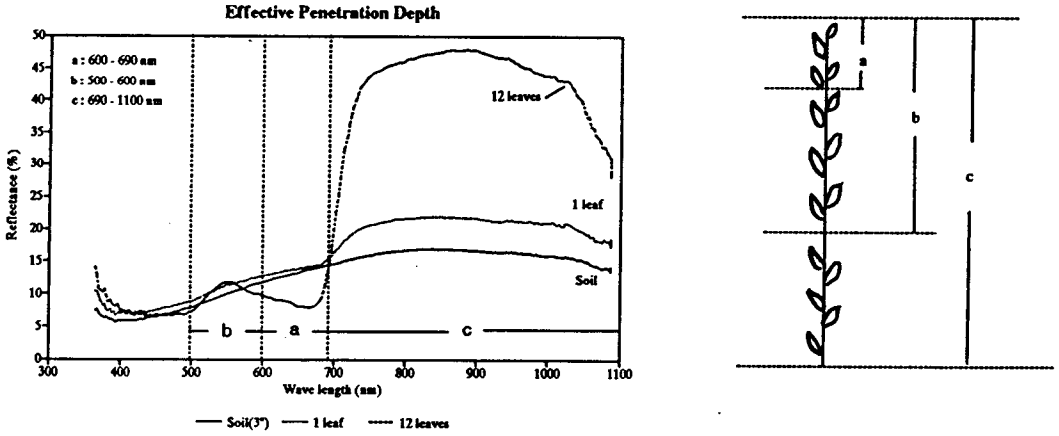

Figure 11. Effective penetration depth for different wavelengths within a typical canopy

The approximation is used to provide general guideline for the formulation of ground cover and spectral reflectance relations. The range labelled as "a" in Figure 11 has a valley around 660 nm (.66 μm) which is known as the major chlorophyll-a absorption region. The absorption of radiation by green vegetation is wave-length dependent and is usually characterized by the spectral absorption coefficient. In terms of absorbed solar energy, the interaction between plant stand and solar radiation can be categorized as follows:

(1) Radiation in thermal forms : approximately 70% of solar energy absorbed by the plant is converted to heat to provide the energy for transpiration and to maintain plant temperature.

(2) Radiation for photosynthesis: up to 28% of absorbed solar energy (in the spectral region .38-.71 μm) is used for photosynthesis and stored in high energy organic compounds in chemical form.

(3) Radiation for photomorphogenetic processes: photomorphogenetically active radiation begins in the ultraviolet and ends in near infrared. It performs the role of a regulator in the process of growth and development.

The top layer canopy reflectance and transmittance are low due to the high chlorophyll absorption in the visible wavelengths. Subsequent reflection and transmission below the top canopy layer can then be ignored. The spectral radiance at the top canopy layer in the visible range is therefore approximated in terms of reflectance and transmittance. A general solution of canopy absorption can be derived from Maxwell equations assuming the leaf is a homogeneous, isotropic, and non-magnetic media. Rewriting the Maxwell equations for a homogeneous canopy as

$$\nabla \boldsymbol{E} - \mu_0 e_0 \mu_r e_r \frac{\partial^2 \boldsymbol{E}}{\partial t^2} = 0 \tag{107}$$

where

$\boldsymbol{E}$: energy vector

μ_0, e_0 : permeability and permittivity of vacuum (108)

μ_r, e_r : relative permeability and permittivity

In case of a sinusoidal field such as the electromagnetic field in a remote sensing spectrum, the above equation can be simplified as

$$\nabla^2 E + \frac{\omega^2}{C_r^2} E = 0 \tag{109}$$

where

$$C_r : \frac{1}{\sqrt{\mu_0 e_0 \mu_r e_r}} = \frac{C}{\sqrt{\mu_r e_r}}$$

ω : angular frequency

C : speed of light (110)

The general solution for the above differential equation is

$$E = A e^{i(k_r - \omega t + \phi)} \tag{111}$$

where

A : wave amplitude

ϕ : phase angle

k_r : wave vector in propagation medium, $k_r = \frac{2\pi\sqrt{e_r}}{\lambda}$ (112)

To formulate the penetration depth under vegetation absorption conditions, the refraction index n should be introduced

$$n = \sqrt{e_r} = N_r + iN_i \tag{113}$$

$$k = \sqrt{e_r}\, k_0 = N_r\, k_0 + i\, N_i\, k_0 \tag{114}$$

where

$$k_0 : \frac{2\pi}{\lambda}$$

N_r, N_i : the real and imaginary parts of refraction index n (115)

The field expression from Equation (111) becomes

$$E = A e^{i(N_r k_0 + iN_i k_0)r - i\omega t} = E_0 e^{-N_i k_{0r}} \tag{116}$$

This equation describes the field behavior when absorption occurs within the medium. The energy

(or field) decreases exponentially as its intensity is absorbed by the medium. The "*skin*" depth d is defined as the thickness at which the field energy is reduced by a factor of e^{-1}

$$d = \frac{1}{2N_i k_0} = \frac{\lambda}{4\pi N_i} \tag{117}$$

It is clear that the penetration depth increases as the wavelength increases. The expression explains why the near infrared band is a better indicator of canopy geometry than the visible bands. Equation (117) can be applied to obtain canopy reflectance directly if N_i and k_{0r} are chosen properly. The analysis works well for a canopy close to full cover. To apply the analysis on commonly used remote sensing platforms on partially covered fields, equations will be written for red and green bands as

$$r_g = r_{c,g} \cdot G + r_{s,g} \cdot (1-G) \tag{118}$$

$$r_r = r_{c,r} \cdot G + r_{s,r} \cdot (1-G) \tag{119}$$

According to the basic radiative transfer model, r_c depends on the number of the leaf layers (or *LAI*). This theory implies the nonlinear relationship between canopy reflectance and plant cover. Since *LAI* is an important parameter for vegetative growth models, a preliminary analysis based on physical and mathematical processes will be performed to study the *LAI* and canopy reflectance. The portion of reflectance due to the vegetation canopy can be expressed as

$$r_{vc} = r - r_s(1-G) = r_c \cdot G \tag{120}$$

The range of influence for different wavelengths within the canopy was previously described in Fig.11. Assume soil reflectance strictly increased with wavelength (Chen, 1991). The ratio of reflectance in green and red bands is essentially independent of the soil conditions. The relation can be written as:

$$\frac{r_{s,g}}{r_{s,r}} = k_1 \tag{121}$$

$$\frac{r_{s,ir}}{r_{s,r}} = k_2 \tag{122}$$

Rewrite Equation (120) for the infrared band as

$$r_{vc,ir} = r_{ir} - r_{s,ir} \cdot (1-G) = r_{c,ir} \cdot G \tag{123}$$

Solving Equations (118), (119), (121), (122), and (123) we obtain

$$r_{vc,ir} = r_{ir} - \frac{k_2 \cdot (r_g \cdot r_{c,r} - r_r \cdot r_{c,g})}{k_1 \cdot r_{c,r} - r_{c,g}} \tag{124}$$

The transmission of beam radiation through a vegetative canopy is a function of leaf area index, the canopy extinction coefficient and the radiation flux over a horizontal surface above the canopy. The beam extinction can be decomposed into the direction of incoming beam radiation and the sensor viewing direction. Consider the extinction process occurs within the canopy. In the visible wavelength regions, extinction happens when the beam radiation encounters a leaf. It can be assumed that the probability of beam radiation hitting *i canopy element within n* independent events has a binomial distribution. Since the number of the cells in a canopy can be considered as infinite (or some very large number), the probability of hitting a specific element will decrease relatively to zero. Assume the number of independent elements of the canopy is a random variable x, the binomial distribution under the above condition becomes a Poisson distribution.

$$P(x=i) = \frac{e^{-\lambda} \cdot \lambda^i}{i!}, \quad i = 0,1,2,..... \tag{125}$$

In the above equation, λ is the expected number of elements in which extinction could occur. It is clear that the probability that no radiation is absorbed (no extinction) is equal to

$$P(x=0) = e^{-\lambda} \tag{126}$$

Assume the extinction in sensor and beam radiation are independent events. The extinction coefficients for sensor direction (K_{sd}) and beam radiation direction (K_{br}) can be introduced and the probability of the sensor seeing the sunlit soil is the product of $e^{-Kbr \cdot LAI}$ and $e^{-Ksd \cdot LAI}$ which is equal to $e^{-(Kbr+Ksd)LAI}$. The apparent canopy cover is therefore equal to

$$G = 1 - e^{-(K_{br}+K_{sd}) \cdot LAI} \tag{127}$$

Substituting Equation (127) into Equation (120) we have

$$r_{vc} = r_c \cdot (1 - e^{-(K_{br}+K_{sd})\, LAI}) \tag{128}$$

A detail theoretical derivations and experimental results on the relation between GC and LAI can be found in a special pilot project report (Chen, 1990).

Feature Extraction in Spatial Frequency Domain

Feature extraction or pattern recognition from remotely sensed data reveal a pronounced performance asymmetry in respect to which texture represents the foreground region and which represents the background. Two distinguishable textural regions occasionally have unique characteristics that make one texture more salient than the other. This characteristic implies that more than local or adjacent textural element analysis should be applied in feature extraction processes. The key point of feature detection is that features of interest must appear with a distinct characteristic within some given area. The magnitude (dimension or spectral reflectance) of a feature signature is generally proportional to either increasing spatial or spectral resolutions. As an observation sensor increases its spectral or spatial resolution, the original homogeneous image cell (pixel) may start to demonstrate a new primitive element. At a certain resolution the feature surface may exhibit an image characteristic which is different from the original image. A similar effect occurs if the resolution is decreased. The feature details may blur to a constant magnitude and the original feature may no longer be discernible. Clearly, the choice of an appropriate resolution is implicit to both qualitative and quantitative processes in feature extraction. Conventionally, the analysis of remotely sensed data utilizes statistical tools that do not distinguish between spatial and spectral feature space. This approach provides reasonable results but apparently is not suitable to handle multi-platform image data from various satellite and aircraft sensors.

Concept of spatial frequency

The image enhancement methods used to extract features from remotely sensed data were derived from spatial domain approaches. Since the ***Spatial Domain*** refers to the aggregate of pixels composing an image, the spatial domain methods therefore operate directly on these pixels. Image processing functions in the spatial domain can be expressed as

$$g(x,y) = T\,[f(x,y)] \tag{129}$$

where $f(x,y)$ is the input image, $g(x,y)$ is the processed image, and T is an operator on f defined over some neighborhood region of (x,y). Due to the low computational cost, the spatial domain methods have dominated the remote sensing digital image processing for the last 15 years. ***Frequency Domain*** methods have been used for non-image data such as radar signal processing, random wave studies, and underwater object detection. The conventional methods used in the discrete inverse problem of image processing require matrix inversion. In the one-dimensional case (signal processing or transect processing of an image), inversion of a square matrix is required. In two dimensional processing, a block matrix inversion is required. This implies that a N^2 by N^2 matrix inversion must be performed

for a N pixel by N pixel image. The matrix inversion requirement has imposed very severe limitations on some stable numerical algorithms and prohibited the practical use, due to limitation in the size of the image, of these algorithms. Recent advances in mathematical theory have allowed the construction of super-resolution images from a blurred source. The method proposed by this research is the ***Fourier transform*** in ***Radon space***. Even though the ***Fourier transform*** is computationally expensive, on a numerical basis, it presents less of a problem than matrix inversion.

Fourier analysis

The Fourier theory allows the representation of a function in terms of its frequency or temporal characteristics and permits easy translation between the two representations. The representation of periodic functions are usually done using ***Fourier Series***, a case that does not occur frequently in the remotely sensed image. Nonperiodic functions (or patterns) are handled through the ***Fourier Transform***. The measurement processes used by the remote sensing platforms to acquire information about continuous functions found in the nature is accomplished by discrete sampling. Apparently, the ***Fourier theory*** provides a tool for investigating the processes of replication and sampling.

Fourier series

Dirichlet originally stated the ***Fourier theorem*** as ***"If a function f(t) is periodic, has a finite number of points of ordinary discontinuity, and has a finite number of maxima and minima in the interval representing the period, then the function can be represented by a Fourier series***

$$f(t) = \frac{a_0}{2} + \sum_{l=1}^{\infty} a_l \cos(l\omega t) + \sum_{l=1}^{\infty} b_l \sin(l\omega t) \tag{130}$$

where the expansion in terms of sine and cosine functions are harmonics with the frequency ω ($\omega = 2\pi/T$), where T is the period of $f(t)$. The coefficients can be calculated as

$$\begin{aligned} a_n &= \frac{\omega}{\pi} \int_{-\pi/\omega}^{\pi/\omega} f(t)\cos n\omega t \, dt \\ b_n &= \frac{\omega}{\pi} \int_{\pi/\omega}^{-\pi/\omega} f(t)\cos n\omega t \, dt \end{aligned} \tag{131}$$

Fourier transforms

Features in remotely sensed images are often nonperiodic. This prohibits the use of Fourier Series for digital image analysis. To extend the Fourier analysis to a ***Fourier transform***, the series are

expressed in exponential form

$$\cos l\omega t = \frac{1}{2}(e^{il\omega t} + e^{-il\omega t})$$
$$\sin l\omega t = \frac{1}{2}(e^{il\omega t} + e^{-il\omega t}) \tag{132}$$

Rewrite Equation (130) as

$$f(t) = \frac{a_0}{2} + \frac{1}{2}\sum_{l=1}^{\infty}(a_l - ib_l)e^{il\omega t} + \frac{1}{2}\sum_{l=1}^{\infty}(a_l + ib_l)e^{-il\omega t} \tag{133}$$

The coefficients within the summations are given by

$$\alpha_{\pm l} = a_l \pm ib_l = \frac{\omega}{\pi}\int_{-\pi/\omega}^{\pi/\omega} f(t)(\cos l\omega t \pm i\sin l\omega t)\,dt$$
$$= \frac{\omega}{\pi}\int_{-\pi/\omega}^{\pi/\omega} f(t)e^{\pm il\omega t}dt \tag{134}$$

Rewrite Equation (133) as a summation over positive and negative values of l

$$f(t) = \sum_{l=-\infty}^{l=\infty}\alpha_l e^{il\omega t} \qquad \text{where} \quad \alpha_l = \frac{\omega}{2\pi}\int_{-\pi/\omega}^{\pi/\omega} f(t)e^{-il\omega t}dt \tag{135}$$

The properties of α_l can be generalized by replacing t by $-t$

$$\alpha_l = \frac{\omega}{2\pi}\int_{-\pi/\omega}^{\pi/\omega} f(-t)e^{il\omega t}\,dt \tag{136}$$

The above equation implies

$$\begin{aligned} \alpha_l &= \alpha_{-l} \quad f(t) \text{ even} \\ \alpha_l &= -\alpha_{-l} \quad f(t) \text{ odd} \\ \alpha_l &\neq \alpha_{-l} \quad f(t) \text{ neither odd nor even} \end{aligned} \tag{137}$$

Unlike the ***Fourier series*** where $f(t)$ is required to be periodic, $f(t)$ in the case of ***Fourier transforms*** can be nonperiodic functions. Fourier expansion of nonperiodic functions can be made by assuming the

nonperiodic functions are in fact periodic functions with an infinite period. Since $\omega=\pi/T$, if $\omega \rightarrow 0$ then $T \rightarrow \infty$. Since in the limit (∞) the fundamental frequency approaches zero, the summation over discrete harmonics of the fundamental frequency becomes a definite integral over a continuous distribution of frequencies. Define the fundamental frequency as $\Delta\omega$ and rewrite $f(t)$ in terms of $\Delta\omega$

$$f(t) - f(t + \frac{2\pi}{\Delta\omega}) - \frac{1}{2\pi}\sum_{l=-\infty}^{l=\infty}\left\{\int_{-\pi/\Delta\omega}^{\pi/\Delta\omega} f(t)\, e^{-il\Delta\omega t}\, dt\right\} e^{il\Delta\omega t}\Delta\omega \tag{138}$$

The limit is now taken as $\Delta\omega \rightarrow 0$. The harmonics making up the distribution become infinitely close to one another and, in the limit, the discrete set of harmonics can be replaced by a continuous function

$$\lim_{\Delta\omega \rightarrow 0} (l\Delta\omega) - \omega \tag{139}$$

Taking the limit of $f(t)$ yields

$$f(t) - \frac{1}{2\pi}\int_{-\infty}^{\infty}\int_{-\infty}^{\infty} f(\tau)e^{i\omega(t-\tau)}d\tau\, d\omega \tag{140}$$

The ***Fourier transform*** of $f(t)$ can now be defined as

$$\mathcal{F}\{f(t)\} = F(\omega) = \int_{-\infty}^{\infty} f(\tau)e^{-i\omega t}d\tau \tag{141}$$

Information is not destroyed when using a ***Fourier transform*** for temporal to frequency transformation. The transformed information can be recovered using the inverse transform

$$\mathcal{F}^{-1}\{\, F(\omega)\,\} - f(t) - \frac{1}{2\pi}\int_{-\infty}^{\infty} f(\omega)e^{i\omega t}\, d\omega \tag{142}$$

$f(t)$ and $F(\omega)$ are called a ***Fourier transform pair***. Until now, the derivation has been limited to the time and frequency domain. Space variables are introduced to the transformation process when spatial analysis is needed such as in remote sensing image analysis. The ***transform*** or ***conjugate*** variable must have reciprocal units. In the case of image processing when the pixel (or its equivalent ground resolution) is used the conjugate unit would be ***pixel*** (or ***meter***) and its reciprocal ***pixel***$^{-1}$ (or m^{-1}). The conjugate variable to the space variable is called ***spatial frequency***. There are many important properties associated with the ***Fourier transform*** which are described in many mathematical references.

Convolution integral and ***Linear system theory*** are two key properties which require special attention when applying the ***Fourier transform*** in ***Radon space.***

Convolution integral

A ***Convolution integral*** are generally expressed in the following form

$$g(\tau) = a(t) \otimes b(t) = \int_{-\infty}^{\infty} a(t)b(\tau - t)dt \tag{143}$$

This integral is called a ***faltung*** or ***folding*** integral because the function $b(t)$ is folded over the ordinate before the integration is performed. The weighing function $b(\tau-t)$, called the ***convolution kernel***, is a window that moves in time (or conjugate unit) through which we are observing the function $a(t)$. The convolution is the average of the temporal function $a(t)$ viewed through this window. The convolution integral is different from the ***correlation integral*** which has a form

$$h(\tau) = a(t) \oplus b(t) = \int_{-\infty}^{\infty} a(t)\, b^*(t-\tau)dt \tag{144}$$

where $a(t)$ and $b(t)$ are different functions and b^* is the conjugate. One major difference is that the correlation operation does not commute (information passing) while the convolution does. The relation between convolution and correlation can be described by a simple equation

$$a(t) \oplus b(t) = a(t) \otimes b^*(-t) \tag{145}$$

The correlation and convolution functions are identical if the weighing function $b(t)$ is a real, even function. This is an important property for information extraction from vegetation indices derived from remotely sensed data. The mathematical operations are simplified since the Fourier transform allows us to write the Fourier transform of the convolution as the product of the Fourier transforms of the two functions

$$\mathcal{F}\{a(t) \otimes b(t)\} = \mathcal{F}\left\{\int_{-\infty}^{\infty} a(t)b(\tau - t)dt\right\} = A(\omega)B(\omega) \tag{146}$$

The above property provides an efficient way to manage the complicated mathematical operation efficiency in remote sensing image extraction.

Linear system theory

The electromagnetic wave passing through the atmosphere is projected onto the vegetation or other

ground features and reflected back to the sensors on remote sensing platforms. They are many theories which describes the possible physical processes. To simplify the analysis we can assume each energy transfer step is a linear system. With this assumption we can characterize a linear system by determining its response to a delta function input. The output of the linear system to an arbitrary input function is the convolution of the input function and the delta function response. The importance of such a property becomes clear as we shall discuss under ***sensor dynamics*** in the following section. A mathematical operator Γ maps the input function $f(t)$ onto the output function $g(t)$

$$\Gamma\{ f_1 \} \rightarrow g_1(t), \quad \Gamma\{ f_2 \} \rightarrow g_2(t) \tag{147}$$

To study the invariant properties embedded through scaling processes, assume the operator is linear, stationary, and homogeneous

$$\begin{aligned} \Gamma\{af_1(t)\} &\rightarrow ag_1(t) && \text{: homogeneous} \\ \Gamma\{ af_1(t) + bf_2 \} &\rightarrow ag_1(t) + bg_2(t) && \text{: linearity} \\ \Gamma\{ f_1(t - t_0) \} &\rightarrow g_1(t - t_0) && \text{: stationary} \end{aligned} \tag{148}$$

The relationships are based on the principle of superposition which allows the decomposition of a complex input into a linear combination of simple functions. When a delta function is used as an input into the linear system, we obtain

$$\Gamma\{\delta(t)\} \rightarrow s(t) \tag{149}$$

$s(t)$ is called ***Green's function*** or the ***Point spread function*** in the case of image processing. For a large set of delta function responses we have

$$\Gamma\{ f(t_1)\delta(t-t_1)+ f(t_2)\delta(t-t_2) \} \rightarrow f(t_1)s(t-t_1) + f(t_2)s(t-t_2) \tag{150}$$

where $f(t_1)$ and $f(t_2)$ are eigenfunctions of linear operator Γ. The above equation can be expanded to

$$\Gamma\left\{ \sum_{n=1}^{N} f(t_n)\delta(t-t_n) \right\} \rightarrow \sum_{n=1}^{N} f(t_n)s(t-t_n) \tag{151}$$

The following input function

$$\Gamma\left\{ \int f(t')\delta(t-t')dt' \right\} \tag{152}$$

can be decomposed using the ***sifting property*** of the delta function

$$f(t) = \int f(t')\delta(t' - t_1)dt' \tag{153}$$

The superposition integral is derived by

$$\Gamma\left\{ \int f(t')\delta(t-t_1)dt' \right\} = \int f(t')\Gamma\{\delta(t-t')\} = \int f(t')s(t-t')dt' \tag{154}$$

Radon transform

The resampling procedure used in the scale information extraction requires approximating continuous inverse problems in a discrete manner. Menke (1989) described the use of Radon Transform for simple tomography problem. The general form of the continuous inverse problem is

$$d_i = \int_a^b G_i(z)m(z)dz \tag{155}$$

A continuous inverse problem can be converted into a discrete event with the assumption that the model function of a physical process can be represented by a finite number M of coefficients

$$m(x) \sim \sum_{j-1}^{M} m_j f_j(x) \tag{156}$$

The data kernel for a two (or more) variable transect (or slicing) processing has a form of

$$d_i = \int_{C_i} m[x(s),y(s)]ds \tag{157}$$

The data kernel is integrated along a transect C_i that has arc length s. Define an image processing operator ρ which can operate on both one- and two-dimensions. Assume an image is separable such that

$$I(x,y) = I_x(x)I_y(y) \tag{158}$$

The operator ρ can be applied using

$$\rho_2 = I(x,y) = \rho_1 I_x(x)\rho_1 I_y(y) \tag{159}$$

where ρ_2 represents ρ operating in a two-dimensional situation. The approach is used to overcome the difficulty of using a two-dimensional process that presents computational problems. Mathematically, this operation should be restricted to images that are separable. Researchers often

use parallel stripping processing to relax this constraint. The relaxation might work fine in some cases but is technically incorrect. The concept behind the ***Radon transform*** is to provide a method to reduce the dimensionality without assuming separability. The Radon transform operator is given by

$$\mathfrak{R} = \int\int \delta(z-(x^2 + y^2)^{1/2}\cos\theta \tag{160}$$

This equation demonstrates the process of a ***Radon transform*** which converts a digital image into a sequence of one dimensional arrays. Figure 12 illustrates the parameterization of a transect through an image. The transect is parameterized by the perpendicular distance u from the origin and depression angle θ between the transect line and x-axis. Any point on the transect can be expressed by

$$\begin{pmatrix} x \\ y \end{pmatrix} = \begin{pmatrix} \cos\theta & -\sin\theta \\ \sin\theta & \cos\theta \end{pmatrix} \begin{pmatrix} u \\ s \end{pmatrix}$$
$$\begin{pmatrix} u \\ s \end{pmatrix} = \begin{pmatrix} \cos\theta & \sin\theta \\ -\sin\theta & \cos\theta \end{pmatrix} \begin{pmatrix} x \\ y \end{pmatrix} \tag{161}$$

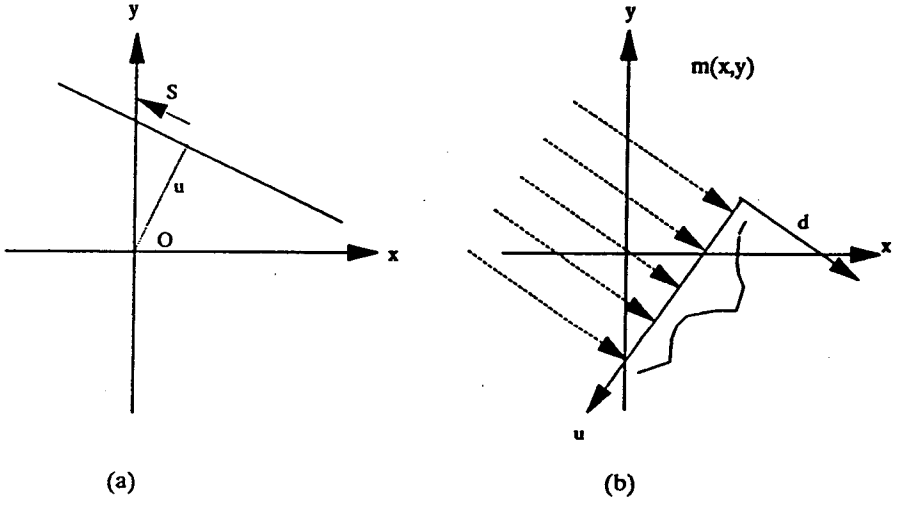

Figure 12. (a) Integration direction in Radon transform, (b) Slicing projection (from Menke,1989)

Rewrite the data kernel d_i in terms of the transformation as

$$d(u,\theta) = \int_{-\infty}^{\infty} m[x - u\cos\theta - s\sin\theta, y - u\sin\theta + s\cos\theta]ds \tag{162}$$

The Radon transform is mathematically similar to the Fourier transform. The *Fourier transform pair* used to transform between spatial position x and spatial frequency k_x is

$$F(k_x) = \int_{-\infty}^{\infty} f(x)e^{ik_x x}dx \tag{163}$$

$$f(x) = \frac{1}{2\pi}\int_{-\infty}^{\infty} F(k_x)e^{-ik_x x}dx \tag{164}$$

Taking the Fourier transform of the data kernel function d_i equation with respect to $u \rightarrow k_u$

$$\mathcal{F}\{d(k_u,\theta)\} = \int_{-\infty}^{\infty}\int_{-\infty}^{\infty} m[x - u\cos\theta - s\sin\theta,\ y - u\sin\theta + s\sin\theta)ds e^{ik_u u}du \tag{165}$$

Taking the transform of the double integral from ***ds du*** to ***dx dy*** we can rearrange the equation as

$$\begin{aligned}\hat{d}(k_u,\theta) = \mathcal{F}\{d(k_u,\theta)\} &= \int_{-\infty}^{\infty}\int_{-\infty}^{\infty} m(x,y)e^{ik_u\cos\theta x + ik_u\sin\theta y}dxdy \\ &= \mathcal{F}\{\mathcal{F}\{(k_x - k_u\cos\theta,\ k_y - k_u\sin\theta)\}\}\end{aligned} \tag{166}$$

This procedure provides a way to invert the Radon transform. The last equation simply represents a Fourier transformed image evaluated along radial lines in the (k_x, k_y) plane. The Fourier transformed image is known for all (k_x, k_y) if the Radon transform is known for all the values of (u,θ). The spatial domain image $m(x,y)$ can be reconstructed by taking the inverse Fourier transform. One important property about this procedure is that "***Since the Fourier transform and its inverse are unique, the Radon transform can therefore be uniquely inverted if it is known for all possible*** (u,θ)". The slicing characteristics of the Radon transform also make it a good candidate for a *discrete Fourier transform*.

Discrete Fourier transform in spatial frequency domain

The *spatial frequency* is the image analog of the frequency of a signal in time. A sinusoidal signal with high frequency alternates rapidly, whereas a low frequency signal changes slowly with time. Similarly, an image with high spatial frequency in the horizontal direction exhibits frequent changes of brightness with position horizontally. The foundation of spatial frequency domain techniques is the

convolution theorem which was discussed in the previous section. Let ***g(x,y)*** be an image formed by the convolution of an image ***f(x,y)*** and a position invariant operator ***h(x,y)***, that is

$$g(x,y) = h(x,y) * f(x,y) \tag{167}$$

The following relation holds in case of ***Fourier transforms***

$$G(u,v) = H(u,v)F(u,v) \tag{168}$$

Where ***G, H,*** and ***F*** are the Fourier transforms of ***g, h,*** and ***f,*** respectively. In the previous section we also discussed the theoretical background of ***Multispectral Transforms.*** The eigenvectors associated with the principal component, the coefficients of the Tasselled Cap functions, and discriminant analysis transformations define new coordinate axes in the multidimensional space containing the multispectral data. The data are expressed in terms of the new coordinate axes which could be used to bring out certain features of interest. The ***Fourier Transform*** operates on a monotone (single band) image. The transform breaks down the image into scale components, which are defined in terms of sinusoidal waves with varying amplitudes, frequencies, and directions. The coordinates of the two-dimensional space are given in terms of frequency (i.e. cycle/basic interval). The following figure (Figure 13) illustrates the spatial and frequency domain representation of a digital image.

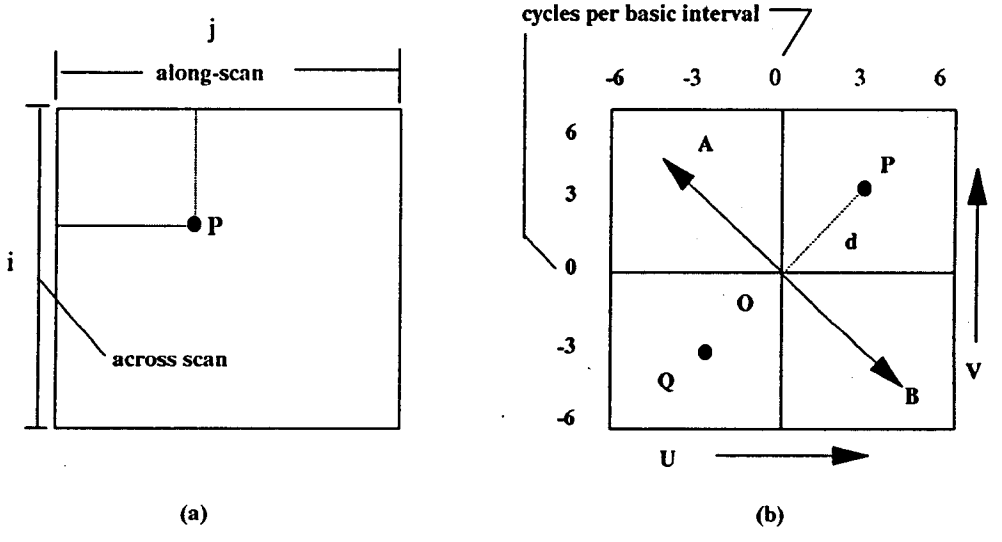

Figure 13. (a) Spatial domain, (b) Spatial-Frequency domain representation of an image

Consider a three dimensional feature surface generated from a single band digital image where x and y axes are the rows and columns in the image with the brightness value of each pixel as the third dimension. A series of waveforms of increasing frequency are fitted to the brightness surface.

Information associated with each waveform is calculated. The calculated information provides (1) the frequency of each of the scale components of the image, and (2) the proportion of information associated with each frequency component.

Consider an infinite periodic sequence of impulses in the frequency domain spaced Δf ($\Delta\omega/2\pi$) apart. The inverse transform of this sequence is another sequence of impulses in the time domain, spaced T_0 ($=1/\Delta f$) apart. If the periodic spectrum $F(\omega)$ (Fourier transform of $f(t)$) is multiplied by the frequency domain sampling function, the convolution theorem states that samples of $f(t)$ will be formed into a periodic sequence with period T_0. Assume the spectrum is represented by a number of K samples. Since the time domain has samples spaced T apart, the duration of sampling is KT. Let $\phi(k)$ (k=0, 1, . . . , K-1) be a set of K samples taken from $f(t)$ over the sampling period 0 to T_0. Let $F(r)$ (r=0,1,..,K-1) represent a set of samples of frequency spectrum. The continuous function $f(t)$ is replaced by the samples $\phi(k)$ and $2\pi f$ is replaced by $2\pi r\Delta f$ (with r = 0, 1, . . , K-1 and $\omega=2\pi r/T_0$.) The time variable t is replaced by kT (= kT_0 /K k=0, 1, . . ., K-1). The Fourier transform pair can be expressed in a discrete form as

$$F(r) = T\sum_{k=0}^{K-1}\phi(k)e^{-(j2\pi/K)rk}, \qquad r = 0,\ldots K-1$$
$$\phi(k) = \frac{1}{T_0}\sum_{r=0}^{K-1}F(r)e^{-j2\pi rk/K}, \qquad k = 0,\ldots,K-1 \tag{169}$$

The ***discrete inverse Fourier transform*** (the second equation) can be rearranged as

$$\begin{aligned}\phi(l) &= \frac{1}{T_0}\sum_{r=0}^{K-1}F(r)e^{-j2\pi rl/K}\\ &= \frac{1}{T_0}\sum_{r=0}^{K-1}\cdot T\sum_{k=0}^{K-1}\phi(k)e^{-j2\pi r(k-l)/K}\\ &= \frac{1}{K}\sum_{k=0}^{K-1}\phi(k)\cdot\sum_{r=0}^{K-1}e^{-j2\pi r(k-l)/K}\end{aligned} \tag{170}$$

The second term in the last equation is zero, $\forall k \neq l$; and equals to K, $\forall k=l$. The above constraint implies that $\phi(l)$ can simply be replaced by $\phi(k)$. The final form for Fourier transform pair is

$$F(r) = \sum_{k=0}^{K-1} \phi(k) e^{-j2\pi rk/K}, \quad r = 0,\ldots,K-1$$
$$\phi(k) = \frac{1}{K} \sum_{r=0}^{K-1} F(r) e^{-j2\pi rk/K}, \quad k = 0,\ldots,K-1 \tag{171}$$

Two important properties of the discrete Fourier transform when applied to image processing are *Linearity* and *Symmetry*.

Discrete Fourier transform of a digital image

Fourier transforms need to be rewritten in order to describe an image in discrete spatial frequency domain. Define a sequence $\phi(i, j)$ which represents the brightness of a pixel at location i, j within an image (of size K by K pixels) as

$$\phi(i,j), \quad i,j = 0,\ldots,K-1 \tag{172}$$

The discrete Fourier transform of this image is described by

$$\Phi(r,s) = \sum_{i=0}^{K-1} \sum_{j=0}^{K-1} \phi(i,j) e^{-j2\pi(ir + js)/K} \tag{173}$$

An image can be reconstructed from the above equation by

$$\phi(i,j) = \frac{1}{K^2} \sum_{i=0}^{K-1} \sum_{j=0}^{K-1} \phi(r,s) e^{j2\pi(ir + js)/K} \tag{174}$$

Φ can be rewritten as

$$\Phi(r,s) = \sum_{i=0}^{K-1} e^{-j2\pi ir/K} \sum_{j=0}^{K-1} \phi(i,j)\, e^{-j2\pi js/K} \tag{175}$$

It is clear that the right side of the process is a one-dimensional Fourier transform

$$\Phi(i,s) = \sum_{j=0}^{K-1} \phi(i,j)\, e^{-j2\pi js/K}, \quad i = 0,\ldots,K-1 \tag{176}$$

This one-dimensional property simplifies discrete Fourier transform of an image as

$$\Phi(r,s) = \sum_{i=0}^{K-1} \Phi(i,s)\, e^{-j2\pi ir/K} \tag{177}$$

The procedure to transform an image becomes (1) transform each individual row and generate an intermediate image, and (2) transform the result from (1) by column to yield the final result.

Image information extraction

The relevant details of images exist only over a restricted range of scales. The importance of image structure which affects the level of resolution was discussed in the previous section. Any given image has a limited extent or window (defined as ***outer scale***) as well as a limited resolution (defined as ***inner scale***). These limits are set by either the format of the image, the structure of radiation, or the subject matter. In the case of an image format, the limitations result from the physical characteristics (such as grain size, charge-coupled device (CCD) array spacing, sensor mirror scan angle) of the imaging devices. In the case of ***inner scale***, the determination factor can be the luminance situation. For ***subject matter***, the limiting factor is the relevant scales of different objects. The problem of setting ***outer*** or ***inner scales*** is especially difficult for automated image processing. In satellite image processing, all variable structures need to be retained if no ***a priori*** knowledge is available for certain features. This implies that the image should be treated simultaneously at all levels. A general solution to achieve this goal is to (1) embed the original image with a family (a range of scale) of derived images and (2) analyze relations between structure features in that scale range. In terms of ***inner*** and ***outer*** scales, the inner scale measures the resolution while the outer scale determines how far to proceed. No mathematical formula or theory is available to describe the perception of different levels of resolution. Any image can be uniquely embedded in a resolution family if the constraint is set such that no spurious details should be generated when the resolution is diminished. Theoretically, the diffusion equation with a second order linear parabolic form can be used to describe the structure of this resolution family in a continuous manner. As the resolution decreases the image becomes less articulated because the extremes ("bright" or "dark") disappear one after the other. This is a structure erosion process which is similar in every resolution. Traditionally, the remotely sensed images are analyzed using pixel-based statistical approaches. The most significant drawback has been ***scene dependency*** which makes cross-referencing and temporal analysis very difficult. Applications of texture analysis in remote sensing have been limited due to the lack of computing tools and understanding of the importance of texture. Practically, textures can be analyzed on two levels : ***statistical*** and ***structural***. On a statistical level, a set of statistics are derived from the local features which are defined in terms of reflectance at a specific position relative to each point in the image. Analysis on the structural level is complex but can derive more detailed information with the introduction of neighboring pixels and their statistical descriptions.

First-order statistics

A discrete image array $F(n_1, n_2)$ can be completely characterized statistically by its joint probability density function

$$p(f) = p\{f(1),f(2),.....,f(Q)\}\ , \quad Q = N_1 \cdot N_2 \text{ which is the order of joint density} \tag{178}$$

If all pixel values are statistically independent, the joint density can be factored into the product of its first-order marginal densities as

$$p(f) = p\{f(1)\},p\{f(2)\},....,p\{f(Q)\} \tag{179}$$

The probability distributions of image values can be estimated by histogram measurements with the above characteristics. The first-order histogram estimate of the probability distribution is

$$H_E(j;q) = \frac{N_p(j)}{N_p} \tag{180}$$

Where N_p represents the total number of pixels examined and $N_p(j)$ denotes the number of pixels for which $f(q) = r_j$, (r_j is a set of discrete values) , $j = 0,1,..., j\text{-}1$. If the image source is statistically stationary, the first-order probability distribution will be the same for all vector components q. If the image source is ergodic, then measurements over a collection of images can be replaced by spatial averages. The quality of the image after scale transformation can be examined using first order statistics. The characteristics of the image histogram can also be investigated using first order statistics which are computed around single pixels relative to the population. Two first order statistics selected for investigation are

$$\begin{aligned} &\sum_{i=1}^{n} (i-\mu)^3 p(i) \qquad 3^{rd} \text{ moment} \\ &-\sum_{i=1}^{n} p(i)\log(p(i)) \qquad \text{entropy} \end{aligned} \tag{181}$$

where $p(i)$ is the occurrence probability of pixel value i (either from raw spectral value or transformed image). The reason to perform such analysis is based on the statistical properties of a histogram. The third moment is a measure of histogram skewness. When the histogram is symmetrical, its value is 0. The entropy, on the other hand is a measure of uncertainty. The goal to evaluate feature extraction from multi-scale images is to determine how "close" the features match in different scales. It is important to have a minimum dispersion along any given direction in the measurement space. Small dispersion in the measurement space means less uncertainties in the selected feature. Theoretically, the information content is closely related to the uncertainty. The information content in any given signal is the amount of unpredictable change. If the signal is completely predictable, then it contains no information. Consider a discrete signal collected over a time interval [0,T] such that

the signal is constant over sampling periods of length τ and has values in a discrete set $\{v_0, ..., v_{n-1}\}$. The number of possible signals which can be generated in the given time period is $n^{T/\tau}$. Define the information in period [0,T] to be

$$H = \frac{T}{\tau} \ln n \tag{182}$$

The logarithm can be in any base, but the natural logarithm is most appropriate since base 2 is used in computer communication and the information is measured in bits. If each value in the discrete set is equally likely (a reasonable assumption for signals from remote sensors), the probability of any level is p (=1/n). The above equation becomes

$$H = \frac{T}{\tau} \ln n = -\frac{T}{\tau} \ln p \tag{183}$$

In case when the levels are not equally likely ($p \neq 1/n$), the information content in N intervals is

$$H = -\sum_{i=0}^{n-1} R_i(N) \ln P_i \tag{184}$$

Where $R_i(N)$ is the number of occurrences of v_i in a long series of N trials and p_i is the probability of v_i. The following equality exists in a long series of N trials

$$\lim_{N \to \infty} \frac{R_i(N)}{N} = p_i \tag{185}$$

In T/τ intervals, the information content is equal to

$$H = -\frac{T}{\tau} \sum_{i=0}^{n-1} p_i \ln p_i \tag{186}$$

The continuous version of information content for a feature population with probability density $p(x \mid i) = p_i(x)$ is therefore

$$H = -\int_x p(x \mid i) \ln p(x \mid i) dx = -\xi \{\ln p(x \mid i)\} \tag{187}$$

If $p(x \mid i) = 1$, then $H = 0$ and there is no uncertainty and therefore no information content in the given signal. The entropy is therefore a good measure of the uniformity of the image histogram. The entropy will take its maximum value when the pixel value is uniformly distributed. A stronger theoretical support for using the entropy as a measure of scale variabilities in an image can be

obtained using the following relationship derived by Schroeder (1991). assuming S_q is the moment of order q of the probability p_i

$$S_q := -\frac{1}{q-1} \log \sum_{i=1}^{N} p_i^q , \quad q \in \Re \tag{188}$$

For q→1, the equation becomes

$$S_1 = -\sum_{i=1}^{N} p_i \log p_i \tag{189}$$

Which is the generalized form of entropy defined in the previous section. To take the concept of generalized entropy one step further Schroeder defined a generalized dimension as

$$D_q : \lim_{r \to 0} \frac{1}{q-1} \frac{\log \sum_{i=1}^{N} p_i^q}{\log r} \tag{190}$$

The p_i is now defined as the probability that a random variable falls into the i^{th} class of scale r. For a equally likely event $p_i = 1 / N$, the above equation can be rearranged as

$$D_q : \frac{1}{q-1} \frac{\log N(1/N)^q}{\log r} = \frac{\log N}{\log (1/r)} \tag{191}$$

For q=0, the definition of the equation agrees with the **Hausdorff dimension, D**. The term, D_q was defined as a generalized dimension with the hope that it can be used for scale measurement. Consider a generalized feature generator with line segments r_i and probability p_i which satisfies

$$\lim_{n \to \infty} \left(\sum_{i=1}^{N} p_i^q r_i^\tau \right)^n = c \tag{192}$$

$$\sum_{i=1}^{N} p_i^q r_i^\tau = 1 \tag{193}$$

Rearrange the above equation as

$$\tau = \tau(q) = -\lim_{r \to 0} \frac{\log \sum_{i=1}^{N} p_i^q}{\log r} = (1-q) D_q \tag{194}$$

In case of $q=1$, $\tau(q)=0$ we have D_1 as

$$D_1 = \frac{\sum_{i=1}^{N} p_i \log p_i}{\sum_{i=1}^{N} p_i \log r_i} \tag{195}$$

For $q \to 1$ and $p_i = 1/N$, D_1 becomes

$$D_1 = \lim_{r \to 0} \frac{S_1}{\log r} \tag{196}$$

Where S_1 is the generalized entropy defined in the previous section. This information measure has not yet been used in image analysis. The theoretical link between information entropy and the scale invariant dimension (or fractal characteristics) in a digital image should be apparent since D_1 is essentially derived from a generalized feature generator. The relation between these two information measures was used to extract information content from remotely sensed image.

Fractal dimension

A fractal is defined as a { *set* } for which the ***Hausdorff-Besicovitch*** dimension is strictly larger than its Euclidean dimension (Mandelbrot, 1976). The fractal dimension of a surface is an indicator of the surface roughness. The closer the fractal dimension is to its Euclidean dimension, the smoother the surface. By definition, the fractal dimension of a surface is invariant with respect to linear and scale transformations of surface data. Consider the raw reflectance values or any spectral measures (such as the results from multispectral transformation or the Fourier transform, etc.) from a remotely sensed image as the 3rd dimension on the image plane. If the fractal dimension of a specific measure is invariant to different scales, then the fractal dimension can be used as a basis to compare ***suitability*** of each measure when multi-scale processing is required. It should also provide a ***suitability scale range*** for the specific feature in an image. To show the adequacy of using the fractal dimension as a measure for surface spectral intensity, only one basic proposition needs to be proved. The proposition which was first brought out by Pentland in 1984 states: "A three dimensional surface with a spatially isotropic fractal Brownian shape produces an image whose intensity surface is fractal Brownian and whose fractal dimension is identical to that of the components of the surface's normal, given a Lambertian surface reflectance function and constant illumination and albedo". The proof of this proposition is summarized in the following paragraph with minimum mathematical formulations.

Assume a lambertian surface, the spectral intensity I at any given point P is a function of the surface normal N at the surface point projects to P

$$I = \rho \lambda N \cdot L \tag{197}$$

where ρ is the surface albedo, λ is the illuminant intensity, and $L = (l_x, l_y, l_z)$ is the illuminant direction. The variations in I are dependent on variations in N. The preposition can be defined as

$$Pr\left(\frac{I(x,y) - I(x+\Delta x,y)}{||\Delta x||^H} < y\right) = F(y) \tag{198}$$

To prove the above equation we first assign N_1 to be the normal at point (x,y) and N_2 to be the normal at point (x + Δx ,y). The above equation can be expanded as

$$Pr\left(\frac{\rho \lambda (N_1 \cdot L) - \rho \lambda (N_2 \cdot L)}{||\Delta x||^H} < y\right) = F(y) \tag{199}$$

The equation can be further expanded as

$$Pr\left(\frac{\rho \lambda (N_{1x} l_x + N_{1y} l_y + N_{1z} l_z) - \rho \lambda (N_{2x} l_x + N_{2y} l_y + N_{2z} l_z)}{||\Delta x||^H} < y\right) = F(y) \tag{200}$$

As ρ, λ, L are constant, N_x, N_y, N_z are all fractal Brownian functions and the surface is a spatially isotropic fractal Brownian function, then $\rho \lambda N_x l_x$, $\rho \lambda N_y l_y$, *and* $\rho \lambda N_z l_z$ are also fractal Brownian. Clearly, the following intensity term

$$I = \rho \lambda (N \cdot L) = \rho \lambda (N_x L_x + N_y L_y + N_z L_z) \tag{201}$$

must be fractal Brownian also.

In a remotely sensed image, different land types are better characterized by spectral responses to different sets of bands than by overall average responses to all bands. Higher D values for a band implies higher within band variation (more spatially complex) and probably higher textural information. The coefficient of variation (standard deviation divided by mean) is a spatial statistic measure of data variability. The fractal dimension, on the other hand, is an index of spatial complexity (neighboring process). Besides the fractal dimension, three texture measures were also chosen as candidates for image information content evaluation. These texture measures are based on second-order statistics.

Second-order statistics

Estimates of the second-order probability distribution of a digital image source can be obtained by measurement of the second-order spatial histogram. Second-order histogram features are based on the joint probability distribution of pairs of pixels. Consider a pair of pixels $F(m,n)$ and $F(x,y)$ which are located at (m,n) and (x,y) and are separated by r radial units at an angle of θ. The joint distribution of spectral values is

$$P(a,b) = P_R\{F(m,n) = r_a \ , F(x,y) = r_b\} \tag{202}$$

Where r_a and r_b are pixel spectral values. The histogram estimate of the second-order distribution is equal to

$$P(a,b) \approx \frac{N(a,b)}{M} \tag{203}$$

Where $N(a,b)$ is the number of occurrences for which $F(m,n) = r_a$ and $F(x,y) = r_b$ and M is the total number of pixels in the measurement window. The second-order statistics used include

$$\text{(1) Angular second moment} = \sum_i \sum_j \left[\frac{P(i,j)}{r}\right]^2$$

$$\text{(2) Entropy} = -\sum_i \sum_j \frac{P(i,j)}{R} \log \frac{P(i,j)}{R} \tag{204}$$

$$\text{(3) Inverse second moment} = \sum_i \sum_j \frac{1}{1 + (i+j)^2} \frac{P(i,j)}{R}$$

Where $P(i,j)$ is the spatial co-occurrence matrix and R is the frequency normalization constant for selected orientation.

Sensor Response Dynamics

Image sensors often do not maintain proper spectral response due to non-uniform material properties. In the case of space-borne sensors, a common problem is the non-linearity in the sensor. Preprocessing corrections are usually required for multi-sensor multiscale data fusion. The commercial remotely sensed data are usually available in corrected forms unless special arrangement can be made. In most cases, the data subject to the correction processes are irreversible (e.g, TM geometric correction). The following critical corrections are keys to the scale study.

Non-linearity correction (TM,MSS)

Consider an imaging system which produces an observed image field $\Phi_o(x,y)$ according to the separable model

$$\Phi_o(x,y) = \mathcal{O}_Q\{\mathcal{O}_D\{C(x,y)\}\} \tag{205}$$

where

$$\begin{aligned} \mathcal{O}_Q\{\cdot\} &: \text{sensor point amplitude response} \\ \mathcal{O}_D\{\cdot\} &: \text{spatial, time, and wavelength response} \\ C(x,y,\lambda) &: \text{spectral energy distribution of input field} \end{aligned} \tag{206}$$

Sensor luminance correction can be accomplished by choosing a point restoration operator $\mathcal{O}_R\{\cdot\}$ such that

$$\mathcal{O}_R\{\mathcal{O}_Q\{\cdot\}\} = 1 \tag{207}$$

This correction can be performed using arithmetic operators or look-up tables in a digital image processing system. In a pre-launch calibration, a set of binary measurements Q are obtained and converted to a fixed point number L which is linearly proportional to the sensor input luminance. The following relationship is obtained and fitted to the data

$$\begin{aligned} \hat{L} &= g\{Q\} \\ \hat{Q} &= Q_{max}\frac{(g\{Q\} - L_{min})}{(L_{max} - L_{min})} \end{aligned} \tag{208}$$

The required luminance response can be obtained by rearranging the above equation as

$$\hat{L} = Q\left[\frac{\hat{L}_{max} - \hat{L}_{min}}{Q_{max}}\right] + \hat{L}_{min} \tag{209}$$

Sensor response correction (SPOT)

The spectral response of image sensors is determined by sensor materials (in case of SPOT, CCD arrays). The corrections for improper spectral response functions or cross-platform spectral data merging can be achieved by a straight forward procedure as described in the following paragraph. Consider the actual spectral response, L_a , and desired sensor spectral response, L_d , to a energy distribution function $P(\lambda)$ as

$$\begin{aligned} L_a &= \int P(\lambda)S(\lambda)d\lambda \\ L_d &= \int P(\lambda)T(\lambda)d\lambda \end{aligned} \tag{210}$$

Where $S(\lambda)$ is the sensor spectral response and $T(\lambda)$ is the desired spectral sensitivity. It is possible to find a functional transformation f such that the estimate of L_d is

$$\hat{L}_d = f\{L_a\} \tag{211}$$

The linear transformation as shown in the following equation can be used for its computational simplicity

$$\hat{L}_d = \alpha S(\lambda) + \beta \tag{212}$$

Where α and β are regression coefficients which minimize the selected error function.

Feature Signature Variabilities and Error Analysis

The variabilities (or uncertainties in our particular case) of a measure f can be approximated by

$$(\delta f)^2 = (\delta u)^2 \left(\frac{\delta f}{\delta u}\right)^2 + (\delta v)^2 \left(\frac{\delta f}{\delta v}\right)^2 + 2C^2_{uv} \left(\frac{\delta f}{\delta u}\right)\left(\frac{\delta f}{\delta v}\right) + \ldots\ldots \tag{213}$$

where δu is the uncertainty in variable u, and C^2_{uv} is the covariance between two variables u and v. The covariance can be expressed mathematically as

$$C_{uv}^2 = \lim_{n\to\infty} \frac{1}{n} \sum |(u_i - \bar{u}) (v_i - \bar{v})|, \qquad \bar{u} \text{ and } \bar{v} \text{ are mean values for } u \text{ and } v \tag{214}$$

The covariance in the above equation approaches zero when measured errors are not correlated with each other. The use of this generalized equation can best be illustrated using any derived vegetation indices as described in the previous section. The normalized difference vegetation index (NDVI) is of the indices used frequently by scientists and researchers. A simple derivation with general

equations applied to the NDVI is provided in the following paragraph. The analysis of other vegetation indices is much easier since most of the indices are linear combinations of different spectral bands.

Assume F denotes the normalized difference of two spectral bands, L_1 and L_2 or

$$F = \frac{L_1 - L_2}{L_1 + L_2} \tag{215}$$

The partial derivative of F with respect to any variable Ω can be expressed as

$$\frac{\partial F}{\partial \Omega} = \frac{2\left(L_2\frac{\partial L_1}{\partial \Omega} - L_1\frac{\partial L_2}{\partial \Omega}\right)}{(L_1 + L_2)^2} \tag{216}$$

The expected value and variance of F can be derived using Equation (213) as

$$\mathcal{E}[F] = \left(\frac{\mathcal{E}[\,L_1 - L_2\,]}{\mathcal{E}[\,L_1 + L_2\,]}\right) - \left(\frac{Var\,[\,L_1 + L_2\,]\,\mathcal{E}[\,L_1 - L_2\,]}{\mathcal{E}[\,L_1 + L_2]^3}\right) - \left(\frac{Cov\,[\,\{\,L_1 - L_2\},\,\{\,L_2\,\}\,]}{\mathcal{E}[\,L_1 + L_2\,]^2}\right) \tag{217}$$

$$Var\,[F] = \left(\frac{\mathcal{E}[\,L_1 - L_2\,]}{\mathcal{E}[\,L_1 + L_2\,]}\right)^2 \times \left\{\frac{Var\,[\,L_1 - L_2\,] - Var\,[\,L_1 + L_2]}{\mathcal{E}[\,L_1 - L_2\,]^2} - \frac{2\,Cov\,[\,\{\,L_1 - L_2\,\},\,\{\,L_1 + L_2\,\}\,]}{\mathcal{E}[\,L_1 - L_2\,]\,\mathcal{E}[\,L_1 + L_2]}\right\} \tag{218}$$

One of the most important variables in land-based remote sensing is the percent ground cover within an individual pixel. Considering the simple two dimensional projection of a given terrain (Figure 14), the total reflectance of a given pixel can be expressed as

$$L(\lambda,x) = \sum_i \phi_i(x) L_i(\lambda,x) \tag{219}$$

where

$\phi_k(x)$ - fraction of cover type k in pixel

$L_{i,k}$ - average reflectance of cover type k in spectral band i (220)

The above equation can be expanded with the associated constraint for vegetated ground as

$$L_i = \phi_c L_{i,c} + \phi_b L_{i,b} + \phi_{sb} L_{i,sb}$$
$$\textit{constraint} : \phi_c + \phi_b + \phi_{sb} = 1 \tag{221}$$

where c represents canopy, s represents soil background, and sb represents shadowed background. The sensitivity of F can be expressed as

$$\frac{\partial F}{\partial \phi_c} = \frac{2\left(L_2 \frac{\partial L_1}{\partial \phi_c} - L_1 \frac{\partial L_2}{\partial \phi_c}\right)}{(L_1 + L_2)^2} \tag{222}$$
$$\frac{\partial L_1}{\partial \phi_c} = L_{1,c} + L_{1,b} \frac{\partial \phi_b}{\partial \phi_c} + L_{1,sb} \frac{\partial \phi_{sb}}{\partial \phi_c}$$

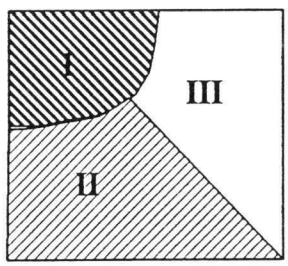

Figure 14. Components of total reflectance in a pixel

Much research has been conducted to investigate the relation between percent ground cover and associated shadow on the ground. A reasonable model which was adopted for the study is to assume the poisson distribution of the canopy structure. The relationship between the canopy and its shadow can be expressed as

$$\phi_b = (1 - \phi_c)^{\eta + 1}$$
$$\eta \text{ - } \textit{shadowed area cast by the plant/vertical canopy projection area} \tag{223}$$

Combine $\phi_c + \phi_b + \phi_{sb} = 1$ and $\phi_b = (1 - \phi_c)^{\eta + 1}$, the partial differentiation term can be

simplified as

$$\frac{\partial \phi_b}{\partial \phi_c} = -(\eta + 1)(1 - \phi_c)^{\eta}$$
$$\frac{\partial \phi_{sb}}{\partial \phi_c} = (\eta + 1)(1 - \phi_c)^{\eta} - 1 \qquad (224)$$

The sensitivity of L_1 with respect to ϕ_c becomes

$$\frac{\partial L_1}{\partial \phi_c} = L_{1,c} - (\eta+1)(1-\phi_c)^{\eta} L_{1,c} + ((\eta+1)(1-\phi_c)^{\eta}) L_{1,sb} \qquad (225)$$

Jasinski (1988) modeled the canopy as a block with height H and width D as shown in Figure 15(a). The η equals to $H \tan \theta_x / D$. The relationship can be used for a row crop as shown in Figure 15(b) with small modification.

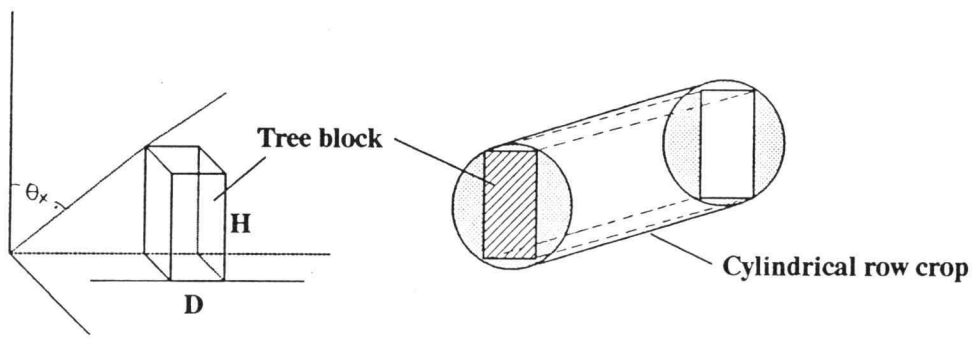

Figure 15. (a)Block representation of plant canopy, (b)Cylindrical representation of row crop

The canopy of the row crop can be mathematically described by

$$\frac{(x-nh)^2}{a^2} + \frac{y^2}{b^2} + \frac{(z-z_0)^2}{c^2} = 1 \qquad (226)$$

Where x , y , z are the coordinates of a given point on the surface of the canopy and a ,b ,c are the semi-axes. z_0 is the distance from the ground to the center of the cylinder and h is the row spacing.

The η for a simplified row crop canopy can be expressed as

$$\eta = \frac{H\tan\theta_x}{\sqrt{H^2 + D^2}} \tag{227}$$

In the case where no simple geometric equation is available to describe η, a numerical solution can be easily performed. The formulation of the error analysis has been generalized and should be applicable to model the feature variabilities with respect to parameters which might affect the overall spectral reflectance.

METHOD AND PROCEDURE

Remote Sensing Data Acquisition

The study covers the area from Boardman to Coldspring Reservoir (Figure 16). Image data from Landsat TM, MSS, SPOT HRV, SPOT Panchromatic, and Compact Airborne Spectrographic Imager (CASI) were assembled for the study area. The characteristics of each sensor was listed in Table 1. The data from Landsat was ordered directly from EROS data center (Sioux Fall, South Dakota) with satellite orbit correction only. Two scenes cover Path 44, Row 27 and Row 28 were required to cover the whole area. The special uncorrected scenes was acquired from SPOT Image Corporation under a special pilot project agreement with CROPIX inc. (Irrigon, OR).

Figure 16. Satellite overview of the study area with DLG vector overlay

Table 1 Characteristics of the sensors used in the study

SENSOR	SPECTRAL BANDS (um)	IFOV (m)	D. RANGE (bits)
MSS - 1	0.5 - 0.6	79x79	7
2	0.6 - 0.7	79x79	7
3	0.7 - 0.8	79x79	7
4	0.8 - 1.1	79x79	6
TM - 1	0.45 - 0.52	30x30	8
2	0.52 - 0.60	30x30	8
3	0.63 - 0.69	30x30	8
4	0.76 - 0.90	30x30	8
5	1.55 - 1.75	30x30	8
6	10.4 - 12.5	120x120	8
7	2.08 - 2.35	30x30	8
SPOT - 1	0.50 - 0.59	20x20	8
2	0.61 - 0.68	20x20	8
3	0.79 - 0.89	20x20	8
CASI - 1	0.4362 - 0.4782	5x5	12
2	0.5398 - 0.5504	5x5	12
3	0.5858 - 0.5964	5x5	12
4	0.6319 - 0.6444	5x5	12
5	0.6586 - 0.6729	5x5	12
6	0.6747 - 0.6872	5x5	12
7	0.7086 - 0.7140	5x5	12
8	0.7463 - 0.7589	5x5	12

The use of CASI image data was a completely different concept. The CASI system used in this research was still in its final commercial prototype from ITRES Research Limited (Calgary, Alberta, Canada). The sensor uses the reflection grating based pushbroom imaging spectrograph technology which covers the wavelength range from .43μm to .87μm. In any operation, the band width can be chosen as multiples of the 1.8 nm sampling interval. The CASI data were acquired in both multispectrometer mode and multispectral imaging mode. The multispectrometer was used in 39 equally spaced points across the full field of view. The sensor recorded the entire spectrum for each selected point in each frame. A moving average was applied to the full spectral curve (244 bands @ 1.8nm). Regression analysis was performed using spectral values and the ground feature of interest. A correlogram was produced with the correlation ranking between ground features and spectral bands.

The top eight ranking bands were used to reprogram the sensor for the multispectral imaging data acquisition. Originally, CASI was scheduled for high spatial resolution data acquisition since it can be mounted on a light aircraft. The instrument provides full resolution image of the scene under the aircraft for each specific band. The total number of bands chosen determines the maximum frame rate. Frame rate and ground speed determine along-track pixel spacing (Figure 17). Altitude determines cross-track pixel spacing (Figure 18). The CASI was mounted on a CESENA 172 aircraft floor with special approval from Federal Aviation Administration (FAA). A gyro was electronically connected to the data acquisition system for in-flight rolling, yawing, and crabbing conditions. Data were acquired from both 1700 meter (2 meter ground resolution) and 3300 meter (4 meter ground resolution). Difficulties occurred during the 1700 meter test flight due to the strong head wind condition and the unexpected long integration time required for minimum aircraft stabilization speed. Images acquired under this condition were fragmented and blurred even after intensive geometric and radiometric corrections. Very few linear features in the scene were acceptable for texture analysis. To make things worse, the target area for final flight had to be altered as aircraft restriction was requested by the Boardman Navy Bombing Range. The high rental cost for the aircraft and CASI instrument package prohibited another flight from being taken.

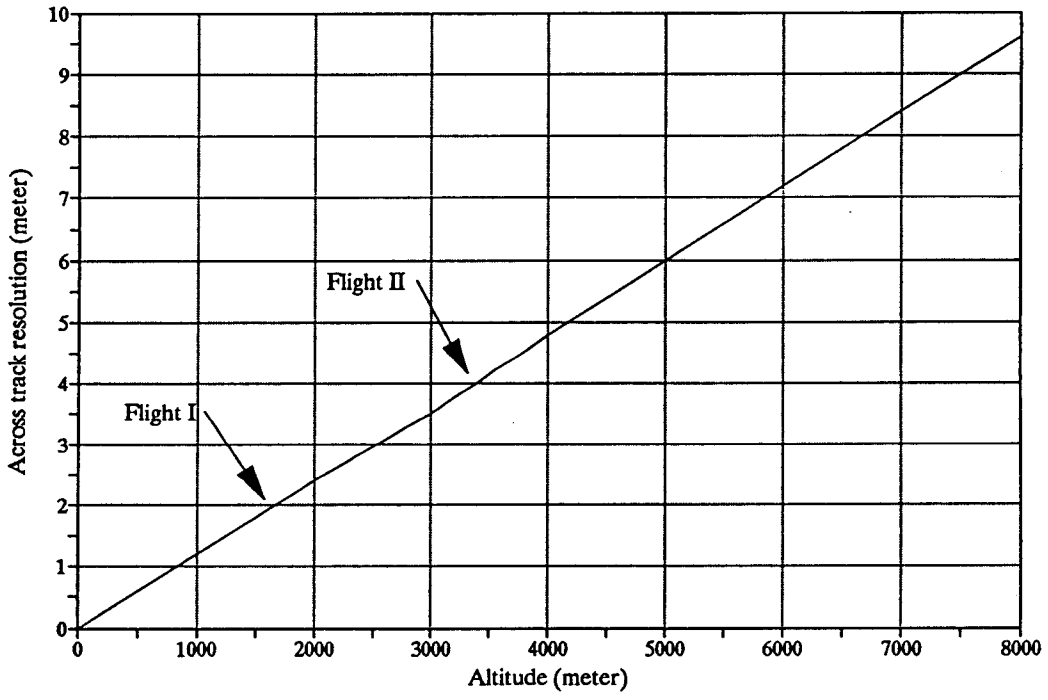

Figure 17. CASI across track ground resolution vs altitude

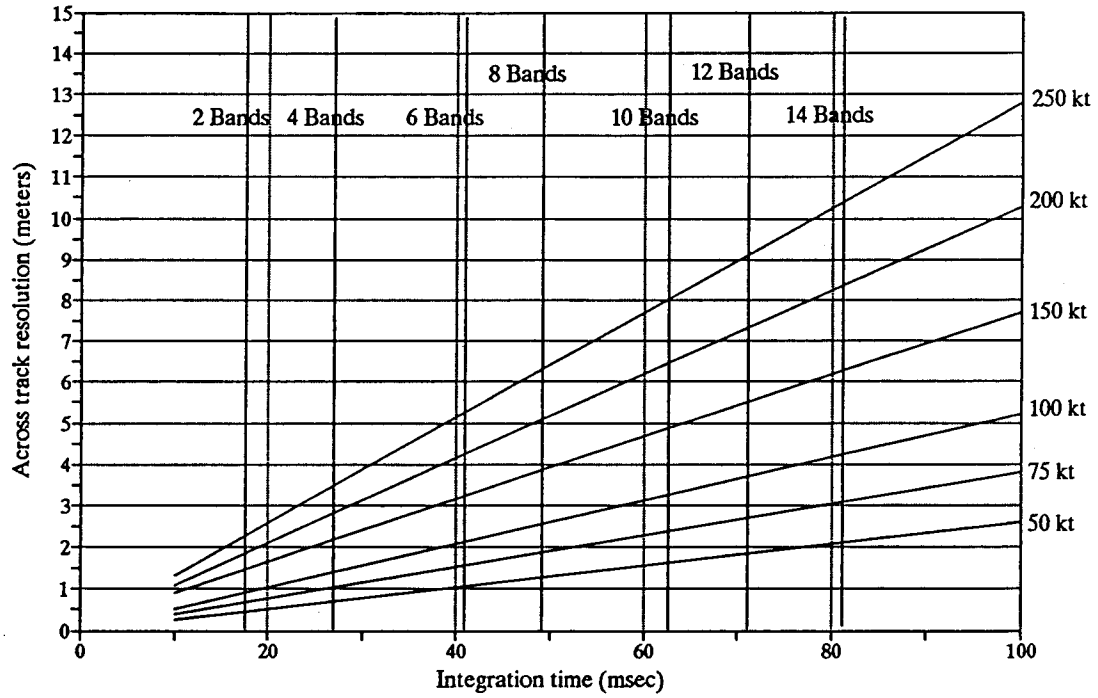

Figure 18. CASI ground resolution vs integration time for various air speeds (in knots)

Ground Spectral Data Collection

Hyperspectral data were obtained using a Spectron Engineering SE590 spectroradiometer. The instrument has 250 spectral bands spread over 0.4 μm - 1.1 μm (Figure 19) with a nominal bandwidth of 2.6 nm. More than 3200 data sets were taken both in the field and in the laboratory. A family of spectral curves cover crops from potato, alfalfa, corn, peas, onion, orchards and other dominant land features in the area of interest were taken in the commercial agricultural fields of the Columbia Basin. Since incident solar light intensity is variable, the spectral reflectance was calculated using a reference panel (Spectrolon). The SE590 was attached to the end of a truck mounted boom at a maximum height of 9.1 meters above the soil surface. Ground cover was taken simultaneous using photography and a grid rack. The measurements were generally taken between 10 AM to 2 PM Pacific Daylight Savings Time. The percent ground cover was calculated using a box counting technique. Leaf area index (LAI) was obtained using destructive sampling. A calibration data set was taken in a dark room equipped with Tungsten lamps (3200 K). Measurements were made using layers of leaves which covered different types of soil under different moisture conditions and slopes. Statistical analysis was conducted to obtain the relationships between several vegetation indices and spectral reflectance. Detailed analysis was reported in Chen and Lamb (1991) and Axness and Chen (1991).

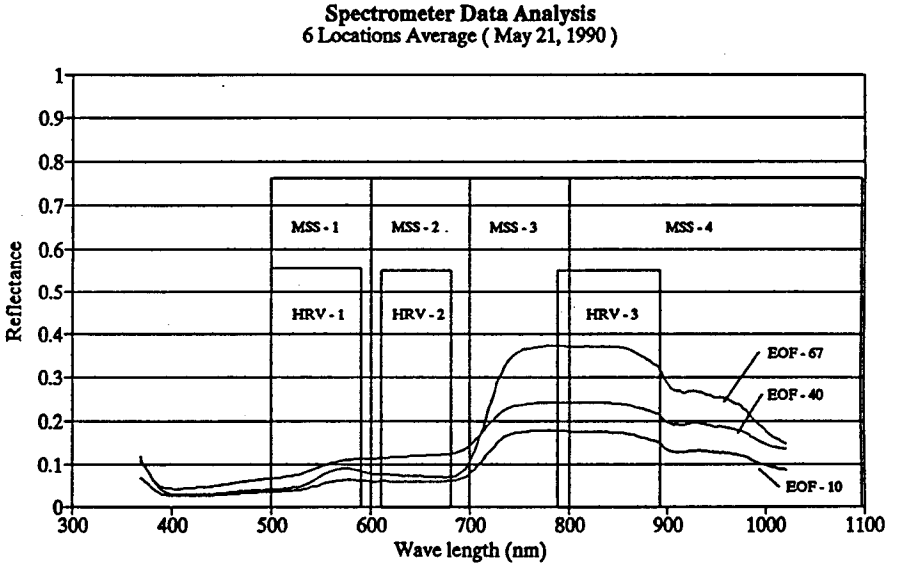

Figure 19. SE590 spectral reflectance curves and equivalent MSS and SPOT bands

Radiometric and Geometric Corrections

Calibration and conversion were required to remove the possible errors inherited from preprocessing procedures. An effective method which can be used to accomplish this requirement is to convert digital numbers from the Computer compatible tape (CCT) to scientific units such as radiance. Different corrections were applied to Landsat, SPOT, and CASI data since these sensors have different characteristics and the data sets available to the end-user were processed differently.

Landsat MSS and TM

The absolute radiometric calibration between bands on the Landsat satellite sensor is maintained by using internal calibrators which are physically located between the telescope and the detectors and are sampled at the end of a scan. The radiometric calibration for TM and MSS scanners can be accomplished by rescaling the raw satellite digital data to calibrated data (Clark, 1986). Theoretically, the raw digital data and calibrated data have a same dynamic range for any scene that is processed on the ground during a specific period of time. Conversion from a quantized and calibrated value (QCAL) on CCT-P tape to spectral radiance, L_λ, was performed using the following equation

$$L_\lambda = LMIN_\lambda + \left(\frac{LMAX_\lambda - LMIN_\lambda}{QCAL_{max}} \right) QCAL \tag{228}$$

where

$$\begin{aligned} QCAL &= \textit{Calibrated and quantized scale radiance , DN} \\ LMIN_\lambda &= \textit{Spectral radiance at } QCAL = 0 \\ LMAX_\lambda &= \textit{Spectral radiance at } QCAL = QCAL_{max} \\ QCAL_{max} &= \textit{Range of rescaled radiance , DN} \\ L_\lambda &= \textit{Spectral radiance , } mW \cdot cm^{-2} \cdot ster^{-1} \cdot \mu m^{-1} \end{aligned} \tag{229}$$

The parameters used in the calibration equation have been changed many times since the launch of both Landsat-4 and 5. The parameters used for spectral data calibration were listed in Table 2. Further between-scene processing was conducted since the images used for study area were not obtained from the same acquisition date. For the clear Landsat scene, a reduction in between-scene variability was achieved through a normalization procedure which converted the spectral radiance to effective at-satellite reflectance (or in-band planetary albedo). The effective at-satellite planetary reflectance is given by

$$\rho_p = \frac{\pi \cdot L_\lambda \cdot d^2}{ESUN_\lambda \cdot \cos \theta_s} \tag{230}$$

where

ρ_p = *Effective at satellite planetary reflectance , dimensionless*

L_λ = *Spectral radiance at sensor aperture , $mW \cdot cm^{-2} \cdot ster^{-1} \cdot \mu m^{-1}$*

d = *Earth-sun distance , astronomical units* (231)

$ESUN_\lambda$ = *Mean solar exoatmospheric irradiances , $mW \cdot cm^{-2} \cdot \mu m^{-1}$*

θ_s = *Solar zenith angle , degrees*

The mean solar exoatmospheric irradiances used for calibration was listed in Table 3. A precise accuracy assessment of such a calibration is very difficult due to the possible MSS sensor dependent changes in sensor optics with time and temperature-dependent changes and continuous in orbit gain changes of the TM internal calibrator. It seems a reasonable assumption that the error in the absolute radiometric calibration constant is less than 10% and uncertainties for exoatmospheric reflectance are less than 2% in visible/near infrared and less than 5% in short-wave infrared. Integrated in-band radiance, L, is further calculated for each pixel to verify the accuracy assumption. The integrated in-band radiance can be calculated by

$$L = BW \cdot L_\lambda \tag{232}$$

where

L = *in-band radiance for any pixel in a specific band , $mW \cdot cm^{-2} \cdot ster^{-1} \cdot \mu m^{-1}$*

BW = *Band-width or the difference between the upper and lower band edges of the band-pas*

L_λ = *Spectral radiance for the pixel in that specific band , $mW \cdot cm^{-2} \cdot ster^{-1}$*

(233)

To simplify the calculation, the nominal band width, BW_n shown in Table 2 was used. An additional calibration step was used for data acquired by the TM sensor to account for changes in post-calibration dynamic range. The minimum in-band radiance at $QCAL = 0$ (DN) and the maximum at $QCAL = 255$ (DN) for any specific band are given by

$$LMIN_f = BW_f \cdot LMIN_\lambda \tag{234}$$

where

$LMIN_f$ = *Minimum in-band radiance at QCAL = 0 DN using full-width at half maximum*

BW_f = *Observed spectral band-width as full-width at half maximum* (235)

$LMIN_\lambda$ = *Minimum Spectral radiance at QCAL = 0 DN*

and

$$LMAX_f = BW_f \cdot LMAX_\lambda \tag{236}$$

where

$LMAX_f$ = *Maximum in-band radiance at QCAL = 255 DN using full-width at half maximum*

BW_f = *Observed spectral band-width as full-width at half maximum*

$LMAX_\lambda$ = *Maximum Spectral radiance at QCAL = 255 DN*

(237)

Table 2 Spectral radiance for post calibration dynamic range

Band #	LMIN	LMAX
MSS-1	0.3	26.8
MSS-2	0.3	17.9
MSS-3	0.5	14.8
MSS-4	0.3	12.3
TM-1	-0.15	15.21
TM-2	-0.28	29.68
TM-3	-0.12	20.43
TM-4	-0.15	20.62
TM-5	-0.037	2.719
TM-6	0.1238	1.56
TM-7	-0.015	1.438

Table 3 Mean solar exoatmospheric spectral irradiance

Band #	Mean	Std. Dev.
MSS-1	184.9	0.2
MSS-2	158	0.3
MSS-3	126.9	0.1
MSS-4	89.4	0.7
TM-1	195.7	-
TM-2	182.9	-
TM-3	155.7	-
TM-4	104.7	-
TM-5	21.93	-
TM-7	7.452	-

SPOT HRV and panchromatic data

Calibration of SPOT images were made on SPOT standard product level 1B and level 2A. The correction applied to the level 1B image included both CCD detector normalization (radiometric correction), along-line, along column resampling, and unidirectional corrections (all three are geometric corrections). The correction used for the level 2A image included all the procedures for level 1B except the use of bidimensional geometric correction. Discussion on SPOT data correction is limited due to restriction of proprietary information. The concept of **Equivalent Radiance** was introduced by utilizing the following equation

$$L(k) = \frac{\int P(\lambda) S_k(\lambda) d\lambda}{\int S_k(\lambda) d\lambda}$$

where

λ = *wavelength* , μm

$P(\lambda)$ = *Spectral radiance density of homogeneous target* , $W \cdot m^{-2} \cdot srad \cdot \mu m$

$S_k(\lambda)$ = *Spectral response of HRV instrument in band k* , % (*FigureYYY*)

$L(k)$ = *SPOT equivalent radiance in the spectral band k*

The equivalent radiance calculated in the above equation represents a mean spectral radiance in a specific spectral band. It can also be interpreted as the spectral radiance of a landscape with uniform

spectral distribution in terms of wavelength. The equation can be further simplified by grouping some of the known sensor characteristics (such as spectral response function, Figure 20) as

$$L(k) = \frac{B(k)}{C_k} \tag{240}$$

where L(k) is the equivalent radiance, B(k) is the pixel brightness, and C_k the absolute calibration coefficient (the denominator in the equivalent radiance integral function). In the case when a non-standard gain is used for a specific sensor, the C_k was recalculated. By using this approach, the difference in sensitivity of 2 instruments can be compensated.

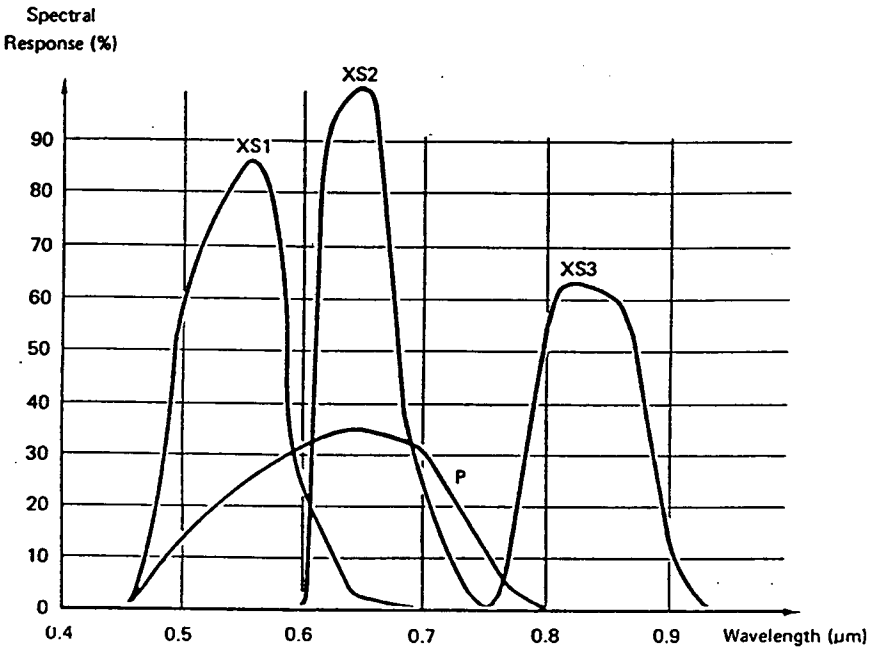

Figure 20. SPOT HRV and panchromatic spectral response function

Compact Airborne Spectrographic Imager (CASI)

The spectrum is integrated and sampled by internal CCD sensors in 1.8 nm blocks with an inherent average spectral resolution of 1.2 nm. The undersample of the spectrum results in a nominal overall average 3.0 nm resolution. The overall calibration and correction for the CASI sensor is presented as the schematic diagram in Figure 21.

IMAGING MODE DATA COLLECTION:
Bands of adjacent 1.8 nm wide spectral lines are summed, effectively providing programmable width/programmable centre spectral filters (bands) for each of up to 578 scene points.

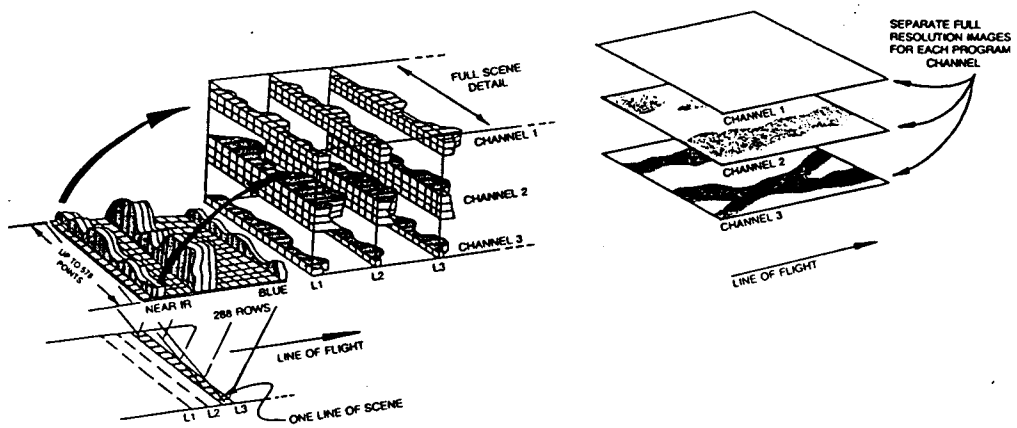

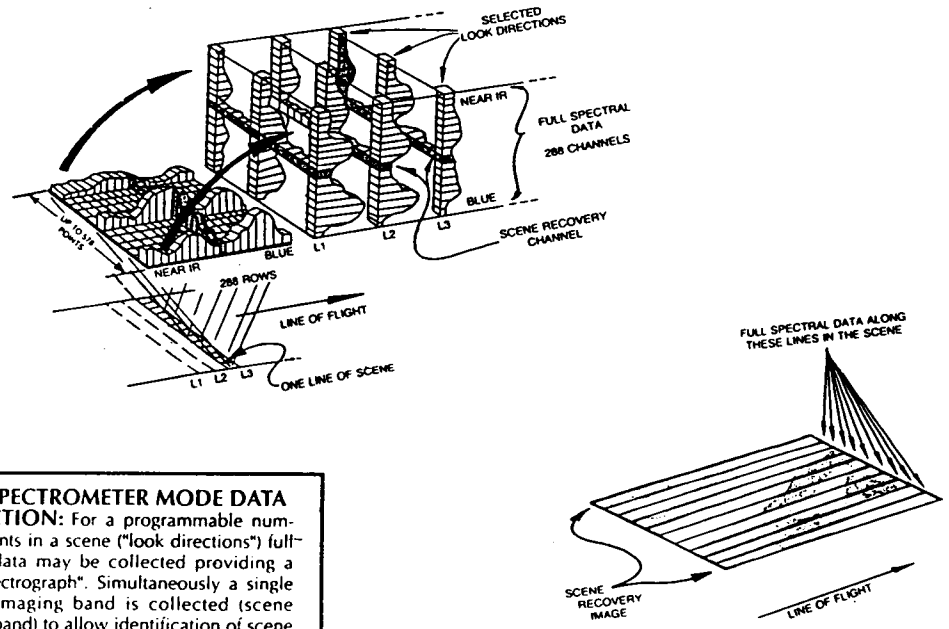

MULTISPECTROMETER MODE DATA COLLECTION: For a programmable number of points in a scene ("look directions") full-spectral data may be collected providing a "Rake Spectrograph". Simultaneously a single spectral imaging band is collected (scene recovery band) to allow identification of scene features in relation to spectral data points.

Figure 21. CASI sensor calibration, correction, and operation diagram

Spatial Scale Resampling

Spatial resampling was required to obtain different scales for each sensor. The digital resampling is essentially an optical magnification process different degrees of constraint. Almost all digital magnification techniques are based on surface interpolation. For natural resource applications such a technique seems to be appropriate since spectral reflectance is generally a surface optical representation of a given feature. To reconstruct an exact image, the original image must be spatially sampled at an interval of at least twice its highest spatial frequency and the reconstructive filter must be designed to pass the spectral component at control points without distortion. To avoid procedure with high computational cost, a set of imperfect reconstruction functions were used. Two steps are required for spatial resampling. The first step is the address transformation between input and output image since input and output images do not have the same size. Both forward or reverse address methods can be used to determine the input or output addresses for each spatial transformation. The forward address method was used for its programming simplicity. A compound geometric operator which includes generalized linear translation, scaling, and rotation transformation was used. The use of this operator ensures the address mapping is separable such that horizontal output address depends only upon the horizontal input and vertical address depends only upon the vertical input. The separable characteristics can be extended to provide nonlinear spatial warping (or rubber sheet stretching). Once the address mapping is completed, the spectral value at each pixel is then calculated. The interpolation of pixel brightness is necessary since there is no one to one relation between input and output image. Five interpolation algorithms were applied to each pixel in the area of interest. The algorithms used for the study include (1) Nearest neighbor, (2) Cubic convolution interpolation, (3) B-spline interpolation, (4) Parametric Bezier, and (5) Bilinear. The mathematical description of each algorithm can be found in Pratt (1991) and is summarized in the following paragraph. The computational stencils for some of the algorithms are shown in Figure 22.

Nearest Neighbor : every pixel in the new image is assigned the brightness value of the pixel in the original image that is nearest to it.

Bilinear interpolation : three linear interpolations were applied over the four pixels that surround the point found in the image corresponding to a given display grid coordinates.

Cubic convolution interpolation : force the slope of the ends of interpolation to be zero to eliminate the problem with slope discontinuity. The parametric expression of cubic convolution interpolation can be formulated as

$$\begin{aligned} f(x) &= (a+2)|x|^3 - (a+3)|x|^2 + 1, \quad 0 \le |x| \le 1 \\ & a|x|^3 - 5a|x|^2 + 8a|x| - 4a, \quad 1 \le |x| \le 2 \end{aligned} \tag{241}$$

B-spline interpolation : This method was used to provide the edge continuity and smoothness at the sample point. The B-spline is defined mathematically as

$$R_3(x) = \frac{2}{3} + \frac{1}{2}|x|^3 - (x)^2, \qquad 0 \le |x| \le 1$$
$$= -\frac{1}{6}(2 - |x|)^3, \qquad 1 \le |x| \le 2 \tag{242}$$

Alternate mathematical form was used for computer implementation of this algorithm

$$R_3(x) = \frac{1}{6}[(x+2)_+^3 - 4(x+1)_+^3 + 6(x)_+^3 - 4(x-1)_+^3]$$
$$\Rightarrow \tag{243}$$
$$(z)_+^m = z^m \quad z>0$$
$$= 0 \quad z \le 0$$

Parametric Bezier : A simple Bezier interpolation technique was used for brightness curve approximation.

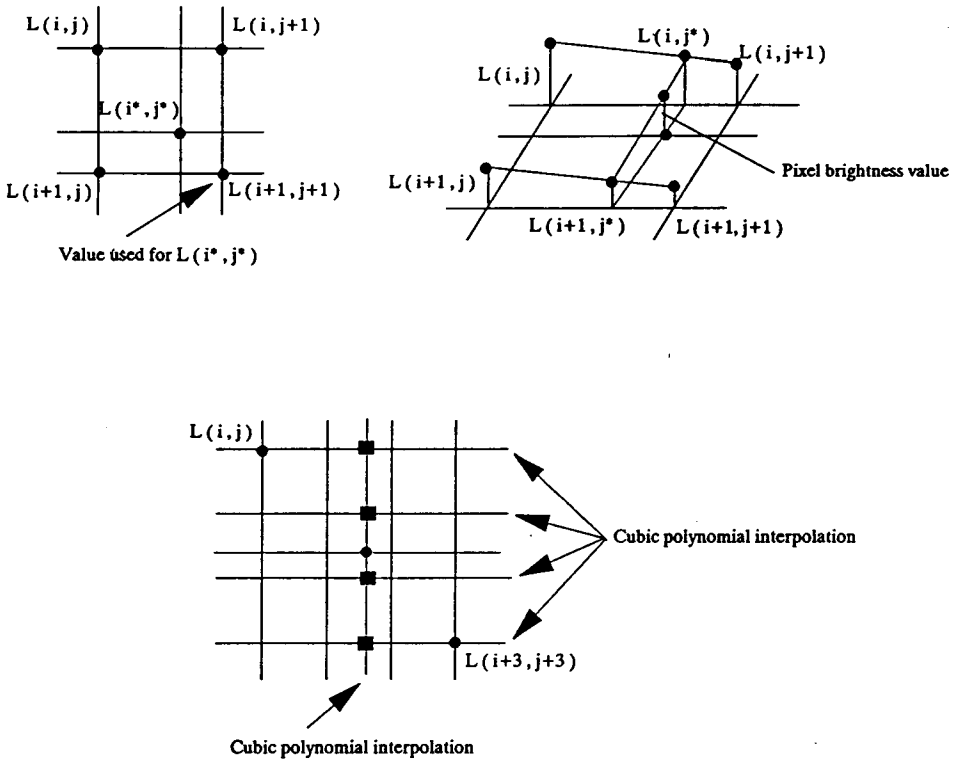

Figure 22. Computation stencils for spatial resampling

Data Analysis

The flow chart for data analysis procedures is shown in Figure 23. The raw images from each sensor were obtained from appropriate sources. The geometric and radiometric correction/restoration were performed as necessary. The information content such as entropy measure and fractal dimension of the power spectrum were calculated. Multispectral transformations were applied to the corrected image. Information contents were again calculated for the transformed images. A set of fourier transforms based on the ring region feature masking were applied to each image. Assume (ω_x, ω_y) are the image spatial frequencies. An optical sensor produces an image output as

$$M(\omega_x,\omega_y) = |\mathcal{F}(\omega_x,\omega_y)|^2 \tag{244}$$

Angular integration of $M(\omega_x, \omega_y)$ over the spatial frequency plane produce a spatial frequency feature that is invariant to translation and rotation. This feature is defined in the polar form as

$$\begin{aligned} N(\rho) &= \int_0^{2\pi} M(\rho,\theta)d\theta \\ \theta &= \tan^{-1}(\omega_y/\omega_x) \\ \rho^2 &= \omega_x^2 + \omega_y^2 \end{aligned} \tag{245}$$

The region of the ring becomes

$$S_{ring} = \int_{\rho(m)}^{\rho(m+1)} \int_0^{2\pi} M(\rho,\theta)\, d\rho\, d\theta \tag{246}$$

The Fourier transformed image served as the input to the Radon transform process. The spatial resampling algorithms were applied to the output image from the Radon transform to obtain the spatial resolutions range from 10, 20, 30, 40, 50, 60 meters. The statistical feature extraction procedures were performed and measures were calculated. Besides the statistical measures discussed in the theory section, the co-occurrence matrix for a subset of each image was constructed. The co-occurrence matrix was constructed according to the following mathematical formulation. Assume $f(x,y)$ is an image with dimension of NxM and G is the number of grey levels of the image (on a non sliced 8 bit system G equals 256). Assign D as a set of displacement vectors

$$D = \{d \mid = (dx,dy), 0 \le dx < N, -M \le dy < M\} \tag{247}$$

Define M_d a matrix whose $(i,j)^{th}$ element is the number of times any grey level i and j occur in the relative location d. The term $M_d(i,j)$ is equal to

$$M_d(i,j) = \#[((x_1,y_1),(x_2,y_2)) : f(x,y_1) = i, f(x_2,y_2) = j \ , \ d = (a,b) \ , \ d \in D \rightarrow x_2 = x_1 + a \ , \ y_2 = y_1 + b \ ] \quad (248)$$

Where # represents the number of elements in the set.

Once the co-occurrence matrix was constructed, the statistical feature extraction and fractal dimension of the power spectrum were again calculated. The Fourier spectrum fractal dimensions of a 9x9 convolution window over the whole image were computed. Pentland (1984) proved that the spectral density of p(f) of a fractal Brownian function is proportional to $f^{-2(2-D)-1}$, where D is the fractal dimension. To obtain an estimate of D a simple regression was performed on p(f) and f. The parameter (2-D) was equated to the regression coefficient and D was calculated.

The co-occurrence matrix was used in combination with contrast and uniformity to extract texture information from the image. The contrast is defined in terms of M_d as

$$\theta = \sum_{ij} (i-j)^2 M_d (i,j) \quad (249)$$

The contrast of the co-occurrence is a measure of the texture coarseness since this value represents spread away from the main diagonal. A high value of contrast for small displacement indicates a fine texture while low values indicate a relative coarse texture. The uniformity (or angular second moment as defined in the theory section) is

$$\phi = \sum_{ij} M_d(i,j)^2 \quad (250)$$

This is a measure of homogeneity of the image. In a homogeneous image, such as a uniformly covered field, M_d has fewer entries of large values therefore produces a large ϕ . In a non-uniform field the M_d has large number of entries with small values and ϕ should be smaller.

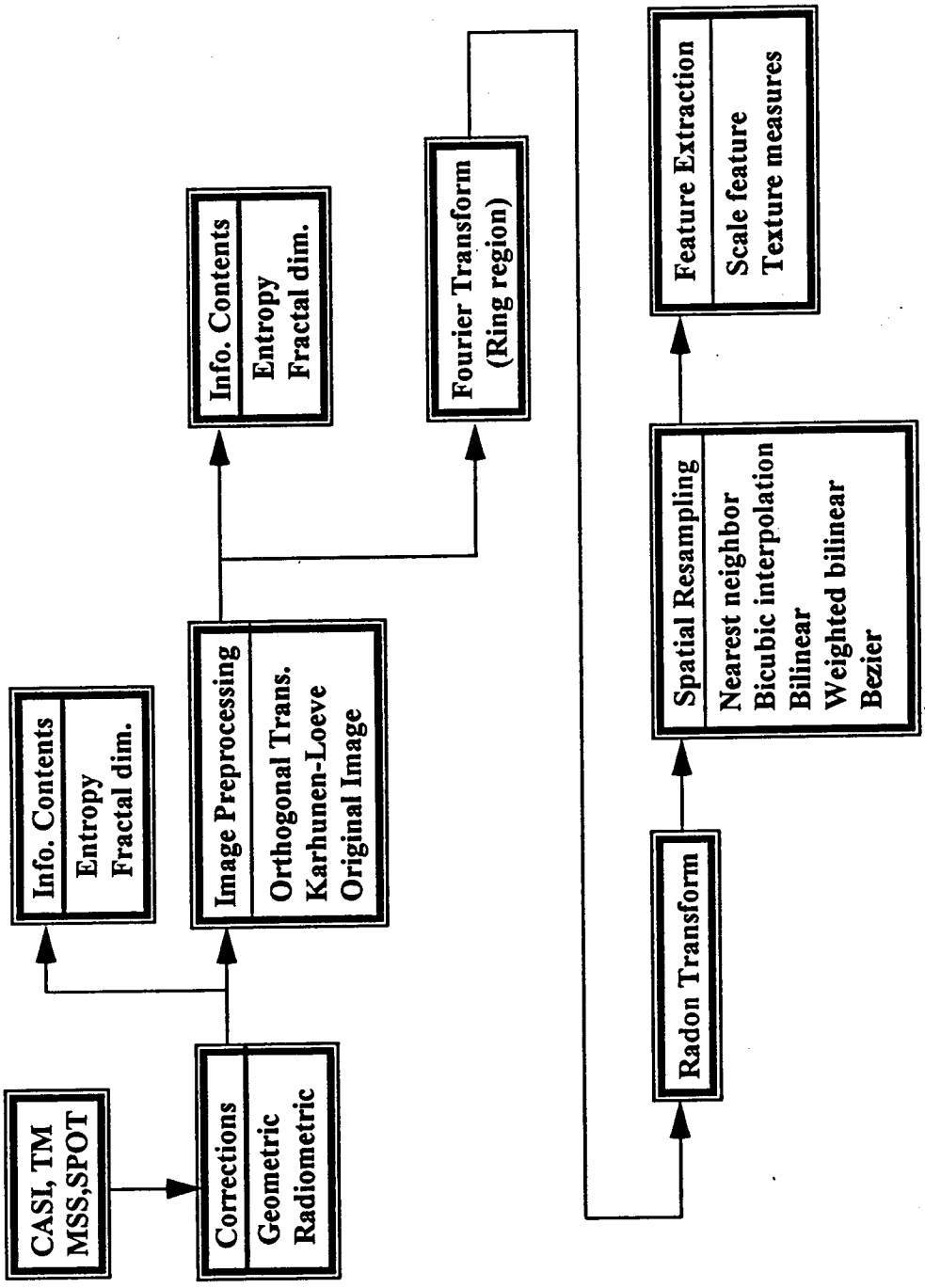

Figure 23. Data analysis flow chart

RESULTS AND DISCUSSION

Canopy Spectral Reflectance Model

The L-system based plant was first constructed using ray tracing technique on a super computer at the National Center for Super Computing Applications (NCSA, University of Illinois). The amount of CPU time required to construct a plant was about 30 minutes on an interruptible batch mode. A simplified ray tracing scheme was implemented to reduce the demand of high CPU time. The simplified ray tracing scheme took 40 seconds to generate a plant. The ray tracing procedure was used to simulate the spectral reflectance for the preset canopy geometry. The NDVI values calculated from the L-system plant model and block plant defined in the theory section are presented in Figure 24. The L-system plant produced higher NDVI values compared to SE590 measurements. The reason for the higher simulated NDVI values was due to the dark (wet) soil background presented in the SE590 field measurement plots. The relation between NDVI and GC for SE590 and the L-system is shown in Figure 25. The variation of the simulated NDVI increases with the increasing GC up to about 50% ground cover and then starts decreasing as the ground cover approaches full cover. The variation was partially due to the shadow term presented in the model while in the real sensor data the shadow effect was removed, at least to some extent by using the NDVI values. The NDVI values calculated from SE590 measurements for different ground resolutions are plotted in Figure 26 together with the NDVI calculated from SPOT images. The 2 meter resolution measurement has higher NDVI values than the 1 meter resolution measurement. This is probably due to the fact that at lower resolution (2 meter) with lower ground cover (GC) the sensor was sensing a higher percentage of the soil background and therefore produced higher NDVI values. The NDVI calculated from the SPOT images shows low NDVI values at low ground cover (0-50% GC). Satellite CCD sensors such as those on board SPOT have specific near infrared threshold values under which the sensor response is low. This is particularly true when the ground has very little vegetation. The low spectral in the near infrared region combined with the higher red reflectance produces some low NDVI values. The variabilities of NDVI calculated from various resolutions and simulated spectral values are presented in Figure 27. The simulated values consistently over estimate the variance of NDVI. It is clear that the over estimation of the variance is the result of shadow and background removal mechanisms embedded in the NDVI values calculated from the sensor data.

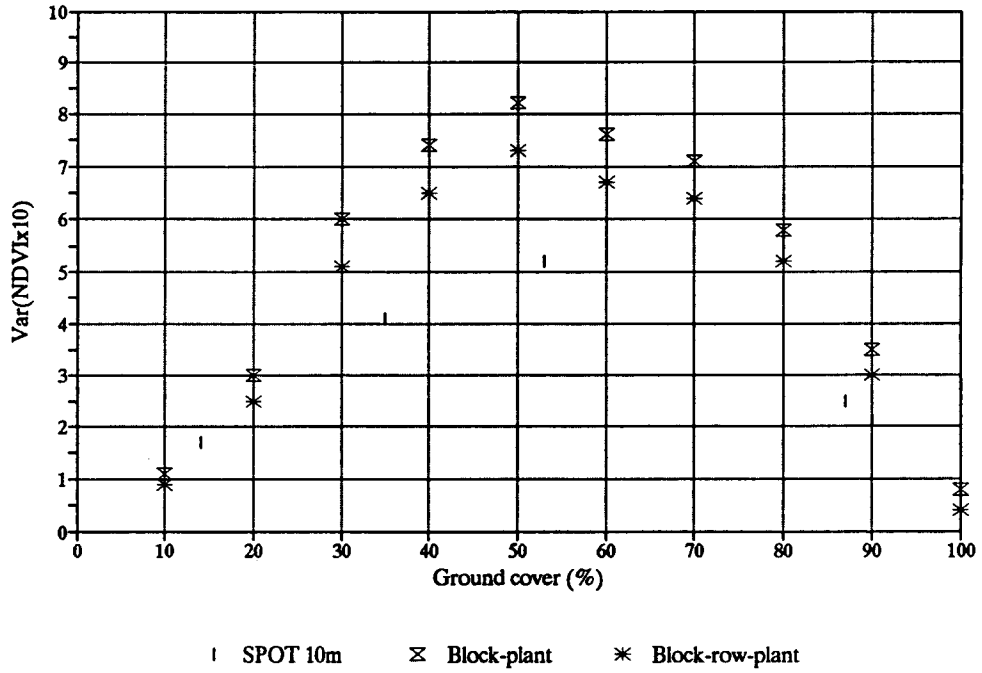

Figure 24. Comparison of NDVI calculated from 2 plant models and SPOT image

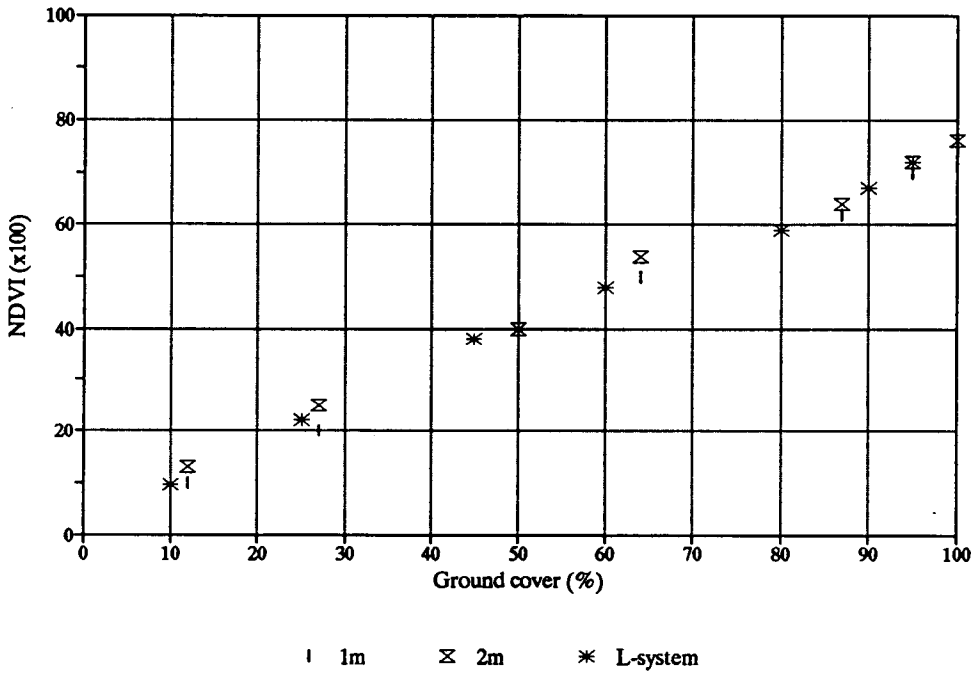

Figure 25. Comparison of NDVI calculated from SE590 and L-system

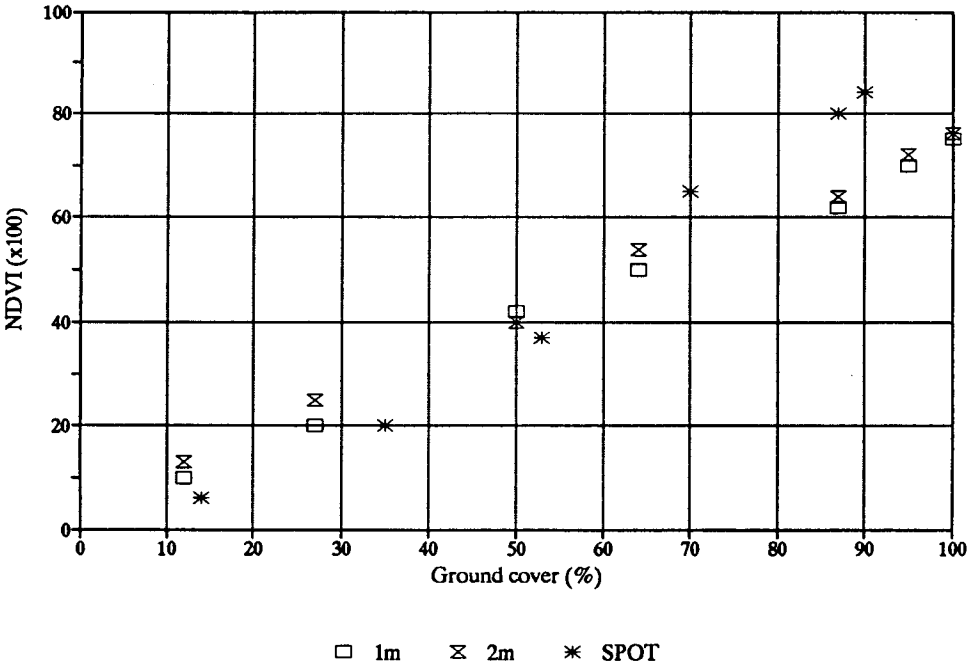

Figure 26. Comparison of NDVI calculated from SE590 and SPOT images

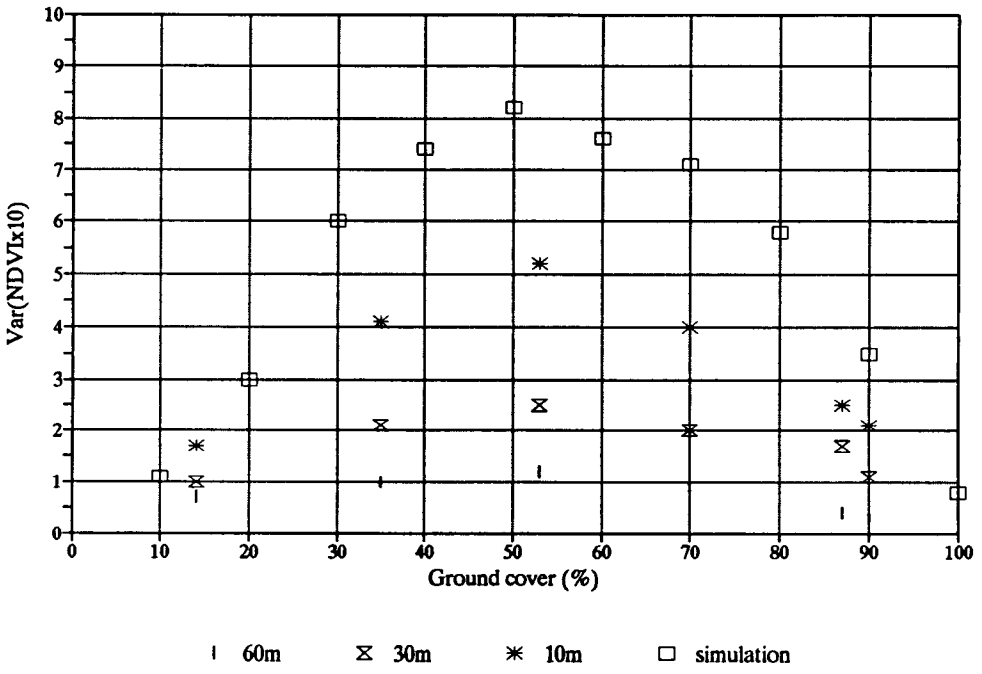

Figure 27. Spectral reflectance variance under different ground resolution (resampled SPOT image)

The results from the canopy model and SE590 ground spectral measurements showed consistent agreements with the known physical land processes encountered in remote sensing. The vegetation index does change somewhat with change in resolutions (scale). The average changes in spectral reflectance at different scales was not as significant as the variabilities in the spectral reflectance. These results suggest the spatial information (especially the texture measurement) could be used to extract more information from multiscale images.

Information Content and Feature Extraction

The information content calculated in terms of entropy and fractal dimension of the power spectrum are presented in Tables 4, 5, 6, 7 and Figures 28 and 29. The analysis were performed for a combination of raw spectral reflectance, different sensors, output from different transforms, and also for four different ground features. In case of information content, the TM shows 4.71 bits/pixel of entropy, MSS has 3.66 bit/pixel, and SPOT has 4.27 bits/pixel of entropy. It should be noted that the maximum possible entropy measure for TM is 8 bits, for MSS is 6 bits, and for SPOT is 8 bits. All the calculated values were lower than the theoretical limit due to the fact that saturation radiances for all three systems are set well above the levels of typical land surface reflectance. If all the physical and sensing conditions are set equal, the TM should have an equal entropy measure as SPOT, and 1 bit per channel more entropy than MSS. Table 4 shows TM carries 1.1 bit/channel more entropy than the MSS and about .5 bit/channel more than SPOT. The slightly lower number for SPOT is due to the low information content in the near infrared band (0.79-0.89 μm, which misses the red edge for vegetation). The Fourier transform did not increase information content for TM due to the homogeneous nature of the agricultural lands. The Radon transform, on the other hand, increased TM information content substantially. The main reason for such an increase is due to the spectral diversities of the TM sensor, which was enhanced by the Radon transform slicing characteristics. Both the Fourier and the Radon transform provide great improvements for MSS and SPOT information content. The SPOT image improved information content was the result of its high spatial resolution. Both Fourier and Radon transforms have shown a great potential to improve the overall image information content. On the individual feature basis, GVI, NDVI, and the 1st principal component show no significant differences. The Fourier and Radon transform do indicate a gain of more than 1 bit of information. The entropy measures also show increasing separability between each feature. This implies the possible use of the tranformed image as another spectral band for classification. The entropy values calculated from different resolutions (10, 30, 60 meters) indicate that the Fourier and Radon tranforms were able to maintain information content. The result is encouraging since it suggests this set of upscaling (or downscaling) procedures can be used to integrate local land process models to regional large scale models.

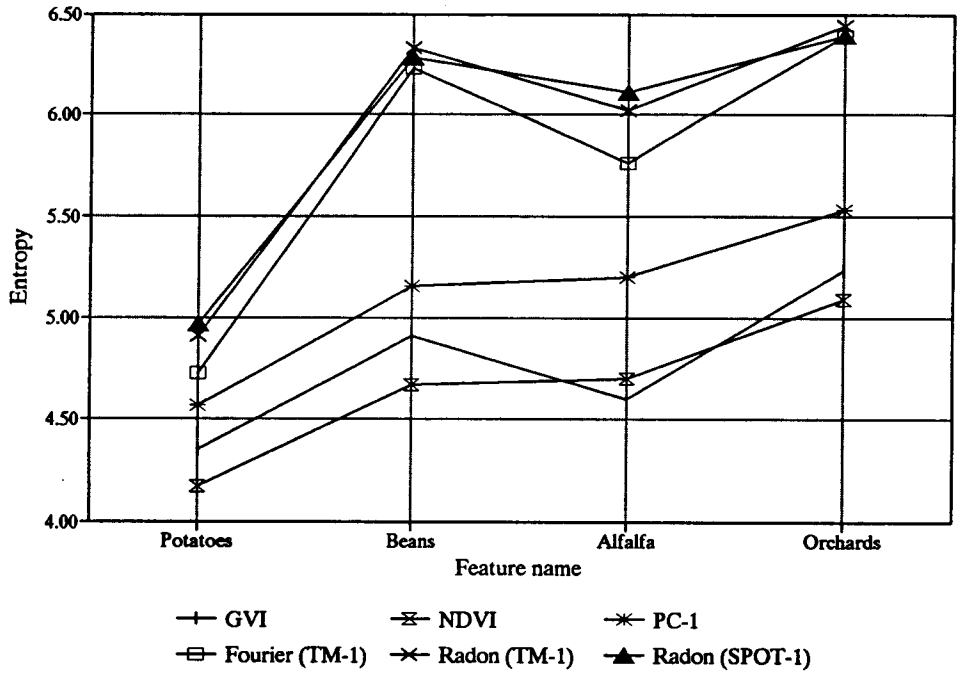

Figure 28. Individual feature entropy measure for different enhancement methods.

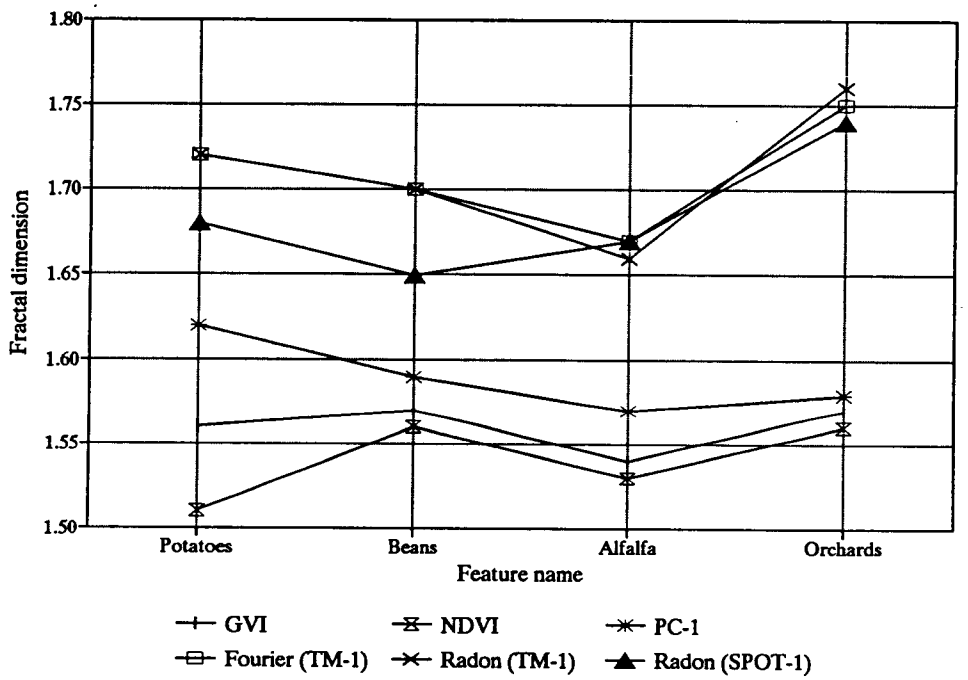

Figure 29. Individual feature fractal dimension for different enhancement methods.

Table 4 Entropy values for raw spectral reflectance and output from transforms

	Raw Image (full scene)			Fourier Transform			Radon Transform		
Band	TM	MSS	SPOT	TM	MSS	SPOT	TM	MSS	SPOT
1	4.00	3.17	3.92	5.33	4.95	5.92	5.39	5.25	5.13
2	3.98	3.21	4.66	4.75	5.10	5.40	5.24	5.11	5.29
3	4.65	4.45	4.22	4.90	4.65	4.95	5.78	5.97	5.97
4	5.20	3.79	-	4.70	4.71	-	6.30	5.23	-
5	5.30	-	-	-	-	-	-	-	-
6	-	-	-	-	-	-	-	-	-
7	5.10	-	-	-	-	-	-	-	-
Average	4.71	3.66	4.27	4.92	4.85	5.42	5.68	5.39	5.46

Table 5 Entropy values calculated from four different ground features.

	GVI	NDVI	Kahunen - Loeve			Fourier Tranform		Radon Transform	
Name	5.70	5.82	PC-1	PC-2	PC-3	TM-1	SPOT-2	TM-1	SPOT-2
Potatoes	4.35	4.17	4.57	4.51	3.13	4.73	4.87	4.91	4.97
Beans	4.91	4.67	5.16	5.74	3.91	6.23	6.05	6.33	6.28
Alfalfa	4.60	4.70	5.20	4.90	3.71	5.76	5.92	6.02	6.11
Orchards	5.23	5.09	5.53	5.40	3.58	6.39	6.42	6.44	6.39

Table 6 Fractal dimensions for raw spectral reflectance and output from transforms

	Raw Image (full scene)			Fourier Transform			Radon Transform		
Band	TM	MSS	SPOT	TM	MSS	SPOT	TM	MSS	SPOT
1	1.73	1.67	1.73	1.88	1.79	1.79	1.89	1.78	1.89
2	1.69	1.66	1.69	1.81	1.73	1.77	1.87	1.70	1.83
3	1.66	1.69	1.64	1.84	1.69	1.75	1.86	1.67	1.83
4	1.62	1.64	-	1.81	1.66	-	1.83	1.64	-
5	1.64	-	-	1.77	-	-	-	-	-
6	-	-	-	-	-	-	-	-	-
7	1.59	-	-	1.68	-	-	-	-	-
Average	1.66	1.67	1.69	1.80	1.72	1.77	1.86	1.70	1.85

Table 7 Fractal dimensions calculated from four different ground features.

	GVI	NDVI	Kahunen - Loeve			Fourier Tranform		Radon Transform	
Name	Avg=1.57	Avg=1.52	PC-1	PC-2	PC-3	TM-1	SPOT-2	TM-1	SPOT-2
Potatoes	1.56	1.51	1.62	1.52	1.42	1.72	1.69	1.72	1.68
Beans	1.57	1.56	1.59	1.51	1.41	1.70	1.66	1.70	1.65
Alfalfa	1.54	1.53	1.57	1.48	1.39	1.67	1.66	1.66	1.67
Orchards	1.57	1.56	1.58	1.44	1.36	1.75	1.72	1.76	1.74

Table 8 Kolmogorov-Smirnov test of spatial resampling algorithms

	Enlargement power			
Algorithm	2	4	6	8
Nearest neighbor	+	+	+	-
Bilinear	+	+	+	-
Cubic convolution	+	-	-	-
B-spline	+	+	-	-
Parametric Bezier	-	+	-	-
.+ : Accept @ 5% level, - : Reject @ 5%				

The fractal dimensions calculated from TM, MSS, and SPOT raw images show little differences between each sensor. Much higher fractal dimensions were found in the Fourier and Radon transformed images (Table 6). The fractal dimensions calculated from individual features were shown in Figure 29. The orchard fields which have a high spatial pattern in nature show a much higher fractal dimension than other features. This is a strong indication of the utility of fractal dimensions as a texture measure. In the cases of self-upscale (or downscale) raw images, most fractal dimensions decrease with the decreasing spatial resolution. The scale-dependent intermittency can be attributed to the statistical properties of the Earth's surface in a remotely sensed image which are not a result of any single dominant physical process. In the case of study area, the variable ground features coupled with geological depositions in the field produced a complicated background composition within the image. Theoretically, the quiescence scale-dependent intermittency suggests a fractal dimension smaller than 2 ($1 < D < 2$). As a consequence, the total region which shows active fluctuation in the larger scale will decrease as the scale of investigation decreases. The fractal dimension will reach unity as the fluctuation of a two dimensional region approaching a highly convoluted one dimensional curve. The fractal dimension plot for each individual feature presents a strong support for this explanation. In the case of the NDVI image (Figure 30), the fractal dimension drops sharply at the 20 meter resolution. This is due to the fact that the size of most features within the area have a value smaller than 200 meters and the 9x9 convolution window

basically covers an area of 180 meters by 180 meters. The GVI image has a much sharper drop in the 20 meter range (Figure 30) due to the much smaller size of green biomass presented in the scene. This provides an indirect support for GVI's capability to isolate soil effects from the composite spectral reflectance. The Radon and Fourier transformed images maintain the scale invariant properties reasonably well within the studied scale (Figure 30). The texture measures of individual features were calculated and are plotted in Figures 31 and 32. The orchard fields, which have a relative coarser texture show lower uniformity values throughout the 10 to 60 meter scale range. The contrast measure does not show a significant difference between each feature (Figure 31). This is a little bit of a surprise since orchards have a much coarser visual texture than other crops.

Many algorithms are available for spatial resampling such as those proposed in the early spatial scale resampling section. No standard measures were established to evaluate the quality of these algorithms since most statistical methods are scene dependent and site specific. The investigation of changes in information content is necessary to provide an unbiased measure of scaling processes. The criteria used to evaluate the spatial resampling should be a measure of image content that is invariant to scale transformations of the original image. Fractal dimensions seems to be good candidate for this evaluation. The power spectrum fractal dimensions were calculated using the method described in the Data Analysis section. The Kolmogorov-Smirnov (K-S) test was used to test whether the resampled images and original images were drawn from the same population distribution function. A Chi-square test would have been used if the fractal dimensions were binned data. To perform a K-S test, assume N events are located at values X_i , $i = 1, \ldots, N$ and $S_N(x)$ is the function given the fraction of data points to the left of a given value x on the cumulative distribution function. The K-S statistics for 2 cumulative distribution functions $S_{N1}(x)$ and $S_{N2}(x)$ is equal to

$$D = \max_{-\infty < x < \infty} |S_{N_1}(x) - S_{N_2}(x)| \tag{251}$$

The function to calculate the significance of a confidence level λ can be written as

$$Q_{KS}(\lambda) = 2\sum_{j=1}^{\infty} (-)^{j-1} e^{-2j^2\lambda^2} \tag{252}$$

The significance level of an observed value of D is given by

$$P(D>observed) = Q_{KS}\left(\sqrt{\frac{N_1 N_2}{N_1 + N_2}}\, D\right) \tag{253}$$

The test results for different resampling algorithms is listed in Table 8. The nearest neighbor

algorithm shows the best scale invariant nature among all the algorithms tested (Figures 33, 34, 35, 36, 37, and 38). Slightly different results were obtained by Lalitha et al. (1989).

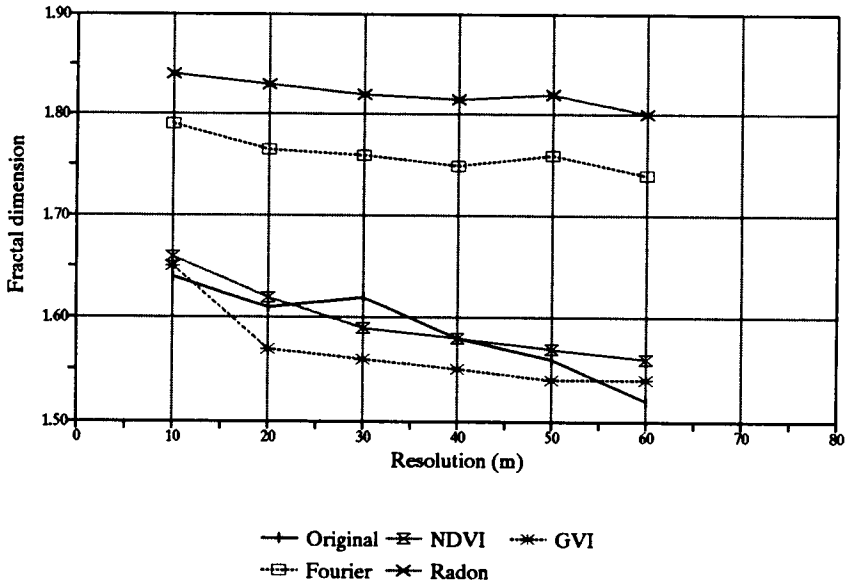

Figure 30. Scale invariant properties of different processes

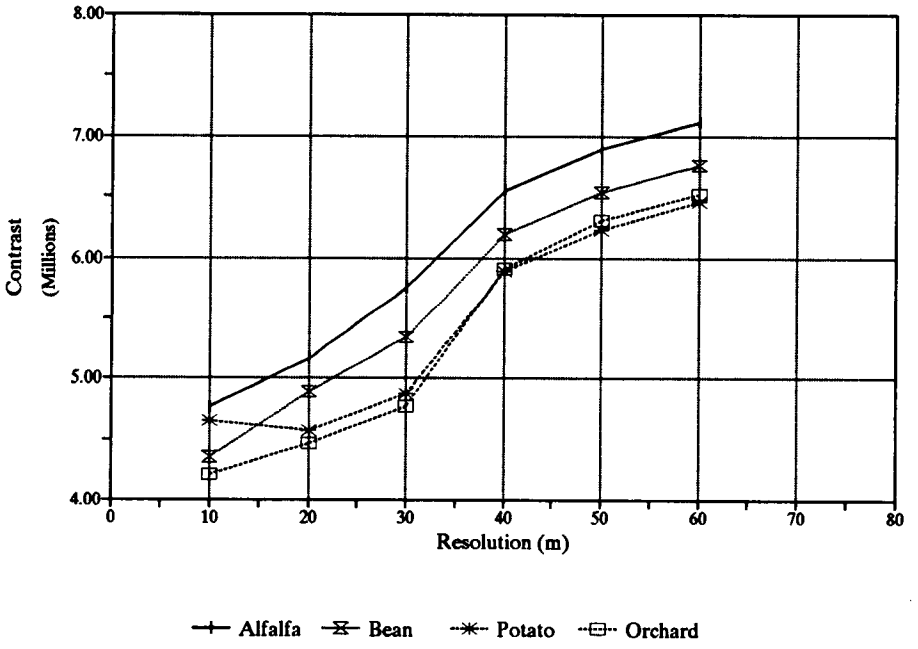

Figure 31. Contrast calculated from co-occurrence matrix

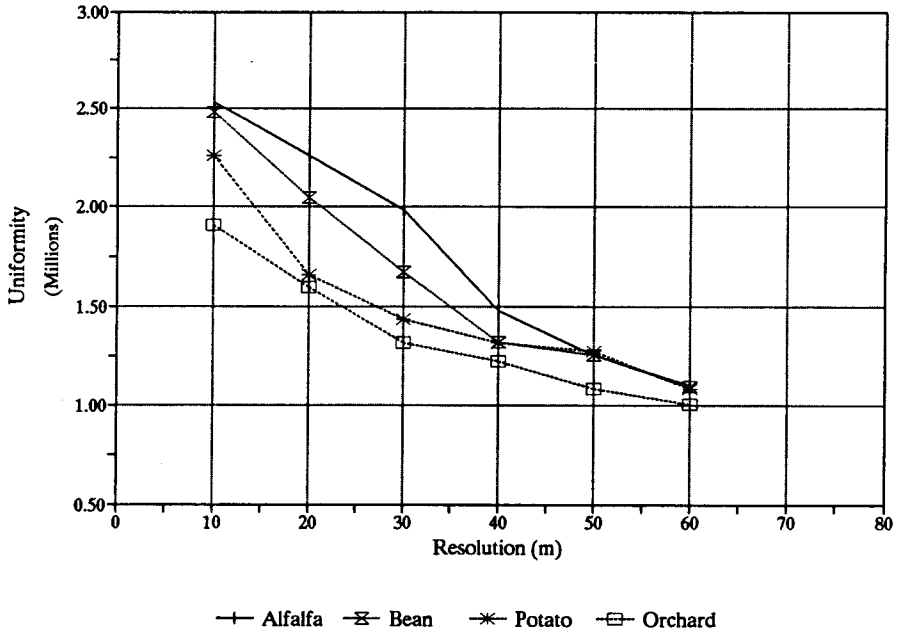

Figure 32. Uniformity calculated from co-occurrence matrix

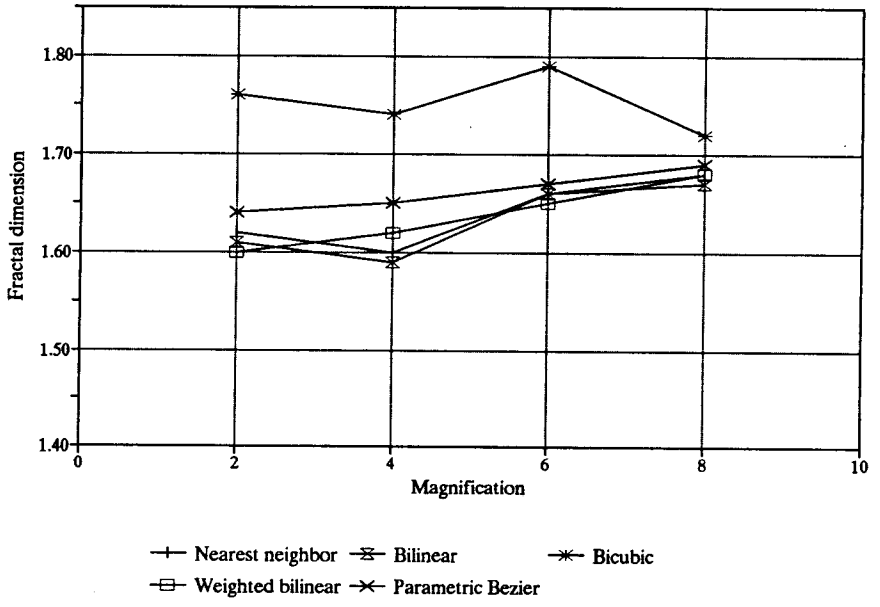

Figure 33. Mean fractal dimension of different spatial resampling algorithms

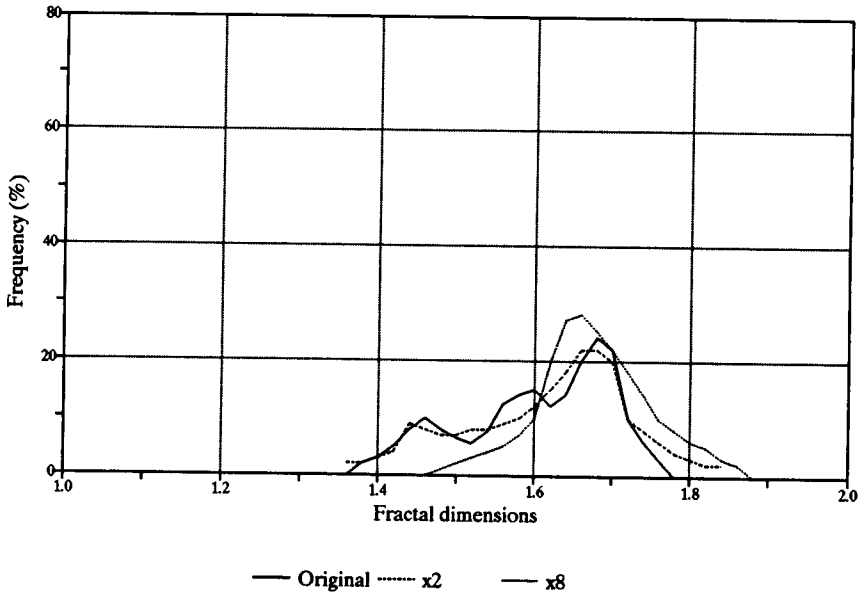

Figure 34. Fractal dimension frequency distribution of nearest neighbor algorithm

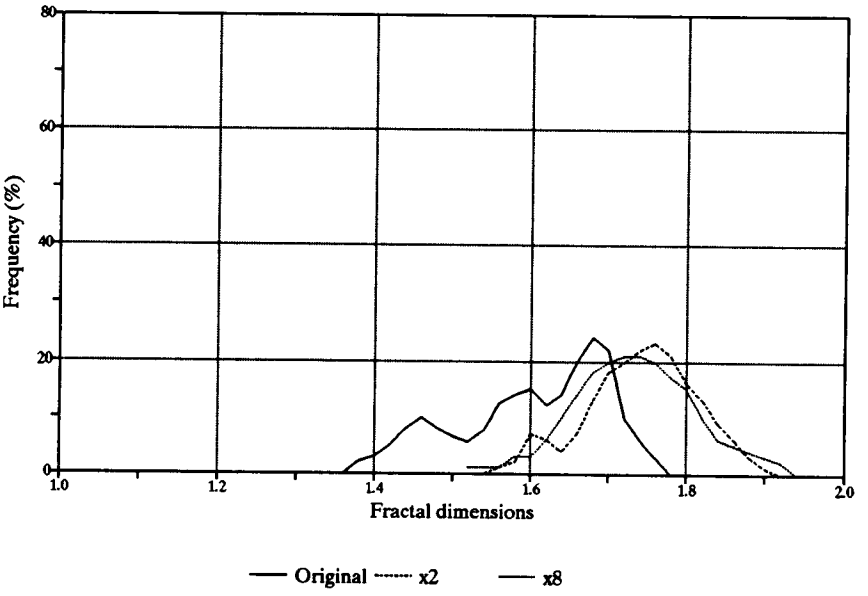

Figure 35. Fractal dimension frequency distribution of bilinear algorithm

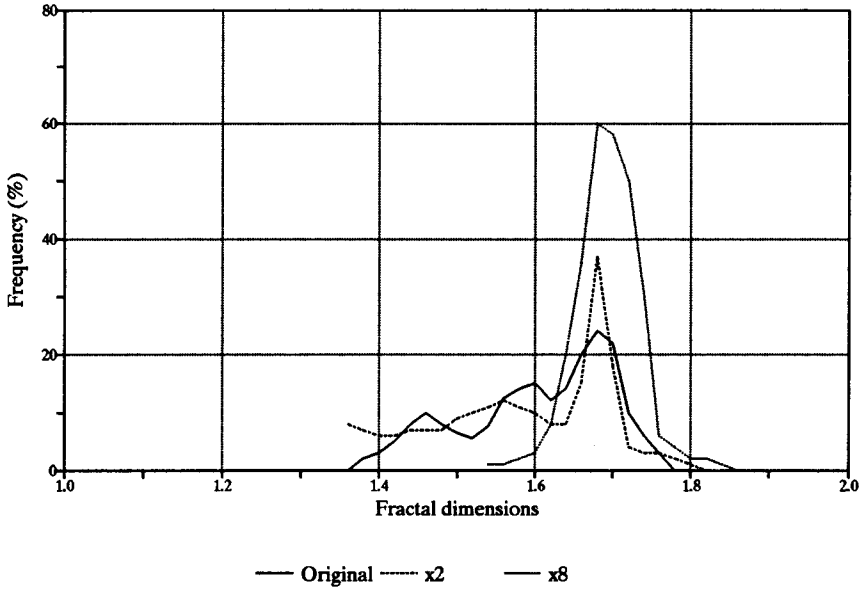

Figure 36. Fractal dimension frequency distribution of cubic convolution algorithm

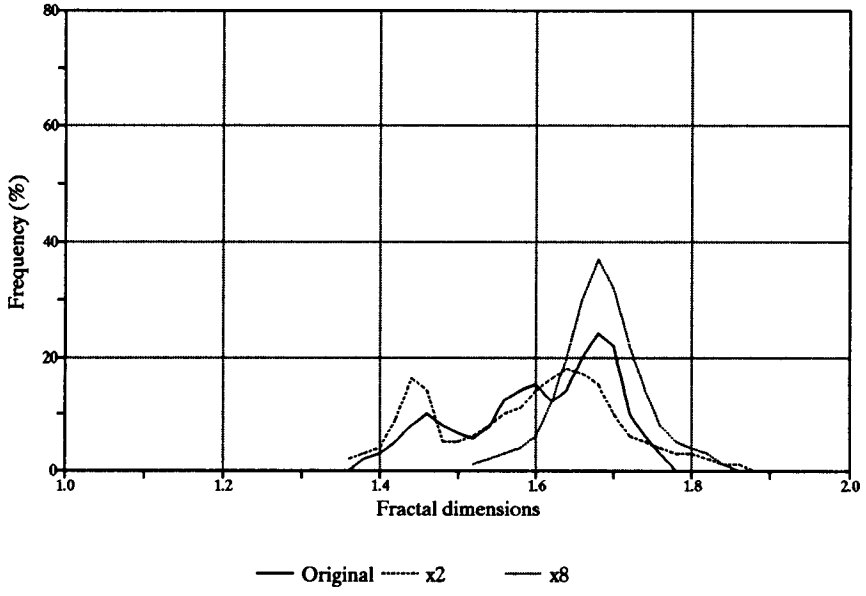

Figure 37. Fractal dimension frequency distribution of b-spline algorithm

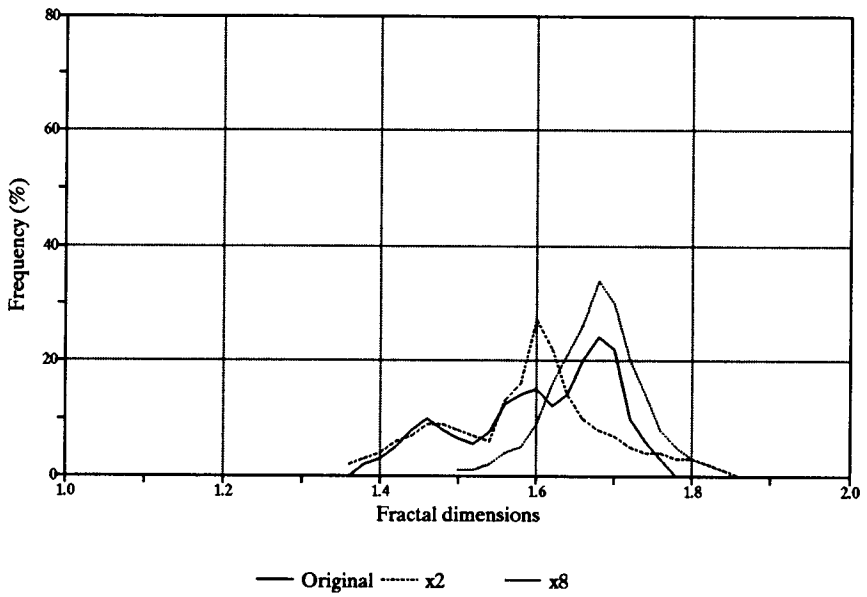

Figure 38. Fractal dimension frequency distribution of parametric Bezier algorithm

APPLICATIONS

Landuse Classification (texture feature)

The texture measure (co-occurrence matrix) from the Fourier/Radon transformed TM image (scaled to 10 meter resolution) was applied together with TM data from May 22 and July 1 of 1991. The fractal dimension was used as an additional spectral band together with bands 3 and 4. A minimum distance classification was performed to classify the southern Columbia basin agriculture fields. The results showed a reasonable improvement of the classification accuracy. Major improvement can be seen in the textured feature (e.g, orchards). The summary of the classification accuracy is shown in Figures 37-39 and Tables 9-16.

Table 9 Contingency table of raw image classification

	TRUTH					
CLASSIFICATION	Potatoes	Orchards	Alfalfa	Bean	Total	Row Accuracy
Potatoes	200	36	23	14	273	73%
Orchards	9	125	42	5	181	69%
Alflafa	19	26	307	28	380	81%
Bean	1	31	17	30	79	38%
Total	229	218	389	77	0	
Column Accuracy	87%	57%	79%	39%		73%

Table 10 Contingency table of combined raw and GVI image classification

	TRUTH					
CLASSIFICATION	Potatoes	Orchards	Alfalfa	Bean	Total	Row Accuracy
Potatoes	197	34	28	6	265	74%
Orchards	10	117	37	2	166	70%
Alflafa	16	35	298	34	383	78%
Bean	6	32	26	35	99	35%
Total	229	218	389	77	0	
Column Accuracy	86%	54%	77%	45%		71%

Table 11 Contingency table of combined raw and NDVI image classification

	TRUTH					
CLASSIFICATION	Potatoes	Orchards	Alfalfa	Bean	Total	Row Accuracy
Potatoes	207	31	40	12	290	71%
Orchards	4	124	44	4	176	70%
Alflafa	15	21	299	25	360	83%
Bean	3	42	6	36	87	41%
Total	229	218	389	77	0	
Column Accuracy	90%	57%	77%	47%		73%

Table 12 Contingency table of Fourier/Radon transformed image classification

	TRUTH					
CLASSIFICATION	Potatoes	Orchards	Alfalfa	Bean	Total	Row Accuracy
Potatoes	219	23	27	9	278	79%
Orchards	2	158	28	5	193	82%
Alflafa	5	15	318	21	359	89%
Bean	3	22	16	44	85	52%
Total	229	218	389	79	0	
Column Accuracy	96%	72%	82%	56%		81%

Table 13 Contingency table of resampled (10 meter) GVI image classification

	TRUTH					
CLASSIFICATION	Potatoes	Orchards	Alfalfa	Bean	Total	Row Accuracy
Potatoes	209	25	17	8	259	81%
Orchards	7	133	41	4	185	72%
Alflafa	10	30	312	29	381	82%
Bean	3	29	19	36	87	41%
Total	229	217	389	77	0	
Column Accuracy	91%	61%	80%	47%		76%

Table 14 Contingency table of resampled (10 meter) NDVI image classification

	TRUTH					
CLASSIFICATION	Potatoes	Orchards	Alfalfa	Bean	Total	Row Accuracy
Potatoes	212	31	39	6	288	74%
Orchards	6	129	37	7	179	72%
Alflafa	9	18	308	29	364	85%
Bean	2	39	5	35	81	43%
Total	229	217	389	77	0	
Column Accuracy	93%	59%	79%	45%		75%

Table 15 Contingency table of resampled (10 meter) Fourier/Radon transformed image classification

	TRUTH					
CLASSIFICATION	Potatoes	Orchards	Alfalfa	Bean	Total	Row Accuracy
Potatoes	218	13	28	11	270	81%
Orchards	3	174	21	2	200	87%
Alflafa	8	14	326	21	369	88%
Bean	0	17	14	45	76	59%
Total	229	218	389	79	0	
Column Accuracy	95%	80%	84%	57%		83%

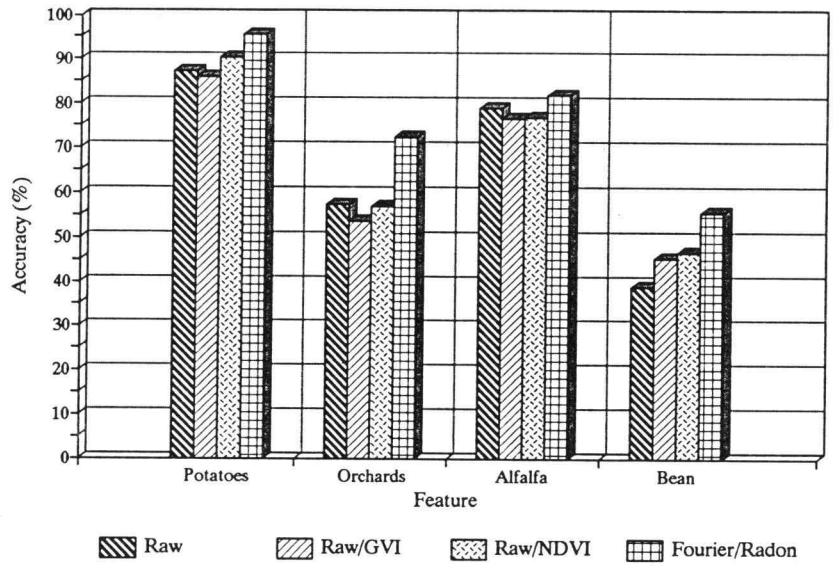

Figure 39. Minimum distance classification accuracies from various image sources

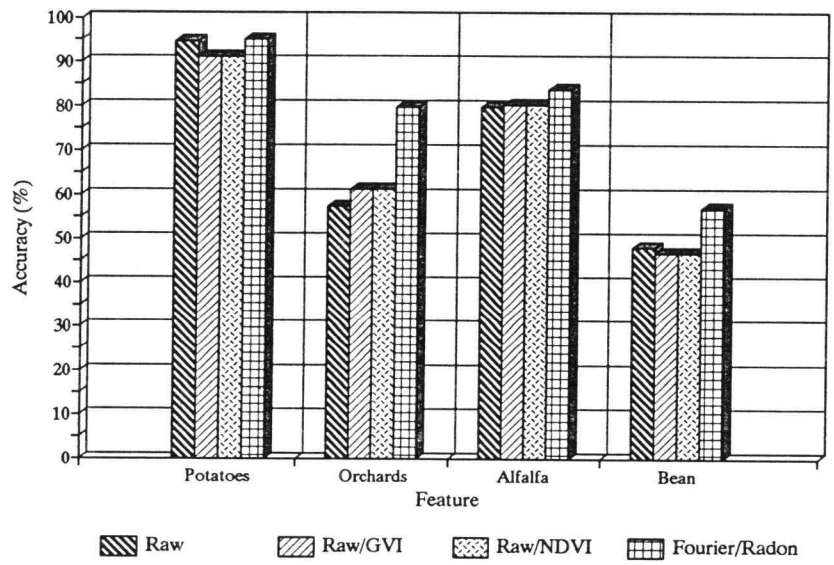

Figure 40. Minimum distance classification accuracies from various image sources

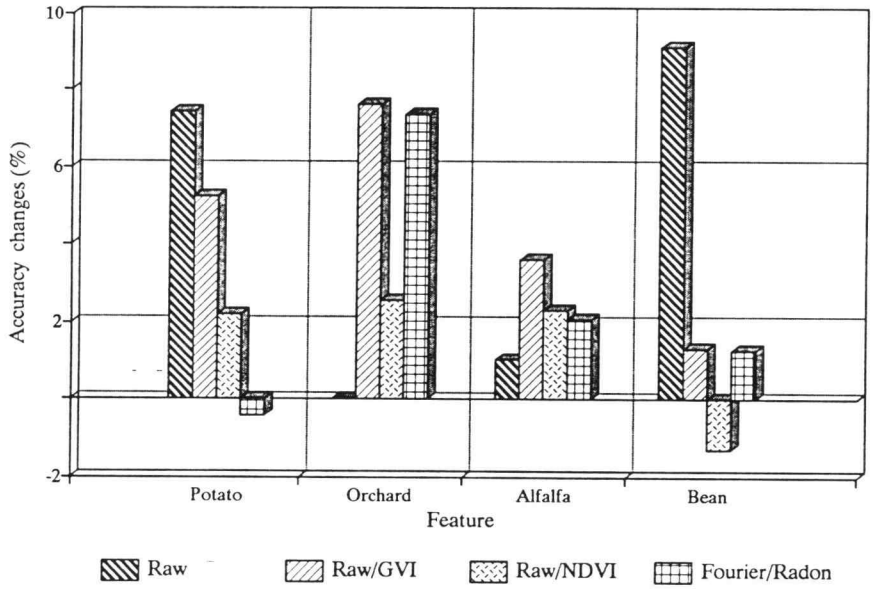

Figure 41. Minimum distance classification accuracies from various image sources

The use of the Fourier/Radon transformed enhanced image (same TM data set) also proved to be useful for a neural network classifier (Chen and Waddington, 1992). The accuracy of using a texture feature enhanced image is summarized in Table 16. The Contingency table was not used in this case since a stratified random sampling technique was used for accuracy assessment (see Appendix). The result showed the texture enhanced classification improved the accuracy bound for the neural network classifier.

Table 16 Classification accuracy bounds using a Fourier/Radon texture enhanced image

Classification Algorithm	Accuracy Bounds	Confidence Level
Minimum Distance	< 0.768,0.843 >	95%
Maximum Likelihood	< 0.749,0.812 >	95%
Neural Networks	< 0.811,0.833 >	95%

Image Scaling for Regional Ecosystem Modeling

The satellite image used in the data analysis section was used in this case. The Fourier and Radon transforms were applied to the raw image to obtain an image with higher fractal dimension. A algorithm with its original concept from the grey scale co-occurrence matrix was implemented as follows

(1) Assume a convolution window of size *nxn* and compute the sums of the squares (i.e. cross variance) of the differences in intensity of the center pixel from the center top, center left, center right, and center bottom pixels in the windows. The cross variance is equal to

$$I(x,y) = \sum_{(i,j)\,\epsilon S} [I(x,y) - i(x+i,y+j)]^2 \qquad (254)$$
$$S = \{(0,a),(0,-a),(a,0),(-a,0)\}$$

(2) Pass a *3x3* window across the variances and save the minimum from the nine variances in the center pixel. Pass another *3x3* convolution window across the resulting image and set the center pixel to zero if its value is not the largest in the window. The result is the possible centroid of the texture field.

(3) The resulting pixels from the above procedures were used as the seeds for a *9x9* dilation/erosion convolution window. A fractal dimension threshold was preselected to maintain the entropy level during the spatial degradation process.The result is an image which has a coarser spatial resolution suitable for regional scale modeling (the resolution can be changed by selecting a different iteration number) with similar image information content compared to the original image (Figure 42).

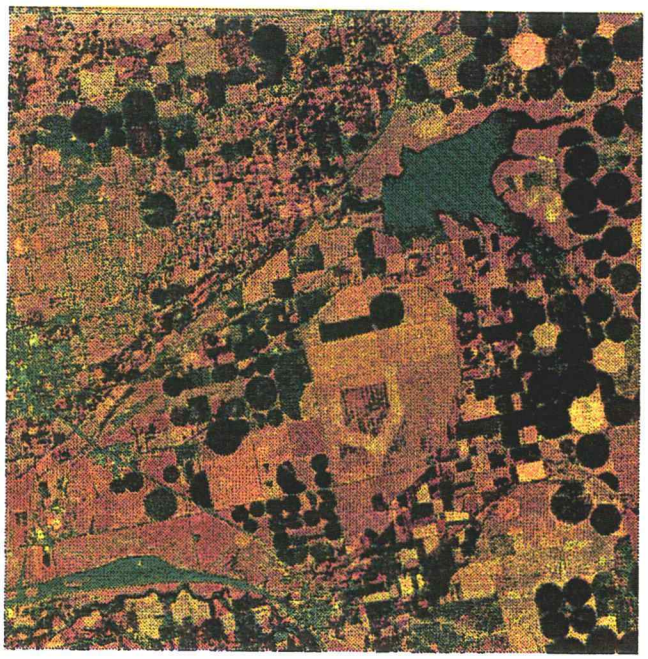

Thematic Mapper Band 4, 5, 3

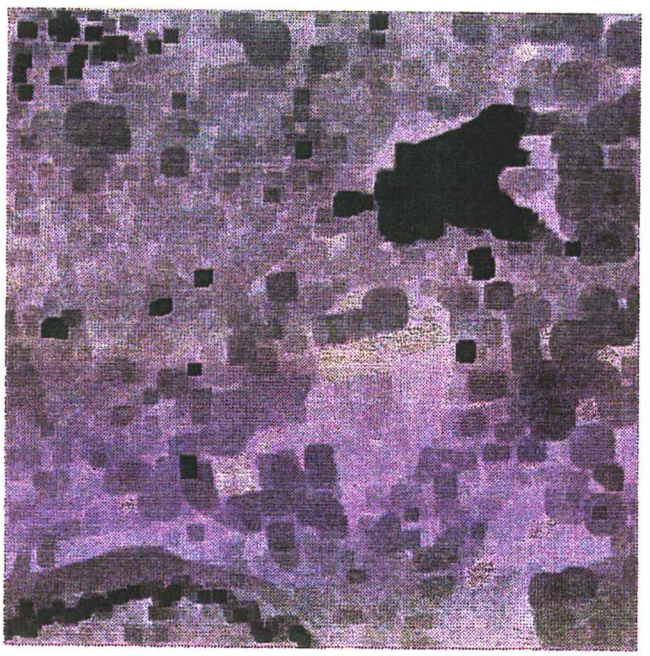

Erosion Scale Process

Figure 42. Scale transformed image for regional ecosystem modeling

CONCLUSIONS AND RECOMMENDATIONS

Summary

A general analytical framework was established for scale-related variabilities in remote sensing measurements. The study started with a basic plant canopy model, relations between canopy reflectance and phenological parameters. The relation between leaf area index, ground cover, and spectral reflectance was also investigated strictly from the probability of photon transfer and leaf projection. The variabilities introduced by scaling was investigated using a simulation model, ground measurement, and satellite data. The relation between orthogonal based transforms and Kahunen-Loéve transform were investigated in the vector space. The spatial domain information extraction was conducted using the Fourier transform with the Radon transform enhancement. The image information content was evaluated using various first and second-order statistics, entropy, and fractal dimensions. The Fourier and Radon transformed image has showed strong scale invariant characteristics in most cases. The utility of this framework was verified by two applications.

Conclusions

The general conclusion from this research was the potential use of spatial frequency domain operator to extract/maintain the scale related spatial variabilities in remote sensing. The study showed the characteristics of spectral variabilities as a function of complex background, shadow, and particularly changes in scale. The canopy spectral reflectance study indicated a very detailed canopy model may provide insights of the radiative transfer physical processes, but most likely will not provide enough information related to the scale issues. In terms of information content, the vegetation indices (e.g, GVI) and Kahunen-Loéve transform do not render themselves as useful tools for scale related applications. The spatially scaled GVI and Kahunen-Loéve transformed images suffered from a severe information degradation. These results do not exclude these transforms from being useful tools for image analysis. The result does imply the inadequacy of these transforms for multi-sensor or multiscale data fusion. A combination of the Fourier and Radon transform, on the other hand, demonstrated the capability to maintain higher information content and to enhance the texture feature within the image. These capabilities were proven to be very useful in general landuse classification and scale image data. The Fourier/Radon transformed image with a texture measure such as uniformity provided a good feature extraction tool in a scaled image especially for features with texture patterns. Additional information about the utility and quality of various spatial resampling algorithms was revealed using the Fourier power spectrum fractal dimension as a measure of information content. Most sophisticated resample algorithms (mathematically robust and visually superior) showed poor quality in terms of maintaining the original spectral information.

Recommendations

Several recommendations for future research in related topics can be made from the results of this project.

(1) More research should be conducted on the effects of shadow, soil background, soil color, moisture content and mineral composition on multispectral transforms. A spatial scale spectral variability component should be implemented in canopy models using a stochastic approach.

(2) More work should be done on ray tracing procedure by replacing detailed single photon ray tracing with simplified canopy/phenological parameter models. A cellular level near-infrared radiative transfer model will provide a key component to complete the reflectance model which covers the spectral wavelength of the most useful bandwidth.

(3) One important aspect not covered by the project is the effect of limited bandpass filters. Filters tuned to structured features that exist in the image should enhance the texture measure of the fractal dimension. If the measured distribution corresponding to a filter does not match the associated features in the image, the resulting output should exhibit strong relation with a Gaussian field. The scaling law may not be applicable under this circumstance. More research should be conducted for better texture measures.

(4) The effect of radiometric scaling should be used together with the spatial scaling. A preliminary result from the author's other research showed a radiometric degradation from 8 bit data to 6 bit data reduced the dynamic range by the fourth root of a dynamic range. The effect of radiometric scaling may be the key to reduce the use of high spatial resolution data which requires huge data storage space.

(5) More effort should be made to bring the high level image processing techniques to the general remote sensing community. Some of these techniques have long been developed in a national lab or other government research center but were never made available generally. An enormous amount of time in this project was spent in developing computer code for data analysis. Current research in remote sensing is more or less limited and restricted by the features available from commercial off-the-shelf packages. The general direction of the quality of remote sensing research should not be hindered by the computer programming issue.

BIBLIOGRAPHY

Anderberg, M.R., 1973. ***Cluster analysis for applications***. Academic Press, New York.

Axness, D and C.F Chen, 1991. "Estimation of ground cover via spectral data", Proceedings of the ASCE Irrigation and Drainage Specialty Conference, ASCE, Honolulu, July 21-24, 1991.

Ball, G.H and D.J Hall, 1965. "Isodata, an iterative method of multivariate analysis and pattern classification", Proceedings of the IFIPS Congress.

Babu, C. C., 1973 "On the application of probabilistic distance measures for the extraction of features from imperfectly labeled patterns", International Journal of Computer and Information Sciences, Vol.2, No.2, pp. 103-114

Baubaud, J., A. Witkin, M. Baudin, and R.O. Duda, 1986. "Uniqueness of the Gaussian kernel for scale-space filtering", IEEE Transactions on Pattern Analysis and Machine Intelligence, Vol. PAMI-8, No.1, pp. 26-33.

Bauer, M.E., M.C. McEwen, W.A. Malila, and J.C. Harlan (1978). Design, implementation, and results of LACIE field research. In Large Area Crop Inventory Experiment, Vol. III. NASA/Johnson Space Center, Houston, Texas, pp. 1037-1066.

Bauer, M.E., C.S.T. Daughtry, L.L. Biehl, E.T. Kanemasu, and F.G. Hall, 1986. "Field spectroscopy of agricultural crops". IEEE Transactions on Geoscience and Remote Sensing.

Biederman, I., 1985. "Human image understanding: Recent research and a theory", Computer Vision, Graphics and Image Processing, Vol.32, 1985, pp. 29-73.

Bischof, W.F. and T. Caelli, 1988. "Parsing scale-space and spatial stability analysis", Computer Vision, Graphics and Image Processing. 42, 1988, pp. 192-205.

Butler, D.M. *et al.* 1984, ***Earth Observing System: Science and Mission Requirements Working Group Report***, Vol. I & Appendix, NASA TM-86129, Washington, D.C.

Butt, E.B., 1968. "Studies in visual texture manipulation and synthesis", Technical report 64-68, Computer Science Center, University of Maryland, College Park.

Chen, C.F, 1990. "Columbia basin SPOT satellite remote sensing pilot project", Special report, SPOT Image Corporation, Reston, VA.

Chen, C.F. and Frank G. Lamb, 1991. "Using landsat to provide potato production estimates to Columbia basin farmers and processors", NASA EOCAP-1 Final report, Washington, D.C.

Chen, C.F. and George Waddington, 1992. "Using neural networks pattern recognition in satellite

remote sensing land classification", Chapter 18, ***Advances in Image Analysis***, Y. Mahdabvieh (editor), SPIE Optical Engineering Press, Bellingham, WA.

Chien, Y.T. and K.S. Fu, 1967. "On the generalized Karhunen-Loéve expansion", IEEE Transactions on Information Theory. Vol. IT-13, No. 3, pp. 518-520.

Choudhury, B.J., 1987. "Relationship between vegetation indices, radiation absorption, and net photosynthesis evaluated by a sensitivity analysis", Remote Sensing of Environment, 22:209-233.

Clark, B.P., 1986. "New look-up tables", Landsat Technical Notes, No.1, August 1986.

Clarke, K. and Diane M. Schweizer, 1991. "Measuring the fractal dimension of natural surfaces using a robust fractal estimator", Cartography and Geographic Information Systems, Vol. 18, No. 1, 1991, pp. 37-47.

Cover, T.M., 1965. "Geometrical and statistical properties of systems of linear inequalities with applications to pattern recognition", IEEE Transactions on Electronic Computer, Vol. EC-14, No. 3, pp. 326-334.

Cover, T.M. and P.E. Hart, 1967. "Nearest neighbor pattern classification", IEEE Transactions on Information Theory, Vol. IT-13, No. 1, pp. 21-27.

Curran, Paul J., 1988. "The semivariogram in remote sensing: An introduction", Remote Sensing of Environment, Vol. 24, pp. 493-507.

Dellepiane, S., D.D. Giusto, S.B. Serpico, and G. Vernazza, 1991. "SAR image recognition by integration of intensity and textural information", International Journal of Remote Sensing, Vol. 12, No. 9, pp. 1915-1932.

Diner, D.J. and J.V. Martonchik, 1985. "Influence of aerosol scattering on atmospheric blurring of surface features", IEEE Transactions on Geoscience and Remote Sensing, GE-23:618-624.

Duda, R. and P. Hart, 1973. ***Pattern Classification and Scene Analysis***, John Wiley & Sons, New York.

Edwards, D.A., 1986. ***Modelling plant growth and development***, Academic Press, Australia.

Goel, N.S., 1989. "Inversion of canopy reflectance models for estimation of biophysical parameters from reflectance data" in ***Theory and Applications of Optical Remote Sensing***, G. Asar (editor), John Wiley & Sons, New York.

Grimson, W., 1985. "Computational experiments with a feature based stereo algorithm", IEEE Transactions on Pattern Analysis and Machine Intelligence, Vol. PAMI-7, pp. 17-34.

Haralick, R.M., K. Shanmugan, and I. Dinstein, 1973. "Texture features for image classification", IEEE

Transactions on System, Management, and Cybernetics, pp. 610-621.

Hall, F.G and G.D. Badhwar, 1987. "Signature extendable technology: Global space-based crop recognition", IEEE Transactions on Geoscience and Remote Sensing, Vol. GE-25 No. 1, Jan. 1987.

Hawkins, J.K. 1970., "Image processing principles and techniques" in ***Advances in Information System Science***, Vol. 3, Plenum Press, New York.

Herman, G.T. and G.Rozenberg. ***Developmental systems and languages***, Nother-Holland, Amsterdam.

Hodgson, R.M., D.G. Bailey, M.J. Naylor, A.L.M. Ng, and S.J. McNeil, 1985. "Properties, implementations, and applications of rank filters", Image and Vision Computing, 3(1).

Jackson, R.D., P.J. Pinter, R.J. Reginato, and S.B. Idso, 1980. ***Hand-held Radiometry***, Agricultural Reviews and Manuals, ARM-W-19, U.S. Department of Agriculture, Washington, D.C.

Jensen, John, 1986. ***Introductory Digital Image Processing : A Remote Sensing Perspective***, Prentice Hall, Englewood Cliffs, N.J

Julesz, B. 1975. "Experiments in the visual perception of texture", Scientific American, 232, 34-43

Julesz, B. and T. Caelli, 1979. "On the limits of Fourier decompositions in visual texture perception", ***Perception***, 8, 69-73.

Kanal, L. ed. 1968. ***Pattern recognition***, Thompson Book Co. Washington, D.C.

Kaufman, Y.J. and J.H. Joseph, 1982. "Determination of surface albedos and aerosol distinction characteristics from satellite imagery", Journal of Geophysics Research, 20:1287-1299.

Kittler, J. and J. Foglein, 1984. "Contextual classification of multispectral pixel data", Image and Vision Computing, 2, 13-19.

Kauth, R.J and G.S. Thomas, 1976. "The tasseled cap - a graphic description of the spectral temporal development of agricultural crops as seen by Landsat", In Machine Processing of Remotely Sensed Data. Purdue University, West Lafayette, Indiana, pp. 41-51.

Koenderink, J., 1984. "The structure of images", in Biological Cybernetic. Springer Verlag, New York.

Lalitha, L and D. Dutta Majumder, 1989. "Fractal based criteria to evaluate the performance of digital image magnification techniques", Pattern Recognition Letters, Vol. 9, pp. 67-75.

Lam, N.S.N, 1990. "Description and measurement of Landsat TM images using fractals", Photogrammetric Engineering and Remote Sensing, Vol. 56, No. 2, 1990, pp. 187-195.

Lillesand, T.M. and Ralph W. Kiefer, 1987. ***Remote Sensing and Image Interpretation*** 2nd Ed. John

Wiley and Sons, New York.

Lindenmayer, A., 1968. "Mathematical models for cellular interaction in development, Part I and Part II", Journal of Theoretical Biology, 18:280-315.

MacDonald, R.B. and F.G. Hall, 1980. "Global crop forecasting", Science 208:670-679.

Mandelbrot, B.B., 1977. ***Fractals: Form, Chance and Dimension***, Freeman, San Francisco, CA.

Menke, William, 1989. ***Geophysical Data Analysis: Discrete Inverse Theory***, Academic Press, Inc. San Diego, California.

Myneni, R.B., J. Ross, and G. Asrar, 1989. ***A Review on the Theory of Photon Transport in Leaf Canopies*** Special issue, Agricultural and Forest Meteorology, 45, 1-153.

Nilsson, N.J., 1965. ***Learning Machine***. McGraw-Hill, New York.

Peitgen, H.O and P.H. Richter, 1986. ***The Beauty of Fractals***, Springer-Verlag, New York.

Pentland, A.P., 1984. "Fractal-based description of natural scenes", IEEE Transactions on Pattern Analysis and Machine Intelligence. Vol. PAMI-6, No. 6.

Pratt, W., 1991. ***Digital Image Processing***, John Wiley & Sons, New York.

Preparata, F.P., 1973. ***Introduction to Discrete Structures***, Addison-Wesley, Reading, MA.

Prusinkiewics, P., K. Krithivasan, and M.G. Vijayanarayana, 1989. "Application of L-systems to algorithmic generation of South Indian folk art patterns and karnatic music", In R. Narasimhan, editor, ***A perspective in theoretical computer science - commemorative volume for Gift Siromoney,*** pp. 229-247. World Scientific, Singapore.

Prusinkiewics, P., 1986. "Graphical applications of L-systems", In Proceedings of Graphics Interface '86 - Vision Interface '86, pp. 247-253. CIPS.

Schroeder, Manfred, 1991. ***Fractals, Chaos, Power Laws***, W.H. Freeman and Company, New York.

Sellers, P.J. 1985. "Canopy reflectance, photosynthesis and transpiration", International Journal of Remote Sensing, 6:1335-1372.

Slater, P.N. and R.D. Jackson, 1982. "Atmospheric effects on radiation reflected from soil and vegetation as measured by orbital sensors using various scanning directions", Applied Optics, 21:3923-3931.

Stoffel, J.C. and J.F.Moreland, 1981. "A survey of electronic techniques for pictorial image reproduction", IEEE Transactions on Communication, 29(12), 1898-1925.

Stoner, E.R. and M.F. Baumgardner, 1981. "Characteristic variation in reflectance of surface soils", Soil Science Society of America Journal, 45:1161-1165.

Swain, P.H. and H. Hauska, 1977. "The decision tree classifier: design and potential", IEEE Transactions on Geosciences Electronics, GE-15, 142-147.

Tou, J.T., 1974. ***Pattern Recognition Principles***. Addison-Wesley Publishing Company.

Tou, L.J., 1968. "Feature extraction in pattern recognition", ***Pattern Recognition***, Vol. 1, No. 1, pp. 3-11

Varmuza, K., 1980. ***Pattern recognition in chemistry***. Lecture notes in Chemistry 21, Springer-Verlag, Berlin.

Watanabe, S., 1965. "Karhunen-Loéve expansion and factor analysis-theoretical remarks and applications", Proceedings of the 4th Conference on Information Theory, Prague, Hungry.

Weszka, J.S, C.R. Dyer, and A. Rosenfeld, 1976. "A comparative study of texture measures for terrain classification", IEEE Transactions on System, Management, and Cybernetics, pp. 269-285.

Williams, D. and M. Shah, 1988. Edge Contours. Technical report CS-TR-88-18, University of Central Florida, Computer Science Department, Sept.

Wong, R.Y., 1979. "Image sensor transformations", IEEE Transactions on System, Management, and Cybernetics, 7(12), 836-841.

Young, T.Y and T.W. Calvert, 1974. ***Classification, Estimation, and Pattern Recognition***, Elsevier Publishing Co., New York.

APPENDICES

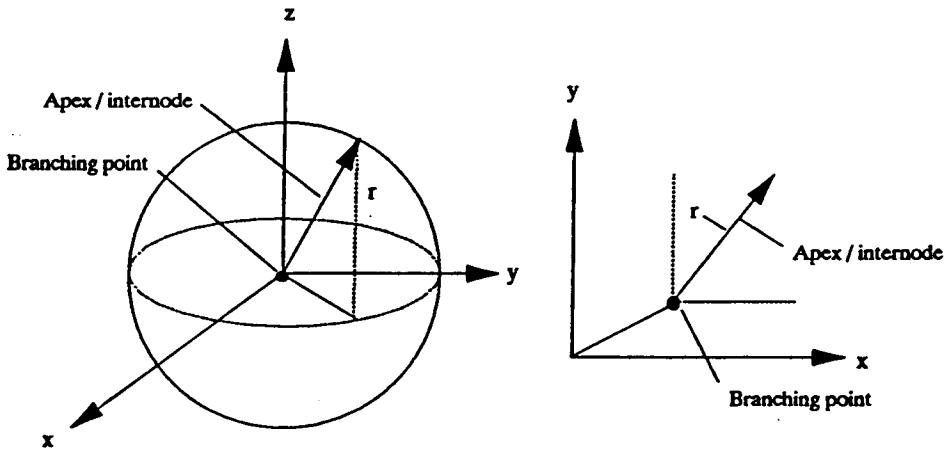

Figure A.1 Plant branching structure represented in three dimensional space

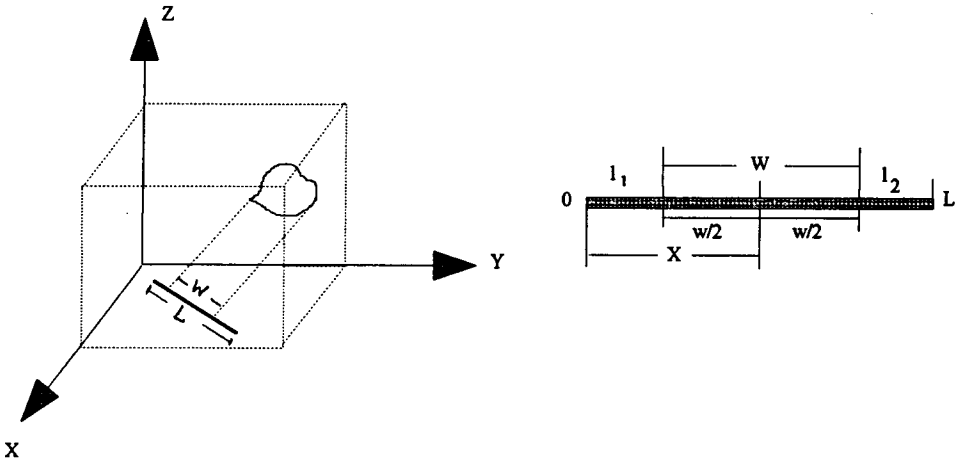

Figure A.2 Leaf projection and related coordinate system

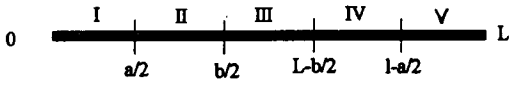

Figure A.3 Line transect division for integration

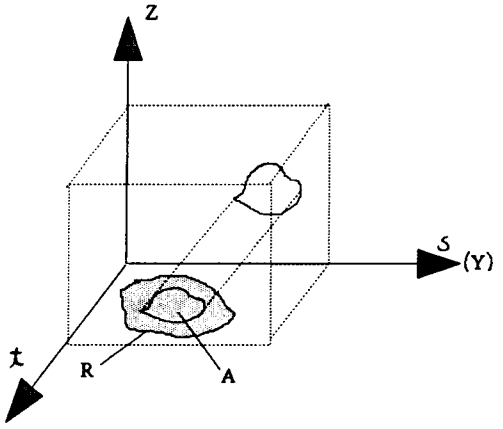

Figure A.4 Canopy mapping from three dimensional to two dimension space

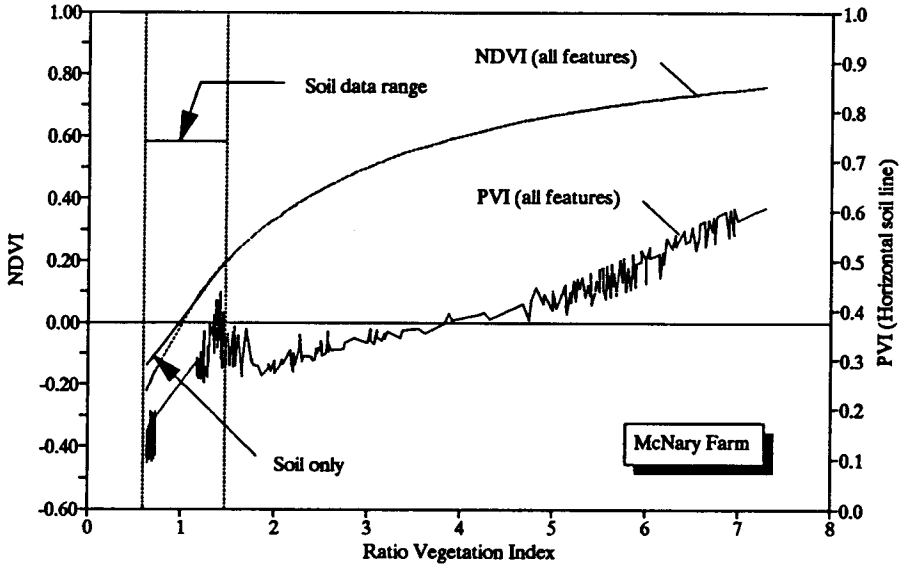

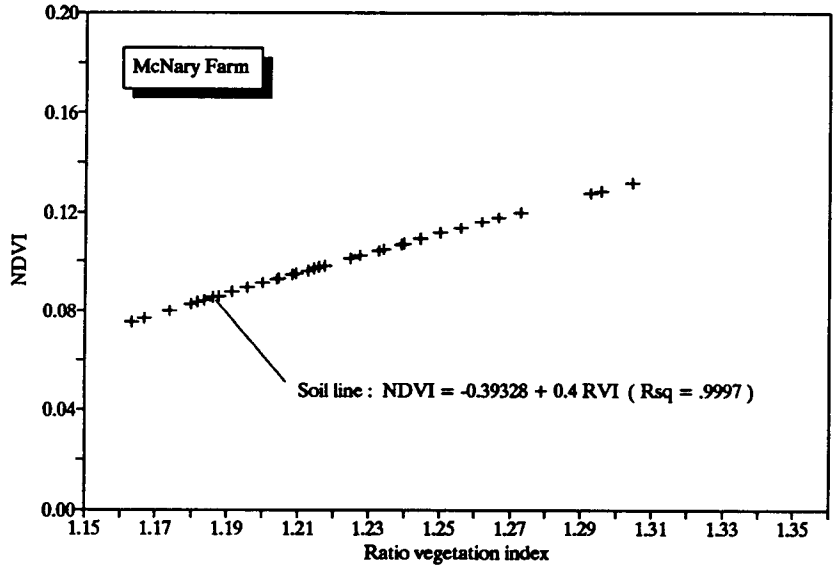

Figure A.5 Functional relation between vegetation indices (SPOT HRV 6/10/88)

Classification Accuracy Assessment Using Stratified Random Sampling

Introduction

The assessment of classification accuracy allows a degree of confidence to be attached to the thematic map. Traditionally, accuracy was determined empirically by selecting a sample of pixels from the thematic map and the labels were checked against classes determined from reference data. One commonly used method is the contingency table (or confusion matrix) that incorporated omission and commission errors. Choice of the sample of pixels is a topic still under investigation. Most methods use some kind of randomized strategy to select the sample. A problem that can arise with random sampling is the area weighted bias. Large classes tend to be represented by a larger number of sample points than the smaller classes; some small classes may not be represented at all. The following section described a ***stratified random sampling*** scheme that can be used as an accuracy assessment tool.

Stratified Random Sampling

The implementation of the method is straight forward. It includes the following steps :

(1) Select a set of strata into which the image is divided. The most appropriate stratification to use is found to be the actual thematic classes.

(2) Choose a random sample (30 to 60 samples) within each thematic class to assess the classification accuracy of that class.

(3) Decide the confidence level for accuracy (see next section for details)

Error/Confidence Level of A Classification

Suppose the true map accuracy for a class is θ. The probability of x pixels being correct in a random sample of n pixels from that class is given by the binomial probability

$$p(x;n,\theta) = C_x^n \, \theta^x (1 - \theta)^{n-x} \qquad x = 0,1,\ldots,n$$

where

$$\theta = \frac{\sum_{i=1}^{n} x_i}{n} \qquad \text{n : number of samples}$$

The "***correctness***" of the classification can be represented by a binomial form (correct or not correct). A better expression for the classification accuracy is using an interval within which

the true map accuracy lies (e.g. 95 % certainty). This interval can be expressed as

$$P\left\{ -Z_{\frac{\alpha}{2}} < \frac{x - n\theta}{\sqrt{n\theta(1-\theta)}} < Z_{\frac{\alpha}{2}} \right\} = 1 - \alpha$$

where

x : number of correctly labelled pixels in a sample of n

θ : true map accuracy as shown in previous equation

$1-\alpha$: confidence level

If we choose $\alpha=.05$ the above expression states that the probability of $(x-n\theta)/\sqrt{n\theta(1-\theta)}$ will be between $\pm z_{\alpha/2}$ is 95%; $\pm z_{\alpha/2}$ are points on the normal distribution between which $1-\alpha$ of the population is contained.

Numerical Example

Assume $x = 211, n = 250$ for a class category and $\alpha = .05$ *(95% confidence level)*. The true map accuracy (sample mean from random sampling) for the class is $x/n = .844$ *(estimation of* θ*)* . The bounds for θ are calculated by

$$Z_{\frac{\alpha}{2}} = \frac{x - n\theta}{\sqrt{n\theta(1-\theta)}}$$

Obtain $z_{\alpha/2} = 1.96$ from a statistic table. Solve for θ

$$1.96 = \frac{211 - 250\theta}{\sqrt{250\times\theta(1-\theta)}} \quad \rightarrow \theta = .88586 \text{ or } .78674$$

which implies the bounds for θ are

$$.78674 < \theta < .88586$$

This concludes that we have *95%* confidence that the overall map accuracy is somewhere between *78.7%* and *88.6%* compared to the estimated $\theta = .844$ *(sample mean)*.

Modeling the effect of sensor field of view (FOV), height, off-nadir viewing angle

The variability of spectral reflectance is a function of sensor height, sensor field of view and off-nadir viewing angle due to a misaligned sensor. The calculation of effective sensing area is a necessary procedure in the case when a non-imaging sensing device is used. The following analysis is performed in order to quantify the relationship between each factor that could affect the spectral value. The basic optical geometry is illustrated in Figure A.6

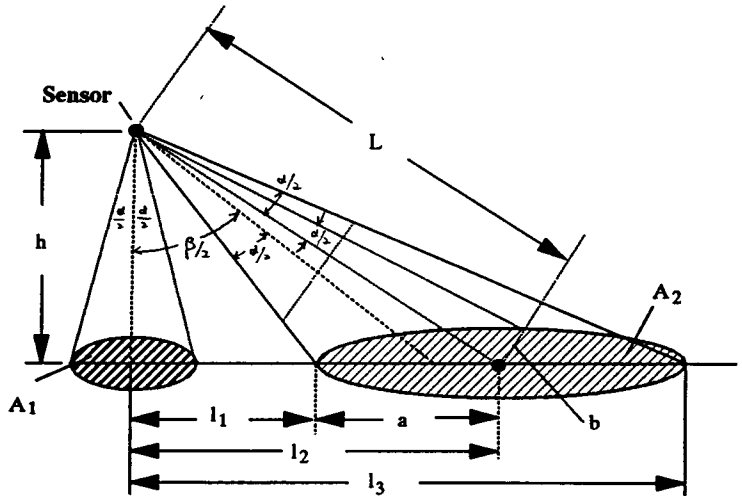

Figure A.6 Sensor field of view, off-nadir viewing angle and viewing height geometry

The following terms need to be defined and calculated

$$\theta = \frac{\beta - \alpha}{2} \quad , \delta = \frac{\beta + \alpha}{2}$$

$$l_1 = h\tan\theta \qquad l_3 = h\tan\delta$$

$$l_2 = l_1 + \frac{1}{2}(l_3 - l_1) = \frac{1}{2}(l_1 + l_3)$$

$$a = \frac{1}{2}(l_3 - l_1) = \frac{h}{2}[\tan\delta - \tan\theta] \quad , \; b = L\tan\frac{\alpha}{2}$$

$$L = (h^2 + l_2^2) = [h^2 + \frac{1}{4}(l_1 - l_3)^2]^{\frac{1}{2}}$$

$$\text{Ellipse Area} - A_2 - \pi ab$$

$$- \frac{\pi h}{2} \tan\frac{\alpha}{2} [\tan\delta - \tan\theta] [h^2 + \frac{1}{4}(l_1 + L_3)^2]^{\frac{1}{2}}$$

$$- \frac{\pi h}{2} \tan\frac{\alpha}{2} [\tan\delta - \tan\theta] [\frac{4h^2}{4} + \frac{h^2}{4}(\tan\theta + \tan\delta)^2]^{\frac{1}{2}}$$

$$- \frac{\pi h^2}{4} \tan\frac{\alpha}{2} [\tan\delta - \tan\theta] [4 + (\tan\theta + \tan\delta)^2]^{\frac{1}{2}}$$

Figure A.7 demonstrates the percent effective sensing area deviation introduced by off-nadir viewing under different sensor field of view with a 10 meter sensor height

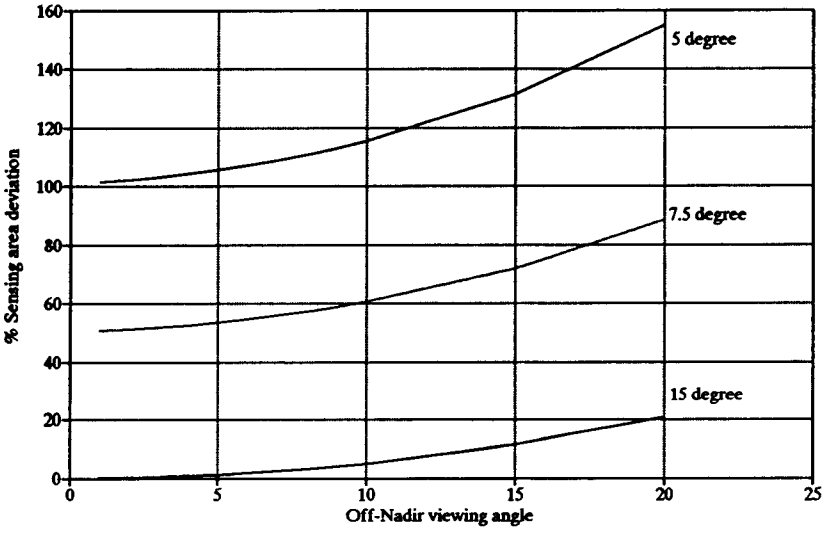

Figure A.7 Effective sensing area deviation as a function of off-nadir angle